# New Route to Frustration by Quantum Many-Body Effects in the Spin Liquid Pyrochlore $Tb_2Ti_2O_7$

by

Hamid Reza Molavian

A thesis
presented to the University of Waterloo
in fulfilment of the
thesis requirement for the degree of
Doctor of Philosophy
in
Physics

Waterloo, Ontario, Canada, 2007

AUTHOR'S DECLARATION FOR ELECTRONIC SUBMISSION OF A THESIS

I hereby declare that I am the sole author of this thesis. This is a true copy of the thesis, including any required final revisions, as accepted by my examiners.

I understand that my thesis may be made electronically available to the public.

# Abstract

In this thesis we investigate the frustrated spin liquid $Tb_2Ti_2O_7$ theoretically. The low-energy effective Hamiltonian of this compound is derived by integrating out the excited crystal field states. It is shown that the pairwise interaction in the effective Hamiltonian is renormalized by all the other $Tb^{3+}$ ions in the system and dynamically generate frustration. The phase diagram of $Tb_2Ti_2O_7$ in the single tetrahedron approximation is calculated. It is shown that $Tb_2Ti_2O_7$ is in a singlet state which is a linear combination of all frustrated two-in/two-out states. Motivated by experimental results, the diffuse neutron scattering of $Tb_2Ti_2O_7$ is obtained within the single tetrahedron approximation. This diffuse neutron scattering captures semi-quantitatively most of the experimental neutron scattering features. The magnetization of $Tb_2Ti_2O_7$ in the single tetrahedron approximation is calculated. Two experiments based on diffuse neutron scattering and magnetization in high symmetry directions are proposed to verify the spin ice like ground state of $Tb_2Ti_2O_7$.

# Acknowledgements

I would like to thank my supervisor Michel Gingras for his enthusiasm, thoughtful suggestions and continual support of this project.

I would like to acknowledge my Ph.D. advisory committee Tom Devereaux, Jan Kycia, Bill Power, Robert Mann and Achim Kempf for their useful suggestions and comments during my study at Waterloo and also

I would like to thank Prof. Oleg Tchernyshyov who accepted to be my Ph.D external examinar and for his useful suggestions on the thesis.

During this project I also benefitted from many useful discussions with Bruce Gaulin and Jason Gardner and here I would like to thank them.

I wish to acknowledge Prof. Yoshiteru Maeno and Dr. Ryuji Higashinaka for the stimulating collaboration from which the experimental data presented in Appendix A originate.

I would like to give my special thanks to Samad Bazargan, Azad Qazi-zade and Sattar Taheri-Araghi for their help in the final revision of the thesis.

My special thank to my colleagues Matthew Enjalran, Adrian Del Maestro , Jean-Yves Delannoy, Jacob Ruff, Taras Yavors'kii, Jeffrey Quilliam, Tom Fennell, Ali Tabei, Francois Vernay, Pawel Stasiak, Mahmoud Ghaznavi, Roger Melko, Martin Weigel, Mohammad Kohandel, Farhad Shahbazi, Koroush Afrousheh, and Jacob Cosman.

**Dedicated to My Parents,**

# Contents

# List of Figures

# List of Tables

# Chapter 1

# Introduction

## 1.1 Frustration

Frustration is a general concept, arising in different branches of physics and at the origin of many novel and interesting phenomena [1-4]. In a physical system, frustration occurs when the minimum energy of a system does not correspond to the minimum energy of the interactions among its degrees of freedom which are often pair-wise interactions. In some frustrated systems, the entropy of the system grows with the total number of degrees of freedom.

One of the simple examples of frustration is four Ising spins on a square with three ferromagnetic and one antiferromagnetic interactions between these Ising spins (Fig. 1.1). The minimum energy of a pair of Ising spins, coupled by the ferromagnetic (antiferromagnetic) interactions occurs when they are parallel (antiparallel). However, in this system, the Ising spin with one ferromagnetic and one antiferromagnetic interaction with its nearest neighbor cannot minimize its energy with its two nearest neighbors at the same time. Hence, this system is frustrated.

Another well-known example of frustration is one of the phases of water ice, called ice $I_H$. In this phase each oxygen atom is surrounded by four hydrogens and the minimum energy of this system occurs when two hydrogens are close to the oxygen and two hydrogens are far from it (Fig. 1.2) [5]. However, the ground

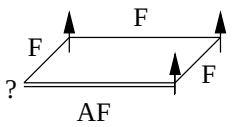


Figure 1.1: Four Ising spins on a square with three ferromagnetic (F) and one antiferromagnetic (AF) interactions between them.

state of this system remains disordered to the lowest accessible temperature [6, 7]. In addition, specific heat results show a residual entropy to the lowest measured temperature [6, 7]. At the time of publication, these results seemed implausible given the fact that every system had a unique ground state and zero residual entropy (third law of thermodynamics). Hence the question arose as to why this system did not order and had a residual entropy. Pauling was the first to answer this question by noticing that the two-close/two-far state was frustrated on the ice $I_H$ crystal structure and he calculated the residual entropy by counting the number of possible degeneracies of this state [8]. He found that the number of degeneracies grows with the number of oxygens and calculated the residual entropy to be $\frac{R}{2}\ln(\frac{3}{2})$ ($R$ is the gas constant), consistent with the experimental results [6, 7]. This was the first time that a frustrated system was investigated in physics and, interestingly, the source of frustration in this system is the special geometry of the ice $I_H$.

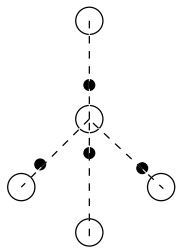

Figure 1.2: Arrangement of hydrogens around an oxygen in ice $I_H$. The protons (black dots) are in the two-close/two-far state which is frustrated. Oxygens are shown with big open circles.

Spin glasses are disordered magnetic systems in which frustration plays an essential role in these systems [9–12]. The source of frustration in these systems is disorder, which can be either structural disorder or disorder induced by doping.

For these systems, a phase transition from the paramagnetic phase to the spin glass phase occurs at the spin glass transition temperature, $T_g$. The important experimental sign of a spin glass phase is the difference in the field-cooled and zero-field-cooled magnetization data. In the field-cooled experiment an external magnetic field is applied to the system in the paramagnetic phase. The system is then cooled down to a temperature below $T_g$ and the magnetization is measured as a function of temperature (upon cooling). In the zero-field-cooled case the system is cooled with the field off, down to a temperature below $T_g$. When the required temperature is reached, a magnetic field is applied to the system. The temperature is then increased and the magnetization of the system is recorded as a function of temperature upon warming. As mentioned, the magnetization obtained from zero-field-cooled and field-cooled measurements are different in spin glass systems and typically bifurcate near $T_g$. This is in contrast to usual magnetic systems that have the same field-cooled and zero-field-cooled magnetizations. There are other experimental features that are unique to the spin glass systems such as the divergence (at $T_g$) of the third derivative of the magnetization as a function of magnetic field.

In most of the aforementioned physical systems, such as spin glasses and water ice, the complexity of the problem precludes an understanding of the generic behavior of frustration. Hence, the realization of other frustrated systems with less complexity and the same behavior as the mentioned systems can improve our understanding of frustration. In this way, "geometrically frustrated magnetic" systems are those with disorder-free crystal structures and tractable interacting Hamiltonians [13].

For an example of a geometrically frustrated system, consider a triangle and a square with antiferromagnetic Ising spins on their vertices (Fig. 1.3). For the square, the minimum energy of the system coincides with the minimum energy of all the pair-wise interactions. However, for the triangle, it is not possible to minimize all the pair-wise interactions simultaneously and this system is frustrated because of its special geometry. In fact, a first example of frustration in magnetic systems is the Ising model on the antiferromagnetic triangular lattice (a lattice made of triangles we discussed in the previous paragraph). An exact solution for

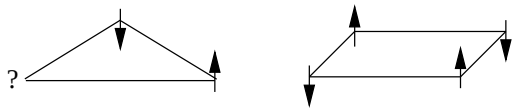


Figure 1.3: Three antiferromagnetic Ising spins on a triangle and a square. Ising spins on the triangle are frustrated because of the special geometry of the triangle.

the triangular lattice reveals a residual entropy and no transition to an ordered state down to zero temperature [14]. This can be naively understood by noticing that the frustration is not removed by attaching triangles together to make a triangular lattice and the number of degeneracies increase.

After this brief discussion about the geometrically frustration for the triangular lattice it is interesting to ask:"Is there a three dimensional variant of a triangle and a triangular lattice which can be geometrically frustrated?" The answer is yes.

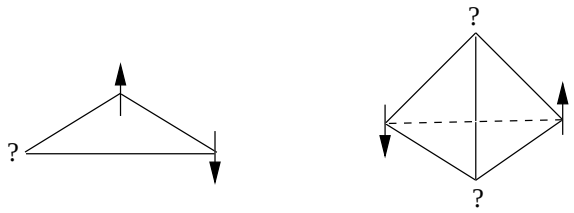


Figure 1.4: Tetrahedron is the three dimensional variant of the triangle in two dimensions. The antiferromagnetic Heisenberg spin 1/2 system on the vertices of a tetrahedron is frustrated.

The three dimensional variant of the triangle is a tetrahedron and this system with four antiferromagnetically classical spins of length $S$ on its vertices is frustrated (Fig. 1.4). This can be simply verified by noticing that the minimum energy of this system satisfies the $\mathbf{S}_1 + \mathbf{S}_2 + \mathbf{S}_3 + \mathbf{S}_4 = 0$ condition; hence it is not possible to simultaneously align all spins anti-parallel [16]. This can be easily shown by writing down the Hamiltonian as $H = \frac{J}{2}(\mathbf{S}_1 + \mathbf{S}_2 + \mathbf{S}_3 + \mathbf{S}_4)^2 - 2JS^2$, where $J$ is the antiferromagnetic exchange coupling ($J > 0$). As a result, the energy of this system is minimum when the expression in the parentheses $(\mathbf{S}_1 + \mathbf{S}_2 + \mathbf{S}_3 + \mathbf{S}_4)$ is zero.

Similar to triangles that make a triangle lattice in two dimensions, tetrahedra

| Primitive Vector of FCC lattice | Tetrahedral Basis |
|---|---|
| $\mathbf{a}_1=\frac{a}{2}(1,1,0)$ | $\mathbf{r}_1=\frac{a}{4}(0,0,0)$ |
| $\mathbf{a}_2=\frac{a}{2}(0,1,1)$ | $\mathbf{r}_2=\frac{a}{4}(1,1,0)$ |
| $\mathbf{a}_3=\frac{a}{2}(1,0,1)$ | $\mathbf{r}_3=\frac{a}{4}(0,1,1)$ |
| | $\mathbf{r}_4=\frac{a}{4}(1,0,1)$ |

Table 1.1: Primitive vectors and, the tetrahedra basis of the pyrochlore lattice. $a$ is the dimension of cubic unit cell.

can make a lattice in three dimensions. This lattice is called the pyrochlore lattice and can be considered as an FCC lattice with four basis vectors that make a single tetrahedron (Fig. 1.5). In Table 1.1 we give the primitive vectors of the FCC lattice and the four basis vectors. We use this nomenclature throughout the thesis.

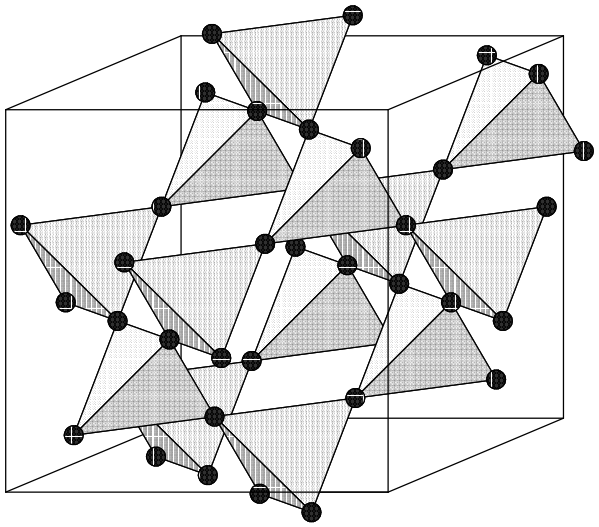

Figure 1.5: Pyrochlore lattice which is a lattice of corner sharing tetraher as.

In the previous paragraph we mentioned that the antiferromagnetic spin $S$ is frustrated on a single tetrahedron. It is interesting now to ask what is the effect of this frustration when we have antiferromagnetic quantum $S = 1/2$ and a clas-

sical spin on the pyrochlore lattice. This question has been a matter of extensive investigation [15-17]. In the classical case, the results of Monte Carlo, molecular dynamics and mean field show that this system remains in the disordered state at all temperatures [15,16]. Interestingly, because of the short range correlations in this system, the DC susceptibility of a single tetrahedron with classical spins gives the same susceptibility as the whole pyrochlore lattice [18]. In the quantum case, the results of perturbation expansion and exact diagonalization suggest a spin liquid ground state for this system with spin-spin correlations that never exceed interatomic distances [17]. From these results, we can conclude that because of the frustration, the correlations in both the classical and the quantum cases remain on the order of an interatomic distance.

From the previous discussion we realize that pyrochlore-based compounds should be a good playground for the emergence of geometrically frustration. Two important sets of chemical composition with pyrochlore lattice structure are $A_2B_2O_7$ and $CD_2O_4$ where A, B and D ions make a pyrochlore lattice. In these compounds A is a rare earth element, B is a transition metal, C is a divalent element and D is a magnetic transition metal or C is a monovalent and D is a trivalent transition metal. There are other compounds such as $YMn_2$, where Mn ions reside on a pyrochlore lattice. However, not all of the compounds with this structure are frustrated and we need to know: "what is the experimental criterion for a compound to be highly frustrated?". This criterion is usually defined as the ratio between the Curie-Weiss temperature $\theta_{\rm cw}$ and the transition temperature to an ordered state $T_c$. If this ratio $|\frac{\theta_{\rm cw}}{T_c}|$ is more than 10, the system is called highly frustrated [19]. Notice that this criterion is proposed based on rough experimental facts and the value of 10 is not really a critical value.

An example of these frustrated systems is $ZnCr_2O_4$ with $\theta_{\rm cw}$ equal to -392 K [20]. This system undergoes a spin-Peierls phase transition at 12.5 K, from a cubic spin liquid to a tetragonal Néel state [20–22]. For this system, the ratio $|\frac{\theta_{\rm cw}}{T_c}|$ is about 31, hence this system is highly frustrated. Inelastic neutron scattering of this compound reveals a novel phenomenon which until now is unique to frustrated systems. Six magnetic moments on hexagonal units of the pyrochlore lattice make unique objects interacting weakly with other hexagons [23]. This result is very

interesting because it shows that the degrees of freedom of a frustrated system can make small clusters and these clusters become new composite degrees of freedom.

Perhaps the richest discovered set of frustrated systems is composed of the compounds with the chemical composition $A_2B_2O_7$, where A is one of the rare earth ions $Er^{3+}$, $Tb^{3+}$, $Dy^{3+}$, $Ho^{3+}$ and $Yb^{3+}$, and B is one of the transition metal ions $Ti^{4+}$, $Sn^{4+}$ or $Mo^{4+}$. Here, we give some examples of these systems and their interesting properties.

$Y_2Mo_2O_7$ with $|\frac{\theta_{cw}}{T_c}| \approx 10$ shows a spin glass transition [24]. $Ho_2Ti_2O_7$ and $Dy_2Ti_2O_7$, known as spin ice systems, are the first magnetic systems that mimic the properties of water ice $I_H$ with no transition to an ordered state down to the lowest measured temperature 50 mK [25,26]. $Tb_2Ti_2O_7$ is one of the candidates for a spin liquid state with no transition to an ordered state and magnetic correlations of the order of intra-atomic distances [27,28]. $Gd_2Ti_2O_7$ with $|\frac{\theta_{cw}}{T_c}| \approx 10$ shows many interesting phases under an applied magnetic field [29, 30]. $Yb_2Ti_2O_7$ with Curie-Weiss temperature of about 0.75 K, shows a first order liquid-gas like transition at $T_c$=0.25 K which is unique among magnetic systems [31].

Among these compounds, the spin ice materials $Ho_2Ti_2O_7$ and $Dy_2Ti_2O_7$ and spin liquid $Tb_2Ti_2O_7$ have been subjected to extensive studies. The experimental studies show that these compounds have quite different properties [26, 27]. However, from a theoretical point of view, the magnetic moments of $Tb^{3+}$ , $Ho^{3+}$ and $Dy^{3+}$ have the same symmetry (Ising like) at low temperatures and similar interacting Hamiltonians [32, 33]. Hence, any theoretical framework that explains one of these compounds has to explain the other compounds as well. However, theoretical calculations show that the spin ice systems $Ho_2Ti_2O_7$ and $Dy_2Ti_2O_7$ are described by the same theory and $Tb_2Ti_2O_7$ fails to follow this theory [32] . Hence, the question: "what is the source of the difference between the spin ice systems and $Tb_2Ti_2O_7$?". Answering this question can give the clue for deriving a proper theoretical framework describing the novel properties of $Tb_2Ti_2O_7$. Hence, in the next two sections we describe the experimental properties and present theories for $Ho_2Ti_2O_7$, $Dy_2Ti_2O_7$, and $Tb_2Ti_2O_7$.

## 1.2 Spin Ice Systems $Ho_2Ti_2O_7$ and $Dy_2Ti_2O_7$

Before we begin presenting the experimental and theoretical results for $Ho_2Ti_2O_7$ and $Dy_2Ti_2O_7$, we review their chemical structure. In $Ho_2Ti_2O_7$ and $Dy_2Ti_2O_7$, $Ho^{3+}$ and $Dy^{3+}$ ions, along with $Ti^{4+}$ ions, make two interpenetrating pyrochlore lattices. However, the last shell of $Ti^{4+}$ ions is full which makes $Ti^{4+}$ non-magnetic and hence, $Ti^{4+}$ ions do not contribute to the magnetic properties of these compounds. In contrast to $Ti^{4+}$ ions, in the $4f$ shell of $Ho^{3+}$ and $Dy^{3+}$ ions, there are 9 and 10 electrons in the $f$ orbitals respectively and, depending on their interaction with the crystalline environment the single ion ground state can be magnetic. The local chemical environment of $Ho^{3+}$ and $Dy^{3+}$ in $Ho_2Ti_2O_7$ and $Dy_2Ti_2O_7$ consists of eight $O^{2-}$ ions which form a distorted cubic environment, with two oxygens along one diagonal ($\langle 111 \rangle$ direction) which are closer to $Ho^{3+}$ and $Dy^{3+}$ than the other oxygens (Fig. 1.6) [25, 35]. Although these $O^{2-}$ ions are non-magnetic, the electrostatic interaction between these oxygens and the angular momentum $L$ of $Ho^{3+}$ and $Dy^{3+}$ change the magnetic properties of $Ho^{3+}$ and $Dy^{3+}$ ions as we briefly explain in the next paragraph (for a discussion on this effect, which is called the crystal field effect, see Chapter 2).

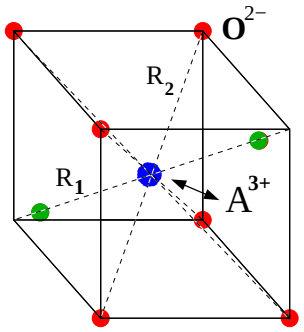


Figure 1.6: The distorted cubic environment of $A^{3+}$ in $A_2Ti_2O_7$ where A= Dy, Ho, Tb. Oxygens are shown with red and green circles.

For a free $Ho^{3+}$ or $Dy^{3+}$, all the electronic states with different $J^z$ are degenerate. However, the distorted cubic environment of oxygens removes this degeneracy and, because of the distortion along the $\langle 111 \rangle$ direction, the magnetic moments of $Ho^{3+}$

and $Dy^{3+}$ point towards the local $\langle 111 \rangle$ direction. A crystal field calculation of $Ho^{3+}$ and $Dy^{3+}$ that considers the local environmental oxygens confirms this picture and in the $|J, m_J\rangle$ basis, finds to be predominantly $|8, \pm 8\rangle$ and $|\frac{15}{2}, \pm\frac{15}{2}\rangle$ as the ground state of $Ho^{3+}$ and $Dy^{3+}$, respectively [35]. These states are separated by a large gap of a few hundred Kelvin to the first crystal field excited state [35]. Because there is no **J** matrix element between the two states of the ground state doublet, in temperatures much lower than the crystal field gap, $Ho^{3+}$ and $Dy^{3+}$ ions behave like local $\langle 111 \rangle$ Ising spins on the pyrochlore lattice.

This $\langle 111 \rangle$ Ising behavior has been observed in the magnetization data of $Ho_2Ti_2O_7$ and $Dy_2Ti_2O_7$. In Fig. 1.7 the magnetization data of $Dy_2Ti_2O_7$ in high symmetry directions [100], [110] and [111] is plotted. This data shows that for a high magnetic field the magnetization in [100], [110] and [111] directions converges respectively to $\frac{1}{\sqrt{3}}g\langle J^z\rangle$=5.77$\mu_B$/Dy, $\frac{1}{\sqrt{6}}g\langle J^z\rangle$=4.08$\mu_B$/Dy and $\frac{1}{3}g\langle J^z\rangle$=3.33$\mu_B$/Dy ($g$ is the Landé factor) consistent with Ising assumption [36,37]. This saturation is understandable because in high magnetic fields, where the Zeeman energy is more than the interaction between ions, the magnetization is controlled by the single ion properties. Also inelastic neutron scattering of $Ho_2Ti_2O_7$ confirms the $\langle 111 \rangle$ Ising behavior for $Ho^{3+}$ [35].

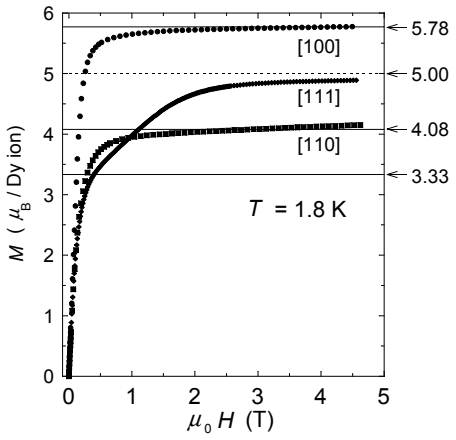


Figure 1.7: Magnetization data of $Dy_2Ti_2O_7$ for the high symmetry directions [100], [110] and [111]. These magnetization are consistent with the local $\langle 111 \rangle$ Ising spins on a pyrochlore lattice [36].

After investigating the single ion properties of $Ho^{3+}$ and $Dy^{3+}$, the next step is to determine the interactions between these magnetic ions. The Curie-Weiss temperatures of $Ho_2Ti_2O_7$ and $Dy_2Ti_2O_7$ (Curie-Weiss temperature gives an estimate of the strength of the coupling between magnetic ions) are respectively 2.5 K and 1.4 K (Appendix A). This shows that the effective interaction between these magnetic ions is ferromagnetic. To find the origin of this ferromagnetic interaction we recall that the crystal field ground states of $Ho_2Ti_2O_7$ and $Dy_2Ti_2O_7$ are mostly made of $|8, \pm 8\rangle$ and $|\frac{15}{2}, \pm\frac{15}{2}\rangle$ and hence the diagonal matrix elements of $J^z$ in the crystal field ground state are large. As a result, the dipole-dipole interaction in these compounds is important. To estimate the strength of this interaction we need to calculate the magnetic moments of these ions. The magnetic moment of a magnetic ion in the ground state is related to the other physical quantities by $\boldsymbol{\mu} = \mu_B g \langle \mathbf{J} \rangle$, where $g$ is the Landé factor equal to $\frac{5}{4}$ and $\frac{4}{3}$, respectively, for $Ho^{3+}$ and $Dy^{3+}$ and $\langle \mathbf{J} \rangle$ is the matrix element of the total angular momentum $\mathbf{J}$ in the crystal field ground state. Substituting the proper values of these quantities, one finds a magnetic moment of approximately 10 $\mu_B$ for both $Ho^{3+}$ and $Dy^{3+}$. Calculating the dipole-dipole coupling created by these moments gives a value of about 2.5 K at nearest neighbor separation (Appendix A), larger than the Curie-Weiss temperature of these compounds.

Yet, the dipole-dipole interaction is not the only interaction, as the overlap between $f$ orbitals gives an exchange interaction between magnetic ions. Considering that the exchange coupling of nearest neighbors is much larger than exchange coupling of other neighbors, one can calculate the nearest neighbor exchange coupling using the Curie-Weiss temperatures of these compounds. The details of such calculations are given in Appendix A and we give here the obtained values of these couplings for $Ho_2Ti_2O_7$ and $Dy_2Ti_2O_7$ which are -0.5 K and -1.1 K respectively. Therefore, the total magnetic interaction Hamiltonian for these compounds is the sum of the antiferromagnetic exchange interaction and the dipole-dipole interaction. At nearest neighbor separations, the sum of the dipole-dipole interaction and the exchange interaction gives a ferromagnetic coupling between $\langle 111 \rangle$ Ising spins.

We explained in Section 1.1 that the antiferromagnetic spins on the pyrochlore

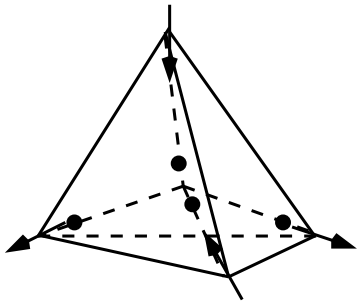

Figure 1.8: Mapping the two-in/two-out state on a tetrahedron to the two-close/two-far state in ice $I_H$.

lattice are frustrated and while it is not for geometrically interacting ferromagnetic spins. Hence, frustration in these compounds seems inconsistent with the fact that the interaction between Ising spins is ferromagnetic. This discrepancy was first explained by Harris *et. al*, who noticed that the $\langle 111 \rangle$ Ising spin on the pyrochlore lattice can be mapped to water ice $I_H$ [25]. To explain this, we plot in Fig. 1.8 the arrangement of one molecule of water ice $I_H$ and a single tetrahedron with four $\langle 111 \rangle$ Ising spins on its vertices. In this plot we can easily realize that the "in" and the "out" states of the Ising spins can be mapped to the "close" and "far" positions of the protons in ice $I_H$ . The ground state of these four spins with ferromagnetic interaction between them is the two-in/two-out state similar to the ground state of ice $I_H$, two-close/two-far state. As a result, the ground state of Ising spins with effective ferromagnetic nearest neighbor interaction on the pyrochlore lattice can be mapped to the water ice $I_H$ and is found to be frustrated. Because of this Harris *et. al.* coined the name of *spin ice* for this kind of system [25]. As in to the disordered ground state in ice $I_H$, neutron scattering experiments and muon spin resonance experiments on spin ice systems show no transition to an ordered state down to the lowest measured temperature (50 mK) [25]. In Fig. 1.9(a) we show the experimental neutron scattering data of $Ho_2Ti_2O_7$ at 50 mK [38]. This pattern has a highest intensity peak around (003) and (3/2,3/2,3/2) with no magnetic Bragg peak indicating an ordered state. Also, the specific heat measurements on spin ice systems $Ho_2Ti_2O_7$ and $Dy_2Ti_2O_7$ reveal that these systems have residual entropy close to $\frac{R}{2}\ln(\frac{3}{2})$ [34, 38]. This determination of residual entropy was not originally

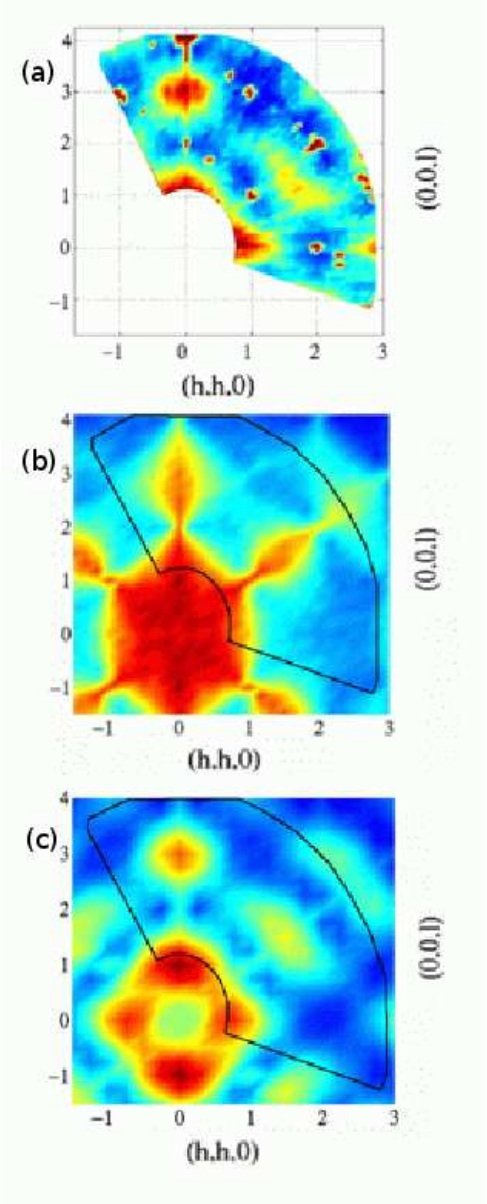


Figure 1.9: (a) Experimental elastic neutron scattering data of $Ho_2Ti_2O_7$ in (hhl) plane at 50 mK. (b) Calculated neutron scattering using Monte Carlo with nearest neighbor exchange interaction at $T$= 0.15J. (c) Calculated neutron scattering using Monte Carlo with antiferromagnetic exchange and dipole-dipole interactions at $T$=0.6 K [38].

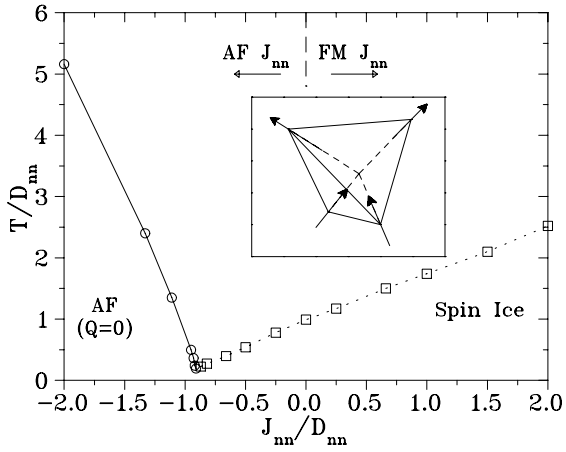


Figure 1.10: Phase diagram of local $\langle 111 \rangle$ Ising spins on the pyrochlore lattice as a function of ratio between nearest neighbor exchange $J_{\rm nn}$ coupling to the dipole-dipole coupling at nearest neighbor $D_{\rm nn}$. The inset show the two-in/two-out structure on a tetrahedron [32].

obvious for $Ho_2Ti_2O_7$, because of a Schottky anomaly in the specific heat data related to the nuclear hyperfine contribution of $Ho^{3+}$ ion. It was after subtracting the contribution of this Schottky anomaly that specific heat measurements confirmed the spin ice state for $Ho_2Ti_2O_7$ [38].

Monte Carlo calculations of elastic neutron scattering using only the nearest neighbor exchange Hamiltonian and the dipole-dipole Hamiltonian, show that including the dipole-dipole interaction, and treating it with the Ewald method are necessary to derive correct correlations for spin ice system $Ho_2Ti_2O_7$ [38]. Also, using Monte Carlo simulations, the phase diagram of spin ice systems with dipole-dipole and antiferromagnetic exchange interactions was obtained (Fig. 1.10) [32]. In this phase diagram, the temperature divided by the dipole-dipole coupling at nearest neighbor $D_{\rm nn}$ as a function of ratio between the exchange coupling $J_{\rm nn}$ and $D_{\rm nn}$ is plotted. Two phases are found: the $Q = 0$, all-in/all-out phase for $\frac{J_{\rm nn}}{D_{\rm nn}} <$ -0.91 and the frustrated spin ice phase for $\frac{J_{\rm nn}}{D_{\rm nn}} >$ -0.91. The $Q = 0$, all-in/all-out phase is an ordered phase on the pyrochlore lattice with either all spins pointing in or out of the tetrahedra. Incorporating loop moves in the Monte Carlo calculation

gives a phase transition from a disorder spin ice state to a so-called "Melko phase" at $T_c \cong 0.077 D_{\rm nn}$=180 mK [39]. In this calculation flips of the Ising spins on closed loops of the pyrochlore lattice is added to the Monte Carlo calculations. This loop dynamics is such that it obeys two-in/two-out, ice rule. This transition is independent of the exchange coupling $J_{\rm nn}$ and hence it is the same for both $Ho_2Ti_2O_7$ and $Dy_2Ti_2O_7$. This phase is a $Q = 001$ phase with the two tetrahedra in each unit cell being in the same two-in/two-out state and the Ising spins on the other two tetrahedra being flipped compared to the first two tetrahedra (Fig 1.11).

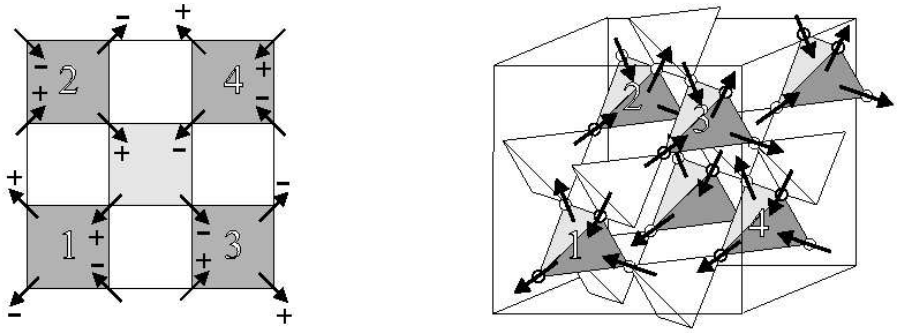


Figure 1.11: Ordered phase of spin ice system "Melko phase". The left hand panel shows the projection of spins to the xy plane [39].

One of the remaining puzzles in these compounds is the predicted exchange coupling of $Ho_2Ti_2O_7$ using the experimental DC susceptibility results [40, 41], which give $J_{\rm nn}$=-1.92 K. This coupling is inconsistent with the exchange coupling derived from fitting the Monte Carlo specific heat to the experimental data [38]. We address the source of this discrepancy in Appendix A.

## 1.3 Spin Liquid $Tb_2Ti_2O_7$

In the previous section, some experimental and the theoretical results on spin ice systems were presented. In this section, we give a brief description of the experimental results of $Tb_2Ti_2O_7$ to expose similarities and differences with the

spin ice systems $Ho_2Ti_2O_7$ and $Dy_2Ti_2O_7$. We use the results of this comparison to find a clue for understanding the physics of $Tb_2Ti_2O_7$.

In $Tb_2Ti_2O_7$ with space group $Fd\bar{3}m$, $Ti^{3+}$ and $O^{2-}$ are non-magnetic and $Tb^{3+}$ ions with 8 electrons in the $4f$ shell ($L$=3 and $S$=3 and spectroscopic symbol $^7F_6$) are magnetic. Muon spin resonance [27] and diffuse neutron scattering [27, 28] experiments show that $Tb_2Ti_2O_7$ does not order down to 50 mK, more than 280 times smaller than the estimated Curie-Weiss temperature $\theta_{\rm cw} = -14$ K estimated from DC susceptibility [33]. Considering the negative $\theta_{\rm cw}$, one would naively conclude that the effective interaction between $Tb^{3+}$ ions in $Tb_2Ti_2O_7$ is antiferromagnetic. The antiferromagnetic Heisenberg model on the pyrochlore lattice is frustrated as we discussed in Section 1.1 and as a result, magnetic correlations should remain short ranged and the system failing to order. Although at first glance this picture seems plausible, experimental and theoretical results reveal another scenario [27, 33, 43]. These results show that the single ion crystal field levels of $Tb^{3+}$ are similar to $Ho^{3+}$ and $Dy^{3+}$ ions in the spin ice systems $Ho_2Ti_2O_7$ and $Dy_2Ti_2O_7$, with an Ising-like magnetic doublet in the ground state which is separated from the first excited states by a 18 K gap [27, 33].

As with the spin ice systems, neglecting the effect of crystal field excited states at temperatures $T \ll \theta_{\rm cw}$, one can map the two states of the crystal field ground state to local $\langle 111 \rangle$ Ising spins. The ground state of local $\langle 111 \rangle$ Ising spins on a single tetrahedron is the all-in/all-out state in which either all Ising spins are towards or outwards of the tetrahedron (Fig. 1.12) and, as we explained before, these states are not frustrated. Considering the long-range nature of the dipole-dipole interaction and the known dipole-dipole and exchange couplings for $Tb_2Ti_2O_7$, which are $D_{\rm nn}$=0.5 K and $J_{\rm nn}$=-0.53 K, put $Tb_2Ti_2O_7$ ($\frac{J_{\rm nn}}{D_{\rm nn}}$=-1.07) in the all-in/all-out state with a phase transition temperature of about 1 K (Fig. 1.10). However, interestingly, for the given dipole-dipole and exchange couplings, $Tb_2Ti_2O_7$ is very close to the boundary of spin ice and all-in/all-out state, hence any small perturbation can move $Tb_2Ti_2O_7$ to the spin ice phase.

Before we proceed, we comment on the notation for dipole-dipole and exchange couplings that was previously used for spin ice system [32] and the notation for $Tb_2Ti_2O_7$ that we use in the rest of this thesis. In spin ice systems the dipole-dipole

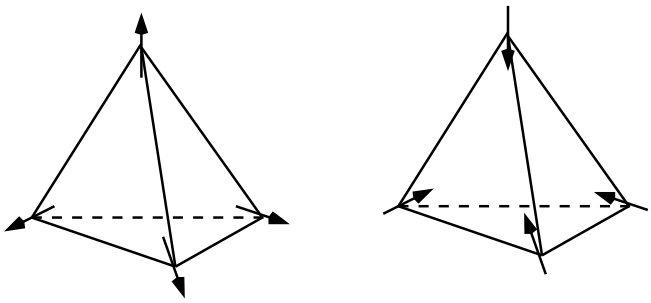

Figure 1.12: The ground state of antiferromagnetic local $\langle 111 \rangle$ Ising spins on a single tetrahedron (all-in/all-out state). This state is not frustrated on the pyrochlore lattice.

and the exchange couplings between Ising spins are respectively $D$ and $J$ and they are related to $D_{\rm nn}$ and $J_{\rm nn}$ by $D_{\rm nn} = \frac{5}{3}D$ and $J_{\rm nn} = \frac{1}{3}J$. In our notation the dipole-dipole and the exchange couplings between $Tb^{3+}$ ions are denoted respectively by $\mathcal{J}$ and $\mathcal{D}$ and this notation is related to the previous notation by $J = \mathcal{J}|\langle J^z \rangle|^2$ and $D = \mathcal{D}|\langle J^z \rangle|^2$, where $|\langle J^z \rangle|$ is the diagonal matrix element of $J^z$ in the ground state doublet. Also, in our notation, positive exchange means antiferromagnetic coupling opposite to the spin ice notation in which positive exchange means ferromagnetic coupling. The dipole-dipole coupling can be obtained using $\mathcal{D} = (\frac{\mu_0}{4\pi})\frac{(g_s \mu_{\rm B})^2}{r_{\rm nn}^3}$, where $\mu_0$=$4\pi \times 10^{-7}$ H/m is the vacuum permeability, $g_s = \frac{3}{2}$ is the Landé factor for $Tb^{3+}$, $\mu_{\rm B} = 9.27 \times 10^{-24}$ J/T is the Bohr magneton and $r_{\rm nn}$ is the nearest-neighbor distance between magnetic ions equal to 3.59 Å [27]. Substituting these values we obtain $\mathcal{D}$=0.0315 K. The exchange coupling can be obtained using $\mathcal{J} = \frac{-3\theta_{\rm cw}}{zJ(J+1)}$ [29], where $z$ is the number of nearest neighbor and $J$=6 is the total angular momentum. We assume a needle-shaped sample with $\theta_{\rm cw}$=-14 K [33] (negative sign shows that exchange interaction is antiferromagnetic) and obtain $\mathcal{J}$=0.167 K. Now we continue our discussion about the ground state of $Tb_2Ti_2O_7$ based on the $\langle 111 \rangle$ Ising spins on the pyrochlore lattice.

We mentioned that with the given dipole-dipole and exchange couplings for $Tb_2Ti_2O_7$, this compound should be in the all-in/all-out phase. However, this compound is close to the boarder of the all-in/all-out and spin ice phases and any small perturbation can move it to the spin ice phase or maybe make a quite

distinct frustrated state. To find what perturbations are at play in this system, we review the experimental results of $Tb_2Ti_2O_7$ and address the key question: "why is $Tb_2Ti_2O_7$ frustrated?".

In Fig. 1.13, muon spin relaxation ($\mu$SR) rate as a function of temperature is plotted down to 70 mK [27, 42]. The muon spin relaxation ($1/T_1$) gives a scale for the spin fluctuations and the larger $1/T_1$ is, the slower are spin fluctuations. Two regions of fluctuations are observed, the fast fluctuation limit for $T > 10$ K and the slow fluctuations limit for $T < 2$ K, until the lowest measured temperature of 70 mK. No peak is observed in these plots, which is a sign of no phase transition into an ordered state [44]. In the inset of the left hand figure, the muon polarization as a function of time is plotted for different temperatures. The exponential behaviour of the polarization as a function of time for each temperature shows that system is in the paramagnetic phase with no clear sign of glassy behaviour which would give stretched exponential relaxation. We should mention that often in the case of a long-ranged ordered system, the muon polarization oscillates as a function of time [44]. Other $\mu$SR experiments on the diluted samples $(Tb_pY_{1-p})_2Ti_2O_7$ (Fig. 1.13)

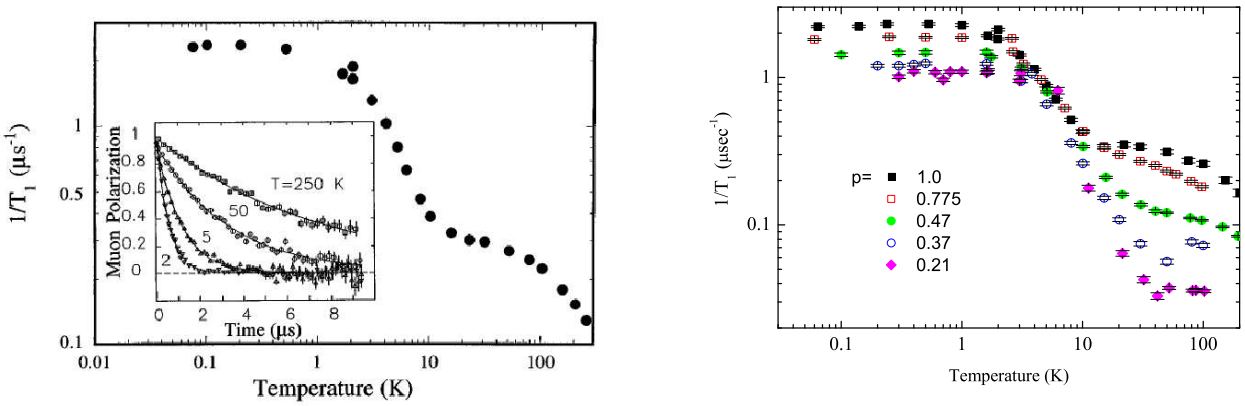


Figure 1.13: Muon spin relaxation of $Tb_2Ti_2O_7$ and $(Tb_pY_{1-p})_2Ti_2O_7$ for different percentage of dilution. In this graph the muon spin relaxation is plotted as a function of temperature [27, 42]. Notice that the percolation threshold for pyrochlore lattice is $R$=0.39.

show that the muon relaxation rate changes with dilution, however, the percolation threshold ($R_c$=0.39) does not signal any dramatic changes [42]. This may suggest that the magnetic ions in $Tb_2Ti_2O_7$ make small magnetic clusters insensitive to the percolation threshold. Also, it is worthwhile to mention that unless $T$=4 K, quantum fluctuations increase with increased dilution [42]. This means that there are weak correlations among magnetic clusters but these correlations are not strong enough to cause a phase transition in the system.

Although $\mu$SR experiments provide some information about $Tb_2Ti_2O_7$, other experimental evidences are needed to confirm the results of $\mu$SR and give some new information for understanding this system. In this context, the neutron scattering experiments have been done on this compound. Fig. 1.14 shows the diffuse neutron scattering of $Tb_2Ti_2O_7$ at 9 K and 60 mK [27, 28]. A broad region of high intensity

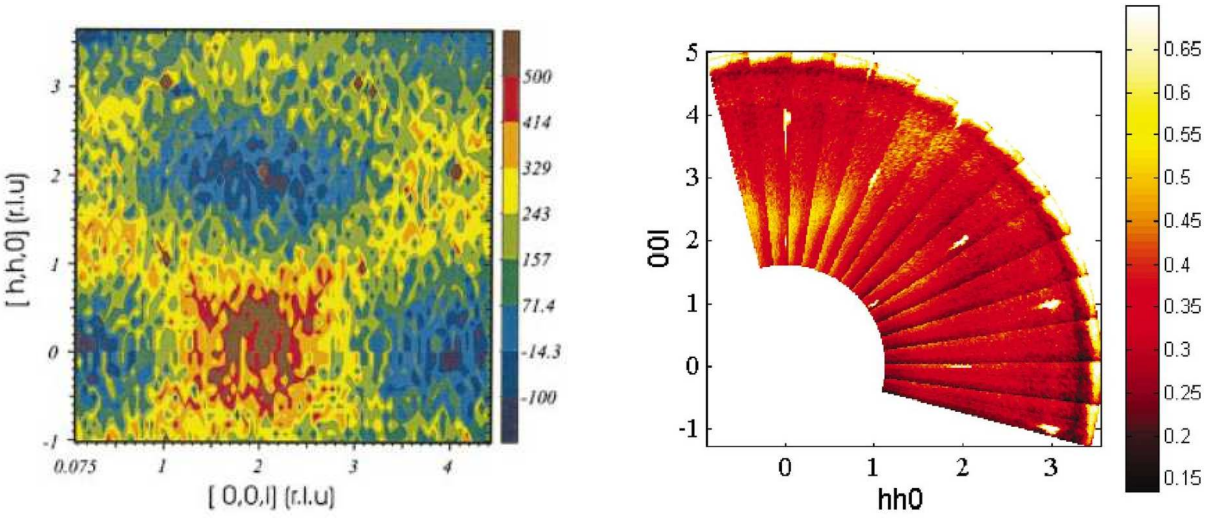


Figure 1.14: Diffuse neutron scattering of $Tb_2Ti_2O_7$ at $T$=9 K (left figure) and $T$=60 mK (right figure). Both data show a broad region around (002) which indicates correlations remain short ranged at least down to 60 mK [28, 43].

is observed around (002) without any change from 9 K to 60 mK. The broadness of diffuse neutron scattering around (002) shows that the magnetic correlations in $Tb_2Ti_2O_7$ are very short ranged. This can be verified qualitatively by noting that

the diffuse neutron scattering is well described by $\frac{\sin(Qr_{ij})}{Qr_{ij}}$ [43] at 2.5 K, which is the derived scattering function with magnetic correlations truncated at nearest neighbor. The inclusion of magnetic correlations from further neighbors (using the more general formula $\sum_{ij}\langle S_i S_j\rangle \frac{\sin(Qr_{ij})}{Qr_{ij}}$) adds extra terms which result in a qualitatively inconsistent pattern with the experiments [43]. Hence, the magnetic correlations in $Tb_2Ti_2O_7$ remain short ranged and of the order of nearest neighbor distance. We should mention that the diffuse neutron scattering of $Tb_2Ti_2O_7$ is qualitatively different from the neutron scattering of spin ice systems. In spin ice systems the highest intensity is located at (003) and (3/2,3/2,3/2) and these region of high intensity are not as broad as the highest intensity region in $Tb_2Ti_2O_7$ at (002). After this short note about the diffuse neutron scattering results of $Tb_2Ti_2O_7$, we discuss experimental inelastic neutron scattering of $Tb_2Ti_2O_7$ results which give information about the magnetic excitations in this compound.

Inelastic neutron scattering results give some $Q$-independent excitations related to the crystal field states [27,43]. The three lowest crystal field states are observed at 18, 126, and 175 K which explain that the crystal field ground state is connected to the three lowest excited states by $J^+$, $J^-$ or $J^z$ matrix elements [27, 43]. The excitations from the ground state to the first excited states show dispersion as a function of $Q$ for $T < 30$ K, while, the excitations from the ground state to the other excited states are dispersionless [43].

To find the crystal field Hamiltonian which describes the single ion excitations of $Tb_2Ti_2O_7$, a crystal field calculation is reported in Ref. [33]. In this calculation the point charge approximation as well as ab-initio methods were employed. It was shown that the crystal field ground state doublet is predominantly made of $|\pm 4\rangle$ and the first excited state doublet is mostly made of $|\pm 5\rangle$ [33]. This doublet-doublet picture is consistent with the susceptibility results of $Tb_2Ti_2O_7$ and $(Tb_{0.02}Y_{0.98})_2Ti_2O_7$ and, also with the magnetic moment in the ground state equal to 5 $\mu_B$ estimated via $\mu$SR experiments [33].

So far, we have discussed the experiments that probe the microscopic properties of $Tb_2Ti_2O_7$. However, it is always useful to study the bulk experimental properties of a physical system such as specific heat and also the physical properties of $Tb_2Ti_2O_7$ under further external perturbations such as pressure and magnetic field.

These studies can give key information such as residual low temperature entropy and the response of the system to different perturbations.

The specific heat results of $Tb_2Ti_2O_7$ show two broad peaks and one sharp peak. In Reference [33], the broad peaks are reported to occur at $T$=1.5 K and $T$=6 K while in reference [45], they are reported to occur at $T$=0.7 K and $T$=5 K (Fig. 1.15). The sharp peak is observed at $T$=0.37 K which may suggest a phase transition to ordered state [45]. Deriving the entropy from these specific heat results confirms the doublet-doublet scheme [33]. However, the entropy at high temperatures still does not recover $R\ln(4)$ [33, 45], which could be interpreted as a sign of residual entropy in the ground state. The observed lower temperature peaks in the specific heat data can be associated with the low energy manifold of states made from interactions between crystal field ground states. The higher temperature peak can be associated with the first crystal field excited state which is broadened by the magnetic correlations between $Tb^{3+}$ ions. The sign of phase transition (sharp peak in the specific heat data at 0.37 K) is observed at AC [45] and DC [46] susceptibility measurements. These results show a spin glass phase transition which in references [45] and [46] are reported to arise at $T$=0.2 K and 0.07 K, respectively. However, as was discussed earlier this transition is not observed in the $\mu$SR and neutron scattering experiments.

The diffuse neutron scattering experiment of $Tb_2Ti_2O_7$ under pressure shows the liquid-solid like transition for $Tb_2Ti_2O_7$ under high pressures [47]. This transition starts to develop at $T$=2.1 K under a pressure of 1.5 GP. At this pressure, the Bragg peaks begin to appear at reciprocal points such as $Q$=100, 110, 210 and 211 and become sharper with increasing pressure. However, the presence of diffuse neutron scattering along with Bragg peaks shows that the system is not fully ordered. An analysis of the Bragg peaks show that this order state is antiferromagnetic with an ordering wave vector of either $\mathbf{k}$= 100 or 110. The x-ray experiment under the pressure reveals no structural phase transition [47]. Hence, the liquid-solid transition can be associated with the change of interacting couplings among the $Tb^{3+}$ ions and maybe the spin-lattice coupling. Applying anisotropic stress via large uniaxial pressure produces a transition to a Néel ordered state [48]. The Néel ordered state is not stable under an applied magnetic field and, for magnetic

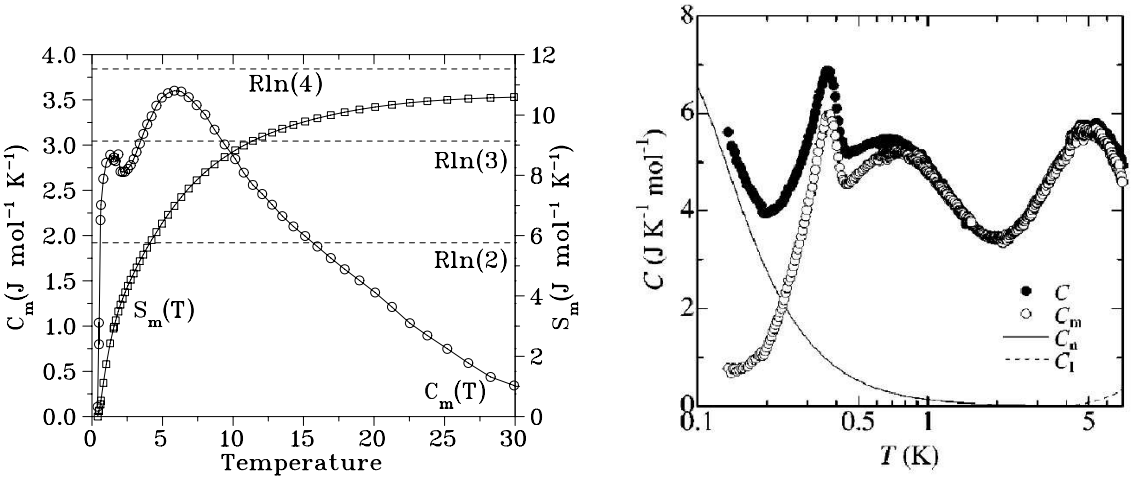


Figure 1.15: The specific heat of $Tb_2Ti_2O_7$ as a function of temperature. Two broad peaks is observed in the left figure and two broad peaks and one sharp peaks are observed in the right figure. The sharp peak at 0.37 K (in the left figure) can be a sign of phase transition [33, 45].

fields more than 0.6 T, this ordered state change from antiferromagnetic to canted ferromagnetic [48].

$Tb_2Ti_2O_7$ has also been investigated under an external magnetic field **B**. The magnetization measurements of $Tb_2Ti_2O_7$ with **B** applied along different high cubic symmetry directions, [100], [110] and [111], is shown in Fig. 1.16 [37]. The lack of anisotropy reveals that $Tb^{3+}$ ions behave more like Heisenberg spins than Ising spins (inset of Fig. 1.16), inconsistent with the crystal field ground state which predicts Ising spins for $Tb^{3+}$. In Fig. 1.17 we show the diffuse neutron scattering of $Tb_2Ti_2O_7$ under an applied magnetic field along the [110] direction [51]. These results show that with increasing the magnetic field, the highest intensity around (002) starts to sharpen and above $B$=2 T, it changes to a Bragg peak. Also, with increasing the magnetic field, a diffuse scattering along with a Bragg peak starts to emerge near (211). In the ordered phase, spin waves are observed which is a further evidence that the magnetic moments are isotropic and not Ising like.

Investigating the properties of $Tb_2Ti_2O_7$ under different perturbations, the ques-

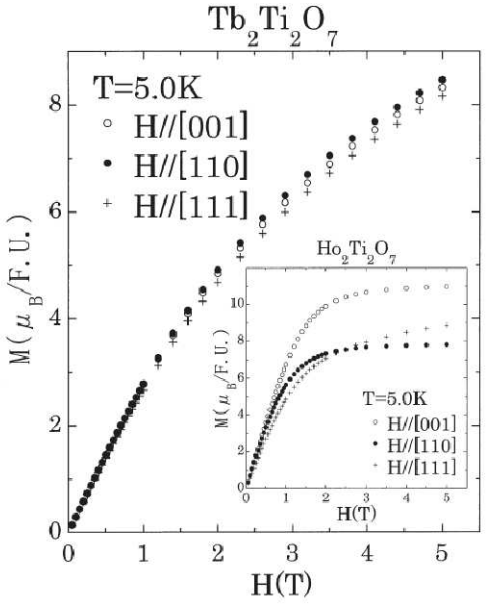


Figure 1.16: Magnetization of a single crystal of $Tb_2Ti_2O_7$ along the high symmetry directions [100], [110] and [111]. These data show the isotropic behavior for $Tb^{3+}$ moments. In the inset the magnetization data of a single crystal of $Ho_2Ti_2O_7$ in the high symmetry directions [100], [110] and [111] is shown. This result is evidence for $\langle 111 \rangle$ Ising spin behavior for the $Ho^{3+}$ moments [37].

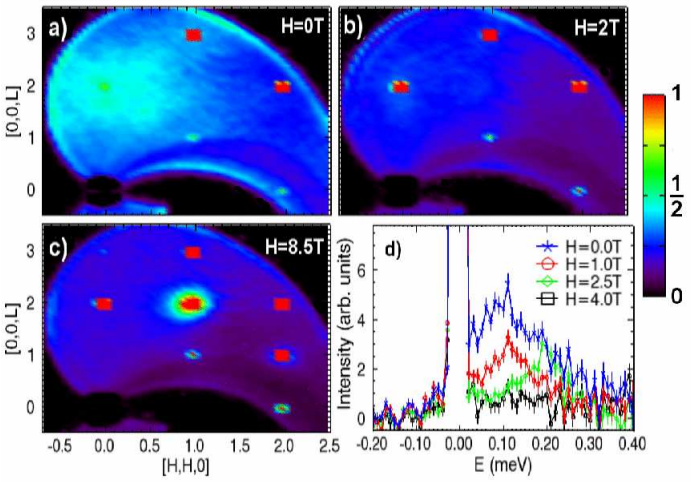


Figure 1.17: Diffuse neutron scattering of $Tb_2Ti_2O_7$ in the (hhl) plan and at 1 K and under the magnetic field with strength (a) $B$=0 T, (b) $B$=2 T and (c) $B$=8 T. (d) The integrated scattering over $Q$ as a function of energy at T=0.1 K [51].

tion arises as to how $Tb_2Ti_2O_7$ behaves when we perturb the structure of this system by replacing the non-magnetic ions $Ti^{3+}$ with other non-magnetic ions. This substitution changes the lattice size and this affects the magnetic properties of the system. This experiment was done by substituting $Ti^{3+}$ with $Sn^{3+}$ in $Tb_2Ti_2O_7$ to give $Tb_2Sn_2O_7$. $Tb_2Sn_2O_7$, in contrast to $Tb_2Ti_2O_7$, shows a two-step phase transition to a long range ordered state. In the first step a smeared transition to a ferromagnetic phase arises at $T \simeq 1.3$ K, which is followed by a sharp transition at $T$= 0.87 K. These phase transitions have been observed via neutron diffraction studies [49]. Specific heat also shows a sharp peak at $T$= 0.87 K consistent with the sharp phase transition observed by neutron diffraction. Comparing the magnetic moments obtained from the specific heat, 3.3 $\mu_B$, and neutron scattering, 5.9$\mu_B$, reveals the persistence of quantum fluctuations of correlated spins in the ordered state [49]. The magnetic moment of $Tb^{3+}$ ions in specific heat data is calculated by fitting the experimental data to the nuclear Schottky anomaly. This fitting determines the hyperfine field and from it the value of 3.3 $\mu_B$ for $Tb^{3+}$ moment is obtained [49]. The observed missing magnetic moment from the macroscopic (specific heat) scale to microscopic scale (neutron scattering) may be related to the

correlations among the dynamic magnetic clusters. The presence of dynamics in $Tb_2Sn_2O_7$ is confirmed by $\mu$SR experiment which shows no transition to a long range ordered state [50].

To find whether $Tb_2Ti_2O_7$ is a disorder-free lattice, the x-ray absorption fine-structure and neutron powder-diffraction studies have been performed. The results of these experiments show that $Tb_2Ti_2O_7$ is a disorder-free pyrochlore lattice with oxygens and $Ti^{3+}$ at their exact position within experimental error and down to the measured temperature of 4.5 K [52]. Also, comparing the experimental results of $\mu$SR with DC susceptibility results show no sign of static lattice distortion in $Tb_2Ti_2O_7$ down to 70 mK [53]. In this experiment, the change in the local environment of the muons as a function of temperature is studied. This change can be related to the polarization of spin and also the distortion of the lattice and as a result, provides strong evidence for the absence of any distortion in the lattice.

On the theoretical side, mean field theory [54] and random phase approximation (RPA) calculation [55] have been used to find a qualitative description of the physical properties of $Tb_2Ti_2O_2$. In the, the full crystal field state has been used to calculate the neutron scattering of $Tb_2Ti_2O_7$ [55]. This calculation gives a qualitative description of the experimental diffuse neutron scattering of $Tb_2Ti_2O_7$ [55]. This is an evidence for the importance of excited crystal field states in describing the physical properties of this compound. On the other hand, this calculation does not give any clue to the source of frustration in this system. Also, a mean field calculation with $\langle 111 \rangle$ Ising spins with dipole-dipole and antiferromagnetic exchange interactions shows that the $\langle 111 \rangle$ Ising spins cannot predict the results of experimental neutron scattering of $Tb_2Ti_2O_7$ [54]. However, assuming a more isotropic spin model, such as Heisenberg spins with finite $\langle 111 \rangle$ anisotropy gives a neutron scattering pattern consistent with the neutron scattering results of $Tb_2Ti_2O_7$ [54].

From the presented experimental data and theoretical results we conclude that the $\langle 111 \rangle$ Ising Hamiltonian is unable to describe the low-energy physics of $Tb_2Ti_2O_7$. As a result, the magnetic behavior of $Tb_2Ti_2O_7$ is likely governed by another low energy Hamiltonian and the first goal of any theoretical work on this system must be to find this Hamiltonian. From this perspective, the facts that $Tb_2Ti_2O_7$ is close to the boundary between spin-ice and all-in/all-out state and that the experimental

evidence that the crystal field gap between the ground state and first excited states is small provide an important clues: Perhaps the crystal field excited states change the effective low energy physics of $Tb_2Ti_2O_7$ from Ising like. This is the main issue that we address in this thesis and we use some tools, such as effective Hamiltonian method (Chapter 3), to derive the low energy Hamiltonian of $Tb_2Ti_2O_7$ and attempt to give an explanation as to "why is $Tb_2Ti_2O_7$ frustrated?".

## 1.4 Structure of the Thesis

We begin with a review of the crystal field effect and how to derive the crystal field Hamiltonian based on the crystal structure and introduce a point charge approximation. We also derive the crystal field Hamiltonian of $Tb_2Ti_2O_7$ by rescaling the crystal field parameters of $Ho_2Ti_2O_7$. We show that the ground state of this Hamiltonian is made of a magnetic doublet separated from the first excited state doublet by a 18.7 K gap. We use the crystal field basis for constructing the effective Hamiltonian of $Tb_2Ti_2O_7$.

In Chapter 3 we review the tools for constructing the effective Hamiltonian of $Tb_2Ti_2O_7$ by introducing the Brillouin-Wigner perturbation theory, the Rayleigh-Schrödinger perturbation theory and the effective Hamiltonian method. Using the effective Hamiltonian method, we calculate in the forth chapter, the effective Hamiltonian of $Tb_2Ti_2O_7$ in the ground state doublet basis and, to the second order of perturbation theory, by integrating out the crystal field excited states. In the first order of perturbation theory we derive the $\langle 111 \rangle$ Ising Hamiltonian on a pyrochlore lattice similar to spin ice systems. We show that to second order in perturbation theory, the crystal field excited states of $Tb^{3+}$ ions renormalize the pair-wise interaction between $\langle 111 \rangle$ Ising spins derived in first order perturbation theory. This renormalization changes the effective interaction between Ising spins at nearest neighbor from antiferromagnetic to ferromagnetic and generates a frustrated $\langle 111 \rangle$ Ising Hamiltonian. We also show that the crystal field excited states create pair-wise transverse terms in the effective Hamiltonian and restore some isotropy of the magnetic moments in the effective Hamiltonian.

In Chapter 5, we study the phase diagram of $Tb_2Ti_2O_7$ with four lowest crystal field states and with the effective Hamiltonian within the independent tetrahedron approximation. This study helps us understand the effects of excited crystal field states on the phase diagram of a single tetrahedron of $Tb_2Ti_2O_7$. At this level of approximation, we find that the ground state of $Tb_2Ti_2O_7$ is mostly made of a linear combination of spin ice states (two-in/two-out), i.e. a *quantum spin ice*.

In Chapter 6 we use the experimental fact that the magnetic correlations in $Tb_2Ti_2O_7$ are of the order of nearest neighbor and calculate the diffuse neutron scattering of $Tb_2Ti_2O_7$ within the single tetrahedron approximation. We show that the inelastic scattering among the lowest energy states of the single tetrahedron, which are in the energy window of the experiment, are responsible for the diffuse neutron scattering in $Tb_2Ti_2O_7$. We propose an experiment based on diffuse neutron scattering to verify the underlying spin ice like nature of the low temperature regime of $Tb_2Ti_2O_7$.

In Chapter 7 we apply periodic boundary conditions to the effective Hamiltonian of $Tb_2Ti_2O_7$ in a cubic unit cell. We find the classical ground state of $Tb_2Ti_2O_7$ and show that it is a two-in/two-out spin ice state. This study helps us to figure out the ground state of $Tb_2Ti_2O_7$ in the presence of long-range dipole-dipole interaction and verify that in the thermodynamic limit, we still have the two-in/two-out state as the ground state.

In Chapter 8 we study the crystal field states of $Tb_2Ti_2O_7$ under magnetic field. We also calculate the magnetization of a single tetrahedron with four $Tb^{3+}$ ions and six lowest crystal field states. We show in the context of magnetization results that the combination of excited crystal field states and the interaction between $Tb^{3+}$ ions restores isotropy of the effective magnetic moments related to $Tb^{3+}$ ions. We propose an experiment based on the magnetization of $Tb_2Ti_2O_7$ in different symmetry directions to verify the spin ice like ground state in $Tb_2Ti_2O_7$.

Finally, in Chapter 9 we summarize the results of all chapters and give few proposals for future work.

In Appendix A we present a calculation of exchange interactions for spin ice materials $Ho_2Ti_2O_7$ and $Dy_2Ti_2O_7$ using the experimental DC susceptibility results

for these compounds. We obtain exchange interactions for $Ho_2Ti_2O_7$ and $Dy_2Ti_2O_7$ consistent with those derived exchange interactions by fitting the specific heat data of these compounds to experimental results. This calculation resolves the last puzzle as to whether $Ho_2Ti_2O_7$ is a spin ice, and confirms that this compound is a spin ice system.

# Chapter 2

# Crystal Field Effect in $Tb_2Ti_2O_7$

The crystal environment of a single magnetic ion in conjunction with its electronic structure determine the single ion magnetic levels and the symmetry of the magnetic ion in its electronic ground state. These single ion levels are key elements in understanding the magnetic properties of a magnetic system. In this chapter, we give a brief introduction to the crystal field effect for f-electron ions and determine the crystal field levels of $Tb^{3+}$ in $Tb_2Ti_2O_7$

The electrostatic interaction between the electrons of a magnetic ion and its environment in a crystal can lift the spatial degeneracy of the magnetic ion levels. This interaction can be written in terms of the angular momentum, $L$, and in the case of f-electron ions, where the spin-orbit interaction is strong, in terms of the total angular momentum, $J$. As previously mentioned, this effect, which is called the crystal field effect, plays an important role in understanding the magnetic properties of magnetic compounds [57, 58]. The interaction caused by this effect alongside the spin-orbit interaction are the main single-electron interactions in a magnetic ion. In ions with d-electrons in the outermost shell, the strength of the crystal field interaction is comparable with spin-orbit interaction and in f-electron ions this interaction is usually much smaller than the spin-orbit interaction [57]. As a result, in f-electron ions, the total angular momentum $\mathbf{J}$ is a good number and the crystal field effect can be treated perturbatively. Based on this, Stevens and others developed a method that substitutes different terms in the expansion of the

electrostatic interaction between the f-electrons and the environment with operators which are functions of the total angular momentum operator $J$ [58]. However, because of quantum effects and the extent of charges, this calculation is unfeasible and one needs to make some approximations. The simplest approximation for this is the point charge approximation where all the quantum effects and spatial extent of charges are neglected [58,59]. The obtained eigenvalues and eigenfunctions from this approximation give a good qualitative picture of the crystal field states. However, these results are not good enough to be considered as an accurate method for calculating physical quantities. Therefore, we need a more sophisticated method for calculating the crystal field which takes into account the quantum effects and the spatial extension of the environmental charges. To accomplish this, we use a semi-empirical method in which we write the most general crystal field Hamiltonian consistent with the environmental symmetry of the magnetic ion with a few unknown parameters that are determined from experimental results.

After this short introduction we present an overview of the organization of the different sections in this chapter. In the first section, we use the point charge approximation to derive the crystal field interaction in terms of the total angular momentum operator. We take into account the quantum effects and the spatial extension of the environmental charges by using a semi-empirical method. In the second section, we calculate the crystal field Hamiltonian of $Tb_2Ti_2O_7$ both in the point charge approximation and with the semi-empirical method. We also calculate the eigenvalues and eigenfunctions of the resulting Hamiltonian as well as the change of eigenvalues with the positions of the environmental ions.

## 2.1 Point Charge Approximation

In this section, we calculate the crystal field Hamiltonian of a rare earth ion with f-electrons as the outer shell and in a crystalline environment. We begin by using the point charge approximation where the three basic assumptions are [58, 59]:

- The overlap between the f-orbitals of the rare earth ion and surrounding ions is negligible.

- The only interaction between f electrons of the rare earth ion and other charges in the environment is the electrostatic interaction.
- All other ions and their electrons are treated as point charges sitting at their equilibrium positions in the crystal.

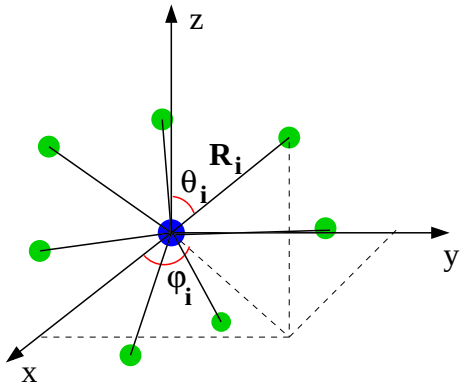


Figure 2.1: The crystal environment of the f-electron ion. The reference frame is usually chosen such that the f-electron ion is at the origin (blue sphere). The environmental ions are shown by green spheres.

We choose a reference frame such that the magnetic ion is at the centre of the coordinates (Fig. 2.1). In this reference frame, the electrostatic interaction between the environmental ions and f-electrons reads

$$V_{\rm cf} = -{\rm e}\sum_{ij}\frac{q_j}{4\pi\epsilon_0|\mathbf{r}_i-\mathbf{R}_j|}\ , \tag{2.1}$$

where $-$e is the electron charge, $q_j$ is the effective electric charge of ion $j$ at site $\mathbf{R}_j$, and $\mathbf{r}_i$ is the position of f-electron $i$. The sum over $j$ includes all the environmental charges of the rare earth element and the sum on $i$ is over all the f-electrons of the rare earth element. Due to the symmetries of the crystalline environment, it is useful to expand the crystal field Hamiltonian in terms of the spherical harmonics. Hence, the crystal field potential, in terms of spherical harmonics, reads

$$V_{\rm cf} = \sum_i\sum_{lm} A_l^m {r_i}^l Y_{lm}(\hat{\mathbf{r}}_\mathbf{i})\ , \tag{2.2a}$$

$$A_l^m = (-1)^m\frac{4\pi}{2l-1}\sum_j\frac{q_j}{R_j^{l+1}}Y_{lm}(\hat{\mathbf{R}}_j) \tag{2.2b}$$

where $Y_{lm}$ are spherical harmonics, $\hat{\mathbf{r}}_i$ is the radial unit vector at the position of f-electron $i$, and $\hat{\mathbf{R}}_j$ is the radial unit vector of position vector at the position of ion $j$, and the sum on $i$ is over all the f-electrons, $r_i$ is the radial distance of f-electron $i$ and the sum on $j$ is over all the environmental ions. Owing to of the symmetries of the crystalline environment, most of the terms in this expansion are zero and there are only a few non-zero terms that satisfy the symmetries of the crystalline environment. To avoid imaginary coefficients in the crystal field Hamiltonian, we define a new set of spherical harmonics such that,

$$Z_{n0} = Y_n^0 \,, \tag{2.3a}$$

$$Z_{nm}^c = \frac{1}{\sqrt{2}}[Y_n^{-m} + (-1)^m Y_n^m] \,, \tag{2.3b}$$

$$Z_{nm}^s = \frac{i}{\sqrt{2}}[Y_n^{-m} - (-1)^m Y_n^m] \,. \tag{2.3c}$$

In terms of this set of spherical harmonics, which are called tesseral harmonics, the crystal field Hamiltonian reads

$$V_{\rm cf} = \mathrm{e} \sum_i \sum_{n\alpha} {r_i}^n \gamma_{n\alpha} Z_{n\alpha}(x_i, y_i, z_i) \,, \tag{2.4a}$$

$$\gamma_{n\alpha} = \sum_{j=1} \frac{4\pi q_j}{2n+1} \frac{Z_{n\alpha}(\theta_j, \phi_j)}{R_j^{n+1}}, \tag{2.4b}$$

where $R_i$, $\theta_i$ and $\phi_i$ are respectively the distance, the polar angle and the azimuthal angle of ion $i$ in spherical coordinates (Fig. 2.1), $x_i$, $y_i$ and $z_i$ are the spatial coordinates of electron $i$, $n$ and $\alpha$ are determined by the symmetry of the environment of the magnetic ion (all $Z_{n\alpha}$ are zero, except those which are invariant under the symmetry of the environment), $Z_{n\alpha}$ represents both $Z_{nm}^c$ and $Z_{nm}^s$ and the sum on $i$ is over all f electrons. Because of the symmetry of $A^{3+}$ in $A_2Ti_2O_7$ (distorted cubic), $Z_{n\alpha}^s$ terms in Eq. (2.4a) are zero and from now on we use $m$ instead of $\alpha$ and $Z_{nm}$ instead of $Z_{nm}^c$. In rare earth elements, the spin orbit interaction is very strong and, as a result, the total angular momentum $J$ is a good quantum number and the eigenstates of the total angular momentum operator $\mathbf{J}$ are good states. Therefore, we calculate the crystal field Hamiltonian in the basis of total angular momentum $J$. To accomplish this, we write $Z_{nm}(x_i, y_i, z_i)$ in Cartesian form and

define new functions $f_{mn}$ as,

$$Z_{nm}(x_i, y_i, z_i) = (c)\frac{f_{nm}(x_i, y_i, z_i)}{{r_i}^n} \ . \tag{2.5}$$

where $c$ is given as a coefficient outside of the bracket in Table IV of Reference [59]. According to the Wigner-Eckart theorem, a simple relation exists between the matrix elements of this potential and functions of the matrix elements of the total angular momentum operator given by,

$$\sum_i f_{nm}(x_i, y_i, z_i) = \theta_n \langle r^n \rangle O_n^m \ , \tag{2.6}$$

where $\langle r^n \rangle$ is the expectation value of the radial distance, $\theta_2 = \alpha_J$, $\theta_4 = \beta_J$ and $\theta_6 = \gamma_J$ are Stevens' multiplicative factors and their values for different rare earth ions are given in References [58, 59]. $O_n^m$, which are called Stevens operators, are functions of total angular momentum and transform among each other like spherical harmonics. As an example, the matrix elements of $\sum_i (3z_i^2 - r_i^2)$ in the basis of $|LSJJ^z\rangle$ are related to the operator $\alpha_J \langle r^2 \rangle O_2^0$ as follows:

$$\langle LSJJ^z | \sum_i (3z_i^2 - r_i^2) | LSJJ^z \rangle = \alpha_J \langle r^2 \rangle \langle LSJJ^z | O_2^0 | LSJJ^z \rangle. \tag{2.7}$$

A list of Stevens operators for rare earth ions is given in References [58, 59]. Substituting Eq. (2.6) in Eq. (2.5) and Eq. (2.5) in Eq. (2.4a), the crystal field Hamiltonian in terms of the Stevens operators can be written as

$$H_{\rm cf} = \sum_{mn} [A_n^m \langle r^n \rangle \theta_n] O_n^m. \tag{2.8}$$

This equation is usually written in the following more compact form:

$$H_{\rm cf} = \sum_{mn} B_n^m O_n^m, \tag{2.9}$$

where the coefficients $B_n^m$ are crystal field parameters.

There are other popular conventions for writing the crystal field Hamiltonian. One of these conventions is based on tesseral operators [61]. These operators transform like Stevens operators and they are related to Stevens operators such that

for positive and negative $m$, Stevens operators are proportional to $C^c_{lm}$ and $C^s_{lm}$ respectively, where $C^c_{lm}$ and $C^s_{lm}$ are tensorial operators [63]. Because of the quantum effects and the complexity of the distribution of electric charge around each rare earth ion, crystal field parameters are hard to calculate and they are usually determined semi-empirically using experimental data. One of the ideal experimental methods for determining the crystal field parameters is inelastic neutron scattering [35]. In this method, the crystal field levels of the single magnetic ion are determined by measuring the change of energy of scattered neutrons at zero momentum transfer. The crystal field coefficients are obtained by fitting the eigenstates of the crystal field Hamiltonian to these energy levels. In the next section, we use the point charge approximation and semi-empirical method to determine the crystal field Hamiltonian of $Tb_2Ti_2O_7$.

## 2.2 Crystal Field Effects in $Tb_2Ti_2O_7$

In this section, we apply the results of the previous section to calculate the crystal field Hamiltonian in the point charge approximation and with the semi-empirical method. It was mentioned in the first chapter that the symmetry group of $Tb_2Ti_2O_7$ is $Fd\bar{3}m$. In this crystal structure, each $Tb^{3+}$ ion is surrounded by eight oxygens which make a distorted cubic environment such that two oxygens in one diagonal are closer to $Tb^{3+}$ ion than the other six oxygens (Fig. 2.2) [33]. The distance between the oxygens and the $Tb^{3+}$ ion were determined by x-ray experiment and they are $R_1$=2.2 $\mathring{A}$ and $R_2$=2.5 $\mathring{A}$, respectively [33]. The electric field of these oxygens at the $Tb^{3+}$ site creates a crystal field effect which we first calculate within the point charge approximation. We should mention that the effect of other ions in the environment of a $Tb^{3+}$ ion is much less than these eight oxygens because the crystal field parameters $B^m_n$ drop off as $\frac{1}{R^{(n+1)}}$ where $R$ is the distance between the $Tb^{3+}$ ion and other ions, and also because the densities of positive and negative charges at large $R$ are the same. In the following calculation, we choose the first sublattice of the FCC lattice with the two closer oxygens in the [111] directions. For the three other sublattices with easy axis towards $[\bar{1}\bar{1}1]$, $[1\bar{1}\bar{1}]$ and $[\bar{1}1\bar{1}]$, we have the same crystal field Hamiltonian with the difference that they

possess a different local easy axis related by the point group symmetry.

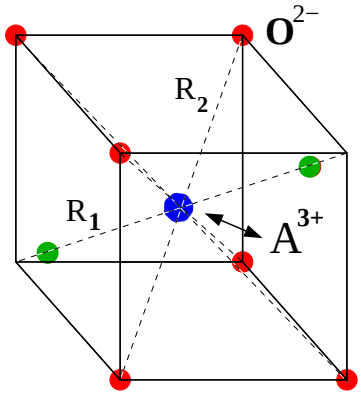


Figure 2.2: The crystal environment of $Tb^{3+}$ ion (blue sphere in the center) in $Tb_2Ti_2O_7$ is made of eight oxygens (red and green spheres in the vertices of the cube) which make a distorted cubic environment such that two oxygens (green) in one diagonal are closer to $Tb^{3+}$ ion than the other six oxygens (red) [33].

To find the crystal field Hamiltonian in the point charge approximation, one has to calculate the $\gamma_{nm}$ coefficients in Eq. (2.4b). The general formula for calculating these coefficients is

$$\gamma_{nm} = \sum_{j=1}^{8} \frac{4\pi q_j}{2n+1} \frac{Z_{nm}(\theta_j, \phi_j)}{R_j^{n+1}} \tag{2.10}$$

where $R_j$ is the distance between oxygen $j$ and the $Tb^{3+}$ ion and the sum is over the eight oxygens surrounding the $Tb^{3+}$ ion. Because the two oxygens in the $\langle 111 \rangle$ direction are closer to the $Tb^{3+}$ ion, they make a preferred axis for the $Tb^{3+}$ ion, we thus choose a local reference of frame such that the new z, y and x axis are respectively towards the $\frac{1}{\sqrt{3}}(1,1,1)$, $\frac{1}{\sqrt{2}}(1,\bar{2},0)$ and $\frac{1}{\sqrt{6}}(\bar{1},\bar{1},2)$ vectors of the global frame. The spherical coordinates of environmental oxygens in this local frame are given in Table 2.1.

By substituting these angles in Eq. (2.4b) we calculate $\gamma_{nm}$ coefficients in terms of the ratio of $R_2$ to $R_1$. Substituting these coefficients in Eq. (2.4a) and using Eq.

| Ion's index | 1 | 2 | 3 | 4 | 5 | 6 | 7 | 8 |
|---|---|---|---|---|---|---|---|---|
| R($\mathring{A}$) | 2.2 | 2.5 | 2.5 | 2.5 | 2.5 | 2.5 | 2.5 | 2.2 |
| $\theta$ (degree) | 0 | 70.53 | 70.53 | 70.53 | 109.47 | 109.47 | 109.47 | 180 |
| $\phi$ (degree) | 0 | 60 | -60 | 0 | 0 | 60 | -60 | 0 |

Table 2.1: The spherical coordinate of the environmental oxygens in the local axis with z, y and x axis are respectively pointed towards the $\frac{1}{\sqrt{3}}$(1,1,1), $\frac{1}{\sqrt{2}}$(1,$\bar{1}$,0) and $\frac{1}{\sqrt{6}}$($\bar{1}$,$\bar{1}$,2) directions (Fig. 2.2).

(2.6) the crystal field Hamiltonian reads,

$$\begin{aligned} V_{\rm cf} &= \alpha_J \tilde{B}_2^0 (r^3-1) O_2^0 + \beta_J \tilde{B}_4^0 [\frac{27r^5+1}{28} O_4^0 - 20\sqrt{2} O_4^3] \\ &+ \gamma_J \tilde{B}_6^0 [\frac{(243r^7+141)}{384} O_6^0 + \frac{35\sqrt{2}}{4} O_6^3 + \frac{77}{8} O_6^6] \,, \end{aligned} \tag{2.11}$$

where $r = \frac{R_2}{R_1}$=1.14, $\alpha_J = \frac{-1}{99}$, $\beta_J = \frac{2}{16335}$ and $\gamma_J = \frac{-1}{891891}$ are Stevens' multiplicative factors for $Tb_2Ti_2O_7$ , $\tilde{B}_n^m$ are crystal field parameters and $O_n^m$ are Stevens operators for J=6 given in Appendix B. Then, we seek to find all possible ground states of this Hamiltonian. Crystal field parameters $\tilde{B}_n^m$ are unknown parameters that have to be determined. However, we can choose them as free parameters and by varying them we can find all the possible ground states of $Tb_2Ti_2O_7$. To accomplish this, we define a new set of coefficients in terms of the unknown parameters in Eq. (2.11) as follows

$$\alpha_J \tilde{B}_2^0 F(2) = Wx \,, \tag{2.12a}$$

$$\beta_J \tilde{B}_4^0 F(4) = Wy(1-|x|) \,, \tag{2.12b}$$

$$\gamma_J \tilde{B}_6^0 F(6) = W(1-|y|)(1-|x|) \,, \tag{2.12c}$$

where, $F(2)$=3, $F(4)$=60, $F(6)$=7560 [59,60], $x$, $y$ are real numbers between -1 and 1 and $W$ is an overall energy scale factor. Writing the crystal field Hamiltonian in terms of these three parameters ($r = 1.14$) and varying them, we calculate all the possible crystal field ground states. We find that the ground state of this crystal field Hamiltonian is either a magnetic doublet or a singlet. However, to find the proper $x$, $y$ and $W$ and thus, the ground state of $Tb_2Ti_2O_7$ we need some input

from experiments. Here, we use inelastic neutron scattering data which shows that the ground state and first excited state of $Tb_2Ti_2O_7$ are doublets separated from each other by an 18 K gap [43]. Fitting these experimental results to the calculated ground state and first excited state gives values -0.79, 0.68 and -13.85 K for $x$, $y$ and $W$, respectively. To investigate the effect of any change in the ratio of the positions of oxygens $r = \frac{R_2}{R_1}$ on the crystal field levels, we find the behaviour of the crystal field levels as a function of $r$ for the given values $x$, $y$ and $W$ for $Tb_2Ti_2O_7$. In Fig. 2.3, we depict the variation of the three lowest crystal field states as a function of $r$.

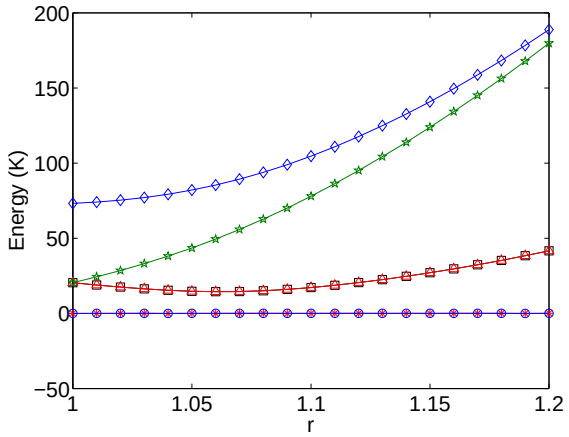


Figure 2.3: The evaluation of the crystal field states of $Tb_2Ti_2O_7$ as a function of $r = \frac{R_2}{R_1}$ (Fig. 2.2). The ground state and the first excited state are doublets while the second and the third excited states are singlets.

For $r$=1 (cubic environment) the ground state of $Tb_2Ti_2O_7$ is a non-magnetic doublet and the first excited state is a triplet. In the cubic environment, eight environmental oxygens form four symmetric directions in each equator of the cube. If the $Tb^{3+}$ ion possessed a magnetic doublet in this environment it would have to choose one of these axis as the preferred axes for its magnetic moment which is not symmetrically possible. Hence the ground state of $Tb^{3+}$ in a cubic environment is a non-magnetic doublet. For $r > 1$ the ground state and the first excited state are both magnetic doublets and the gap between them changes as a function of $r$ and reaches a minimum at $r$=1.106. The magnetic ground state doublet originates

from the fact that the two states of the crystal ground state are time-reversed and, because of the symmetry of the Hamiltonian (Hamiltonian is made of $O_n^{3m}$ operators), all eigenstates have the $|\phi\rangle = \sum_n \alpha_n |m \pm 3n\rangle$ ($|m \pm 3n| < 6$) structure, where $|m\rangle$ is an eigenstate of $J^z$. Hence the only non-magnetic doublet ($\langle\phi|J^z|\phi\rangle = 0$) is the one that possess the highest $J^z$ component, namely $m$=6. For the $Tb^{3+}$ ion in $Tb_2Ti_2O_7$ , $m = \pm 4$ and, based on the above argument, two states of the ground state have to be the magnetic doublet ($\langle\phi|J^z|\phi\rangle \neq 0$).

Until now we used the point charge approximation to calculate the crystal field levels and states of $Tb_2Ti_2O_7$. These crystal field levels give a semi-quantitative description of the experimental crystal field levels. However, because of the approximations made in deriving the crystal field Hamiltonian these levels are not quantitatively good enough to describe the crystal field levels and states of $Tb_2Ti_2O_7$. Hence, from a first principle approach, one would need to use more sophisticated methods to go beyond the simple point charge approximation to calculate the crystal field Hamiltonian of $Tb_2Ti_2O_7$. One of these methods is to use the known crystal field parameters of a compound with similar structure to derive the crystal field parameters of $Tb_2Ti_2O_7$ as we now explain. The crystal field parameters of $Ho_2Ti_2O_7$, with the same structure of $Tb_2Ti_2O_7$, were determined by fitting the crystal field eigenvalues to the energy levels obtained by the experimental inelastic neutron scattering. We use these $Ho_2Ti_2O_7$ crystal field parameters to determine the crystal field Hamiltonian of $Tb_2Ti_2O_7$.

Based on symmetry considerations for the distorted cubic environment, the most general form of the crystal field Hamiltonian of $Tb^{3+}$ in $Tb_2Ti_2O_7$ reads [33],

$$H_{\rm cf} = B_2^0 O_2^0 + B_4^0 O_4^0 + B_4^3 O_4^3 + B_6^0 O_6^0 + B_6^3 O_6^3 + B_6^6 O_6^6 \,, \tag{2.13}$$

where $O_n^m$ are Stevens operators for $Tb_2Ti_2O_7$ given in Appendix B and $B_n^m$ are crystal field parameters that have to be determined.

From Eq. (2.8) we conclude that the crystal field parameters $B_n^m$ are proportional to $\langle r^n \rangle$ and hence for two similar compounds with different rare earth elements the crystal field parameters of one rare earth ion are related to those of the other ion by this scaling factor. We use this scaling of the crystal field parameters to scale the crystal field parameters of $Ho_2Ti_2O_7$ by $\langle r^k \rangle_{(Tb^{+3})} / \langle r^k \rangle_{(Ho^{+3})}$, where $k$

| | $\tilde{B}_2^0$ (K) | $\tilde{B}_4^0$ (K) | $\tilde{B}_4^3$ (K) | $\tilde{B}_6^0$ (K) | $\tilde{B}_6^3$ (K) | $\tilde{B}_6^6$ (K) |
|---|---|---|---|---|---|---|
| $Ho_2Ti_2O_7$ | 68.2 | 274.8 | 83.7 | 86.8 | -62.5 | 101.6 |
| $Tb_2Ti_2O_7$ | 75.3 | 329.0 | 100.2 | 110.6 | -79.6 | 129.42 |

Table 2.2: Crystal field parameters of $Ho_2Ti_2O_7$ and the derived crystal field parameters of $Tb_2Ti_2O_7$. The scaling parameters are $\langle r^2\rangle_{(Tb^{+3})}/\langle r^2\rangle_{(Ho^{+3})}$=1.104, $\langle r^4\rangle_{(Tb^{+3})}/\langle r^4\rangle_{(Ho^{+3})}$=1.197, $\langle r^6\rangle_{(Tb^{+3})}/\langle r^6\rangle_{(Ho^{+3})}$=1.274 [62]. The $\tilde{B}_n^m$ are in Kelvin.

| $M_2^0$ | $M_4^0$ | $M_4^3$ | $M_6^0$ | $M_6^3$ | $M_6^6$ |
|---|---|---|---|---|---|
| $\frac{\alpha_J}{2}$ | $\frac{\beta_J}{8}$ | $-\frac{\sqrt{35}\beta_J}{2}$ | $\frac{\gamma_J}{16}$ | $\frac{\sqrt{105}\gamma_J}{8}$ | $\frac{\sqrt{231}\gamma_J}{16}$ |

Table 2.3: Scaling factors from $\tilde{B}_n^m$ to $B_n^m$; $B_n^m = M_n^m \tilde{B}_n^m$. $\alpha_J = -\frac{1}{99}$, $\beta_J = \frac{2}{16302}$, $\gamma_J = -\frac{1}{891891}$ [63]

is the order of the crystal field parameter, to derive the crystal field parameters of $Tb_2Ti_2O_7$ [35, 62].

The crystal field parameters of $Ho_2Ti_2O_7$ (Table 2.2) were determined by fitting the calculated crystal field states to the crystal field levels determined from inelastic neutron scattering [35]. However, in Reference [35] Rozenkranz *et. al.* used the tensorial operator notation to fit their data. The transformation between the parameters in this notation and Stevens parameters $M_n^m$ are given in Table 2.3 and to avoid any inconsistency we show the Rozenkranz *et. al.* [35] crystal field parameters by $\tilde{B}_n^m$ and our crystal field parameters in Eq. 2.13 by $B_n^m$.

In Table 2.4, we show the eigenstates and eigenvalues of the crystal field Hamiltonian. Some important points about these crystal field levels are:

- The ground state of the Hamiltonian is a magnetic doublet with largest contribution from $|\pm 4\rangle$ and small contributions from $|\mp 5\rangle$, $|\mp 2\rangle$ and $|\pm 1\rangle$. Because of the time reversal symmetry, two states of the doublet are time conjugate and the expectation value of **J** components between these states is zero (**J** is Hermitian and odd under the time-reversal symmetry, hence its expectation value between two time-reversal states is zero).

| E (K) | | $\|-6\rangle$ | $\|-5\rangle$ | $\|-4\rangle$ | $\|-3\rangle$ | $\|-2\rangle$ | $\|-1\rangle$ | $\|0\rangle$ | $\|1\rangle$ | $\|2\rangle$ | $\|3\rangle$ | $\|4\rangle$ | $\|5\rangle$ | $\|6\rangle$ |
|---|---|---|---|---|---|---|---|---|---|---|---|---|---|---|
| 0 | D | 0 | 0.29 | 0 | 0 | -0.14 | 0 | 0 | 0.1 | 0 | 0 | -0.94 | 0 | 0 |
| 18.7 | D | 0 | 0.93 | 0 | 0 | 0.19 | 0 | 0 | 0.08 | 0 | 0 | 0.31 | 0 | 0 |
| 142.1 | S | 0.25 | 0 | 0 | 0.66 | 0 | 0 | 0 | 0 | 0 | -0.66 | 0 | 0 | 0.25 |
| 212.4 | S | 0.33 | 0 | 0 | 0.62 | 0 | 0 | 0.12 | 0 | 0 | -0.62 | 0 | 0 | 0.33 |
| 484.1 | S | 0.66 | 0 | 0 | -0.25 | 0 | 0 | 0 | 0 | 0 | 0.25 | 0 | 0 | 0.66 |
| 497.7 | S | 0.63 | 0 | 0 | -0.32 | 0 | 0 | -0.04 | 0 | 0 | 0.32 | 0 | 0 | 0.63 |
| 577.0 | D | 0 | 0.23 | 0 | 0 | -0.97 | 0 | 0 | -0.07 | 0 | 0 | 0.06 | 0 | 0 |
| 817.8 | D | 0 | 0.03 | 0 | 0 | 0.07 | 0 | 0 | -0.99 | 0 | 0 | 0.12 | 0 | 0 |
| 912.0 | S | 0.02 | 0 | 0 | 0.09 | 0 | 0 | -0.99 | 0 | 0 | -0.09 | 0 | 0 | 0.02 |

Table 2.4: Crystal field eigenvalues and eigenstates of $Tb_2Ti_2O_7$. The first column shows the energy of the state and the second column shows the degeneracy of that state that can be either singlet (S) or doublet (D). The corresponding eigenstate of each eigenvalue is given in front of the eigenvalues and in the $J^z$ basis. In the case of a doublet one of the states is given and the other state is the time conjugate of that state.

- The first excited state is a doublet separated from the ground state by an 18.7 K gap and is connected to the ground state by $J^x$, $J^y$ and $J^z$ matrix elements. The rest of the crystal field excited states are separated by a large gap, more than $\sim$100 K, from the ground state.
- Neglecting all the **J** matrix elements between the ground state and excited states, the two states of the ground state can be considered as Ising spins pointing either towards or away from the center of gravity of each tetrahedron (local $\langle 111 \rangle$ axis). This Ising-like behavior in the manifold of the ground state is the basic assumption of spin ice systems and that is why most of the previous works assumed $Tb_2Ti_2O_7$ as to be a $\langle 111 \rangle$ Ising spin system on a pyrochlore lattice [27, 32, 33].

## 2.3 Summary

In this Chapter we studied the crystal field effect in f-electron ions in a crystalline environment. Based on the symmetry of the environment, we derived a crystal field Hamiltonian in terms of Stevens operators that are functions of total angular momentum $J$. In this framework we introduced the point charge approximation where

all the environmental ions are treated as point charges and the interaction between the rare earth f electrons and environment is the electrostatic interaction. We calculated the crystal field Hamiltonian of $Tb_2Ti_2O_7$ in the point charge approximation and showed that the ground state and the first excited states are doublets. Going beyond the point charge approximation, we used a semi-empirical method to determine the crystal field parameters of $Tb_2Ti_2O_7$ by rescaling the crystal field parameters of $Ho_2Ti_2O_7$ independently found from inelastic neutron scattering. Using these crystal field parameters, we calculated the crystal field Hamiltonian, its eigenstates and its eigenvalues, which were consistent with the experimental results. These crystal field states are semi-quantitatively similar to crystal field states of Ref. [33] and the small difference in the coefficients of the crystal field eigenstates and energy levels is related to the different methods with which the crystal field parameters were obtained.

# Chapter 3

# Effective Hamiltonian Method

In this chapter, we give a review of the effective Hamiltonian method and use this method in the next chapter as well as in Appendix A to derive an effective Hamiltonian for $Tb_2Ti_2O_2$, $Dy_2Ti_2O_7$ and $Ho_2Ti_2O_2$.

Except for a few well known problems in quantum mechanics, it is impossible to calculate the exact eigenvalues and eigenstates of a physical quantum system. Therefore, many perturbative methods have been invented to obtain an approximation of the exact eigenvalues and eigenstates of a physical quantum system. One of these perturbative methods which is useful in studying the low-energy physics of a problem is the so-called effective Hamiltonian method [64]. This method is mostly useful for systems whose Hamiltonian can be approximated by another Hamiltonian which has a degenerate ground state. This is because this method gives a systematic procedure as to what combination of degenerate states perturbation to choose as its eigenstates.

Since our aim in this chapter is to give a systematic method for deriving the effective Hamiltonian, we start the first section with a review on the Brillouin-Wigner perturbation theory and derive a perturbative expansion for the eigenvalues and eigenfunctions of a given Hamiltonian [64]. We show that in this expansion, the derived eigenvalues and eigenfunctions depend on the exact eigenvalues of the system, which is a disadvantage. Following the same prescription as in the Brillouin-Wigner perturbation theory we introduce the Rayleigh-Schrödinger perturbation theory.

This perturbation method is used in the second section to derive a perturbative expansion for the eigenstates and the eigenvalues of a Hamiltonian in terms of the eigenvalues and eigenstates of its model Hamiltonian. In the third section, we use the Rayleigh-Schrödinger perturbation theory to determine the effective Hamiltonian of a system in its low-energy sector. Moreover, we introduce a systematic method to calculate the eigenstates of the original Hamiltonian in the low-energy sector in terms of the eigenstates and eigenvalues of the effective Hamiltonian. We mention here that this chapter is mostly adopted from Chapter 9 of Reference [64].

## 3.1 Brillouin-Wigner Perturbation Theory

In this section we derive a perturbative expansion for the eigenvalues and eigenstates of a Hamiltonian in terms of eigenstates and eigenvalues of a known Hamiltonian. To start, we assume that $H$ is the total Hamiltonian of the system and this Hamiltonian can be written in terms of a model Hamiltonian $H_0$ and a perturbation $V$ as follow:

$$H = H_0 + V. \tag{3.1}$$

The model Hamiltonian is chosen such that it is exactly solvable and a good starting approximation for the total Hamiltonian. For simplicity, we assume in this section, that the eigenstates of the model Hamiltonian are non-degenerate. This does not affect the generality of the discussion and eases the formalism. Now, assume that $|\phi^\alpha\rangle$ are the eigenstates of the model Hamiltonian. These eigenstates make a complete and orthonormal set of states such that,

$$H_0|\phi^\alpha\rangle = E_0^\alpha|\phi^\alpha\rangle, \tag{3.2a}$$

$$\langle\phi^\alpha|\phi^\beta\rangle = \delta^{\alpha\beta} \tag{3.2b}$$

where $\delta^{\alpha\beta}$ is the Kronecker delta. Often, the physical properties of a system at low-temperatures can be suitably described by a restricted low energy sector of the eigenvalues and eigenstates of the total Hamiltonian. This sector of the eigenvalues and eigenstates can be approximated to zero-order by the eigenstates and eigenvalues of $H_0$. If we denote this sector of the Hilbert space by $|\Psi_0\rangle = |\phi^\alpha\rangle$ and define a

projector operator to this subspace with $P$, and to the complementary part of the Hilbert space with $Q$, we have,

$$P = \sum_{\alpha} |\phi^{\alpha}\rangle\langle\phi^{\alpha}| \ , \tag{3.3a}$$

$$Q = \sum_{\beta\neq\alpha} |\phi^{\beta}\rangle\langle\phi^{\beta}|. \tag{3.3b}$$

Using the completeness and orthonormality of the eigenstates of $H_0$, we have

$$P + Q = 1. \tag{3.4}$$

Some of the useful properties of $P$ and $Q$ operators are

$$\begin{aligned} P^{\dagger} &= P; Q^{\dagger} = Q \ , \\ P^2 &= P; Q^2 = Q \ , \\ [p, Q] &= 0 \ , \\ [P, H_0] &= [Q, H_0] = 0 \ . \end{aligned} \tag{3.5}$$

Consider $|\Psi\rangle$ as the exact eigenstate of the total Hamiltonian $H$. The effect of operator $P$ on this state is,

$$P|\Psi\rangle = |\Psi_0\rangle\langle\Psi_0|\Psi\rangle \ . \tag{3.6}$$

Setting the scalar product $\langle\Psi_0|\Psi\rangle$ to 1, and assuming that $|\Psi_0\rangle$ is normalized to 1, we get,

$$P|\Psi\rangle = |\Psi_0\rangle \ . \tag{3.7}$$

This equation can be written down in terms of $|\Psi_0\rangle$ and operator Q as follows

$$|\Psi\rangle = (P + Q)|\Psi\rangle = |\Psi_0\rangle + Q|\Psi\rangle \ . \tag{3.8}$$

Here, the goal is to find a perturbative (recursive) method to calculate $Q|\Psi\rangle$ in terms of $|\Psi_0\rangle$. To accomplish this, we write down the Schrödinger equation ($H|\Psi\rangle = E|\Psi\rangle$) as follows:

$$(E - H_0)|\Psi\rangle = V|\Psi\rangle \ . \tag{3.9}$$

Applying $Q$ to the left hand side we get,

$$(E - H_0)Q|\Psi\rangle = QV|\Psi\rangle \ . \tag{3.10}$$

To solve this equation, we introduce a resolvent $T_E$ that satisfies the following relations,

$$T_E(E - H_0) = Q \ , \tag{3.11a}$$

$$T_E Q = Q T_E = T_E \ . \tag{3.11b}$$

Applying $T_E$ to the eigenstates of the model Hamiltonian gives,

$$T_E(E - H_0)|\phi^\beta\rangle = Q|\phi^\beta\rangle, \tag{3.12a}$$

$$T_E|\phi^\beta\rangle = \frac{Q}{E - E_0^\beta}|\phi^\beta\rangle. \tag{3.12b}$$

Hence, $T_E$ and $H_0$ have the same eigenstates and eigenvalues. Also, Applying $T_E$ to the model space and using Eq. (3.11b), gives zero ($T_E|\phi^\alpha\rangle = 0, \alpha \neq \beta$). Expanding the resolvent in terms of the eigenvalues and eigenstates of $H_0$ gives

$$T_E = \sum_{\beta \neq \alpha} \frac{|\phi^\beta\rangle\langle\phi^\beta|}{E - E_0^\beta}. \tag{3.13}$$

Multiplying $T_E$ to the left-hand side of Eq. (3.10) gives,

$$Q|\Psi\rangle = T_E V|\Psi\rangle. \tag{3.14}$$

Using $P + Q = 1$, we get,

$$|\Psi\rangle = |\Psi_0\rangle + T_E V|\Psi\rangle. \tag{3.15}$$

Now, we seek a perturbative solution to Eq. (3.15). Applying a recursive method and using Eq. (3.11a), we find a perturbative solution for this equation as follows,

$$|\Psi\rangle = (1 + \frac{Q}{E - H_0}V + \frac{Q}{E - H_0}V\frac{Q}{E - H_0}V + ...)|\Psi_0\rangle. \tag{3.16}$$

This is the Brillouin-Winger expansion for the exact wavefunction. As we mentioned in the beginning of this section, $V$ is a small perturbation to the model Hamiltonian

$H_0$ and hence Eq. (3.16) is convergent. From Eq. (3.16) it is possible to find a so-called wave operator so that,

$$|\Psi\rangle = \Omega_E |\Psi_0\rangle, \tag{3.17}$$

where from Eq. (3.15), $\Omega_E$ satisfies the equation

$$\Omega_E = 1 + T_E V \Omega_E. \tag{3.18}$$

This wave operator depends explicitly on the eigenvalues $E$ of the full Hamiltonian $H$ which are not known. Therefore, it is useful to seek another perturbative method in terms of the known eigenvalues and eigenstates of the model Hamiltonian. This method, which we discuss in the next section, is the well-known Rayleigh-Schrödinger perturbation theory.

## 3.2 Rayleigh-Schr$'$odinger Perturbation Theory

In this section, we seek a perturbation expansion in terms of the eigenvalues and eigenstates of the model Hamiltonian ($H_0$). From the previous section, the operator $P$ is defined such that it projects the exact eigenstates to the model space and, the operator $\Omega$ maps the model space to the exact eigenstates. We should mention that in this section we denote operator $\Omega_E$ by $\Omega$ because at the end we derive this operator in terms of the eigenvalues of $H_0$ ($E_0$). In mathematical notation these operators are defined through,

$$|\Psi_0^a\rangle = P|\Psi^a\rangle \ (a = 1, 2, ..., m) \ , \tag{3.19a}$$

$$|\Psi^a\rangle = \Omega|\Psi_0^a\rangle \ (a = 1, 2, ..., m) \ , \tag{3.19b}$$

where $m$ is the dimension of the degenerate ground state. Mapping the exact eigenstates onto the model space gives some states that are in general non-orthonormal (mapping of two orthogonal vectors to a hypersurface gives two vectors that are not in general orthogonal). However, it is usually possible to use the Graham-Schmidt method and find some orthonormal states ($|\Psi_0^{'b}\rangle$) out of these states ($|\Psi_0^b\rangle$) that satisfy biorthonormality condition,

$$\langle \Psi_0^{'b} | \Psi_0^a \rangle = \delta^{ab} \tag{3.20}$$

The projection operator onto the model space in terms of these new states ($|\Psi_0'^b\rangle$) is

$$P = \sum_{b=1}^{m} |\Psi_0^b\rangle\langle\Psi_0'^b|. \tag{3.21}$$

Using the fact that $|\Psi_0^a\rangle = \mathrm{P}\Omega|\Psi_0^a\rangle$, we have the following identity between operators $P$ and $\Omega$,

$$P\Omega P = P. \tag{3.22}$$

To zeroth order in perturbation theory, the operator $\Omega$ is 1 (Eq. (3.18)), hence it is useful to define another operator $\chi$ such that it gives the perturbative part of the expansion as:

$$\chi = \Omega - 1. \tag{3.23}$$

The operator $\chi$ contains the information about the perturbative part of the interaction. Applying this operator to the model space gives the projection of the full wave function to the complementary space as,

$$\chi|\Psi_0^a\rangle = (\Omega - 1)|\Psi_0^a\rangle. \tag{3.24}$$

$|\Psi^a\rangle - |\Psi_0^a\rangle$ gives the component of each exact state to the excited states, therefore the effect of the operator $\Omega - 1$ is similar operator $Q$ in Eq. (3.3b) and we have

$$(\Omega - 1)|\Psi_0^a\rangle = Q|\Psi^a\rangle. \tag{3.25}$$

Two useful identities for this operator are,

$$P\chi P = 0, \tag{3.26a}$$

$$Q\Omega P = \chi P. \tag{3.26b}$$

Eq. (3.26b) can be proved by writing Eq. (3.25) as $\chi|\Psi_0^a\rangle = Q\Omega|\Psi_0^a\rangle$. To derive a recursion relation in terms of the eigenvalues of the model Hamiltonian for $\chi$ we start with the Schrödinger equation

$$H|\Psi^a\rangle = E^a|\Psi^a\rangle. \tag{3.27}$$

This equation can be written as

$$(E^a - H_0)|\Psi_0^a\rangle = PV|\Psi^a\rangle. \tag{3.28}$$

Applying $\Omega$ to the left hand side gives,

$$E^a|\Psi^a\rangle - \Omega H_0|\Psi_0^a\rangle = \Omega PV\Omega|\Psi_0^a\rangle. \tag{3.29}$$

Subtracting this equation from the Schrödinger equation gives,

$$[\Omega, H_0]P = V\Omega P - \Omega PV\Omega P. \tag{3.30}$$

This equation can be reorganized in terms of operator $\chi$ by writing $\Omega PV\Omega P = (1-\chi)PV\Omega P$ and using the identity $Q = 1 - P$ as follow,

$$[\Omega, H_0]P = QV\Omega P - \chi PV\Omega P. \tag{3.31}$$

Using a recursive method, we can find a perturbative solution for $\chi$ in terms of the perturbation potential $V$. Hence we seek an expansion for $\chi$ and $\Omega$ as follows,

$$\chi = \Omega^{(1)} + \Omega^{(2)} + ..., \tag{3.32a}$$
$$\Omega = 1 + \Omega^{(1)} + \Omega^{(2)} + .... \tag{3.32b}$$

Substituting these equations into Eq. (3.30), and keeping terms of the same order in $V$, we have

$$\begin{aligned} [\Omega^{(1)}, H_0]P &= QVP, \\ [\Omega^{(2)}, H_0]P &= QV\Omega^{(1)}P - \Omega^{(1)}PVP, \\ [\Omega^{(3)}, H_0]P &= QV\Omega^{(2)}P - \Omega^{(2)}PVP - \Omega^{(1)}PV\Omega^{(1)}P. \end{aligned} \tag{3.33}$$

The generalized form of these commutators for $\Omega^{(n)}$ in terms of the lower perturbation terms is

$$[\Omega^{(n)}, H_0]P = QV\Omega^{(n-1)}P - \sum_{m=1}^{n-1} \Omega^{(n-m)}PV\Omega^{(m-1)}P. \tag{3.34}$$

The recursive form of this equation in terms of $\chi^{(n)}$ is

$$[\Omega^{(n+1)}, H_0]P = QV\Omega^{(n)}P - \chi^{(n)}PV\Omega^{(n)}P, \tag{3.35a}$$
$$\chi^{(n)} = 1 - \Omega^{(n)}. \tag{3.35b}$$

We can find a matrix form of this equation by evaluating Eq. (3.33) between states $|\alpha\rangle$ and $|\beta\rangle$ and using the eigenstates of the model Hamiltonian as follow

$$\langle\beta|\Omega^{(1)}|\alpha\rangle = \frac{\langle\beta|V|\alpha\rangle}{E_0^\alpha - E_0^\beta}, \tag{3.36a}$$

$$\langle\beta|\Omega^{(2)}|\alpha\rangle = \sum_\gamma \frac{\langle\beta|V|\gamma\rangle\langle\gamma|V|\alpha\rangle}{(E_0^\alpha - E_0^\beta)(E_0^\alpha - E_0^\gamma)} - \sum_{\alpha'} \frac{\langle\beta|V|\alpha'\rangle\langle\alpha'|V|\alpha\rangle}{(E_0^\alpha - E_0^\beta)(E_0^{\alpha'} - E_0^\beta)}, \tag{3.36b}$$

where $|\alpha\rangle$ and $|\alpha'\rangle$ belong to the model space and $|\beta\rangle$ and $|\gamma\rangle$ belong to the $Q$ space.

In the next section we apply the results of this section to derive an effective Hamiltonian in a degenerate model space.

## 3.3 Effective Hamiltonian

In the previous section we derived the Rayleigh-Shrödinger perturbation theory for a degenerate model space. However, before applying the Rayleigh-Shrödinger perturbation theory we need to know what linear combination of degenerate states is selected by the perturbation Hamiltonian. In this section we introduce an effective Hamiltonian method which not only finds systematically the linear combination of degenerate states, but also sometimes gives a deeper physical insight into the problem (if the effective Hamiltonian is similar to another well-known Hamiltonian).

To derive the effective Hamiltonian for the degenerate model space we apply operator $P$ to the Schrödinger equation, (Eq. (3.27)) and also use Eq. (3.17) to derive the following equation,

$$PH\Omega|\Psi_0^a\rangle = E^a|\Psi_0^a\rangle. \tag{3.37}$$

Hence $|\Psi_0^a\rangle$ is the eigenstate of operator $PH\Omega$ with eigenenergy $E^a$. We use the fact that $P|\Psi^a\rangle$=$|\Psi_0^a\rangle$ to write down Eq. (3.37) in terms of operators as follows

$$H_{\text{eff}} = PH\Omega P. \tag{3.38}$$

This operator $H_{\text{eff}}$ is called the effective Hamiltonian and from Eq. (3.37) we find that the eigenenergies of this operator are the eigenenergies of the total Hamiltonian $H$ (Eq. (3.27)) in the model space sector. In addition, from Eq. (3.19a) and the eigenstates of $H_{\text{eff}}$ (Eq. (3.38)), we conclude that its eigenstates of this operator is the projection of the exact eigenstates onto the model space $P$. To separate the perturbative part of the interaction from the non-perturbative part we write down the effective Hamiltonian in terms of the operator $\chi$ as follow,

$$H_{\text{eff}} = PHP + PV\chi P. \tag{3.39}$$

Assuming that all the states of the model space are degenerate, the effective Hamiltonian could be calculated in terms of the operator $P$, the perturbative potential $V$, and the resolvent $R$. To accomplish this, we use the relation $(\Omega H_0 - H_0\Omega)P = (E_0 - H_0)\Omega P$ and write down the left hand side of Eq. (3.30) as

$$[\Omega, H_0] = (E_0 - H_0)\Omega P. \tag{3.40}$$

Using Eq. (3.29) this equation can be written as,

$$(E_0 - H_0)\Omega P = QV\Omega P - \chi PV\Omega P. \tag{3.41}$$

We define the resolvent $R$ for this equation similarly to the resolvent $T_E$ in Eqs. (3.11a) and (3.11b) as follow,

$$R(E_0 - H_0) = Q, \tag{3.42a}$$

$$RQ = R. \tag{3.42b}$$

We apply operator $R$, to both sides of Eq. (3.41) and use the expansion of $\Omega$ and $\chi$ in terms of $\Omega^{(n)}$ in Eqs. (3.32a) and (3.32b) to derive a recursive solution in terms of $\Omega^{(n)}$. The result of this calculation to third order reads

$$\Omega^{(1)}P = RVP, \tag{3.43a}$$

$$\Omega^{(2)}P = R(V\Omega^{(1)}P - \Omega^{(1)}PVP), \tag{3.43b}$$

$$\Omega^{(3)}P = R(V\Omega^{(2)}P - \Omega^{(2)}PVP - \Omega^{(1)}PV\Omega^{(1)}P). \tag{3.43c}$$

For $n > 1$ the right hand side of each equation is a function of lower order terms in $\Omega^{(n)}$, hence by substituting the lower order terms of $\Omega^{(n)}$ into the higher order

terms, we can recursively calculate each term as a function of operators $P$, $R$ and $V$. Substituting this perturbative solution in Eq. (3.37), we find a perturbative solution in terms of operators $P$, $R$ and $V$ for the effective Hamiltonian. The result of this calculation to third order reads

$$H_{\text{eff}}^{(0)} = PH_0P, \tag{3.44a}$$
$$H_{\text{eff}}^{(1)} = PVP, \tag{3.44b}$$
$$H_{\text{eff}}^{(2)} = PVRVP, \tag{3.44c}$$
$$H_{\text{eff}}^{(3)} = PVRVRVP - PVR^2VPVP. \tag{3.44d}$$

This perturbative solution for the effective Hamiltonian is complete if we find a solution for resolvent $R$ in terms of the eigenvalues and eigenstates of the model Hamiltonian. Using Eq. (3.42a), we find a spectral decomposition of $R$ as follows:

$$R = \sum_{\beta \notin P} \frac{|\beta\rangle\langle\beta|}{E_0 - E_0^{\beta}}. \tag{3.45}$$

where $\beta \notin P$ confirms that state $|\beta\rangle$ does not belong to the model space. Substituting $R$ into Eqs. (3.44a), (3.44b), (3.44c) and (3.44d) of the effective Hamiltonian, we obtain a perturbative expansion for the effective Hamiltonian in terms of the eigenvalues and eigenstates of the model Hamiltonian.

By diagonalizing this effective Hamiltonian to the desirable order we can find the eigenvalues of the system to that order in the model space. However, the eigenvalues of the system are not the only quantities we need to calculate. In fact, we generally need to calculate other physical quantities. To accomplish this, we need to know the eigenstates of the exact Hamiltonian in the low-energy sector. The eigenstates of the exact Hamiltonian can be obtained by applying the wave operator to the model space term by term. Substituting Eqs. (3.43a) and (3.43b) into Eq. (3.19b), the eigenstates of the exact Hamiltonian in terms of the eigenvalues and eigenstates

of the model Hamiltonian to second order are,

$$|\Psi^{(1)}\rangle = \Omega^{(1)}|\Psi_0^a\rangle = \sum_\beta \frac{|\beta\rangle\langle\beta|V|\Psi_0^a\rangle}{E_0 - E_0^\beta} \tag{3.46a}$$

$$|\Psi^{(2)}\rangle = \Omega^{(2)}|\Psi_0^a\rangle = \sum_{\beta\gamma} \frac{|\beta\rangle\langle\beta|V|\gamma\rangle\langle\gamma|V|\Psi_0^a\rangle}{(E_0 - E_0^\beta)(E_0 - E_0^\gamma)} - \sum_{\beta\gamma} \frac{|\beta\rangle\langle\beta|V|\gamma\rangle\langle|\gamma|V|\Psi_0^a\rangle}{(E_0 - E_0^\beta)^2}, \tag{3.46b}$$

where $|\beta\rangle$ and $|\gamma\rangle$ belong to the $Q$ space.

Having derived the eigenstates of the exact Hamiltonian in the model space, our discussion is complete and we can now apply this method to any physical system and calculate the low energy physics of the problem. In the next chapter we apply this effective Hamiltonian method to $Tb_2Ti_2O_7$ to derive an effective Hamiltonian in the low-energy sector of the crystal field ground state doublet.

# Chapter 4

# Effective Hamiltonian of $Tb_2Ti_2O_7$

Armed with the Rayleigh-Schrödinger perturbation theory described in the previous chapter, we apply it in this chapter to $Tb_2Ti_2O_7$ in order to derive an effective Hamiltonian in the crystal field ground state doublet basis. The reason for using the effective Hamiltonian method is to first reduce the amount of computational resources (by reducing the Hilbert state from all $(2J + 1{=}13)$ crystal field states per ion to two states per ion) and second to help unravel the basic physics of the problem. We also use this effective Hamiltonian method in the next chapters to investigate some of the physical properties of $Tb_2Ti_2O_7$ at low temperatures. This chapter is organized in the following sections. In the first section, we introduce the total Hamiltonian for $Tb_2Ti_2O_7$, which is sum of the single ion crystal field Hamiltonian plus the dipole-dipole and exchange Hamiltonians. We choose the crystal field Hamiltonian and the interacting Hamiltonian as, respectively, the model Hamiltonian and the perturbative Hamiltonian, and also choose the crystal field ground state doublet as the model space. In the second section, we derive the effective Hamiltonian to first order of approximation and call it the classical term of the effective Hamiltonian. We show that the classical term of the effective Hamiltonian is made of local $\langle 111 \rangle$ Ising spins on a pyrochlore lattice interacting via exchange and dipole-dipole interactions. In the third section, we investigate the quantum corrections to second order in perturbation theory and, due to single ion excitations. We show that this quantum correction renormalizes the classical

term of the effective Hamiltonian. This renormalization is due to the single ion excitation of all $Tb^{3+}$ ions in the system and we name this term the *quantum Ising term*. We also investigate the effect of double crystal field excitations and show that these excitations generate matrix elements between the two states of the ground state doublet. This changes the symmetry of the magnetic moments of the effective Hamiltonian from the local $\langle 111 \rangle$ Ising spin system to the pseudo-spin 1/2 system with the local z direction pointing towards the $\langle 111 \rangle$ local axis.

## 4.1 Total Hamiltonian of $Tb_2Ti_2O_7$

As discussed in Chapter 3, we need to introduce the total Hamiltonian $H$, the model Hamiltonian $H_0$, the perturbative Hamiltonian $V$, the model space $P$, and the resolvent $R$ to calculate the effective Hamiltonian of a system. Hence, in this section, our aim is to introduce these operators for $Tb_2Ti_2O_7$. It is well established that the main interactions between $Tb^{3+}$ ions in $Tb_2Ti_2O_7$ are isotropic exchange interaction and the dipole-dipole interaction. Other interactions are small in comparison with these interactions (we will comment on this in Chapter 6 and put a limit on the anisotropic exchange and DM couplings) [33, 55, 56]. Based on this assumption, the total Hamiltonian of the system reads

$$\begin{aligned} H &= H_{\rm cf} + \mathcal{J} \sum_{\langle ij \rangle} \mathbf{J}_i \cdot \mathbf{J}_j \\ &+ \mathcal{D} r_{\rm nn}^3 \sum_{i>j} \frac{\mathbf{J}_i \cdot \mathbf{J}_j}{|\mathbf{r}_{ij}|^3} - \frac{3(\mathbf{J}_i \cdot \mathbf{r}_{ij})(\mathbf{J}_j \cdot \mathbf{r}_{ij})}{|\mathbf{r}_{ij}|^5} \,, \end{aligned} \tag{4.1}$$

where $H_{\rm cf}$ is the crystal field Hamiltonian for $Tb^{3+}$ ions in $Tb_2Ti_2O_7$ given in Eq. (2.13), $\mathcal{J}$ is the exchange coupling, $\mathcal{D}$ is the dipole-dipole coupling at first nearest neighbor, $\mathbf{J}_i$ is the J=6 total angular momentum operator for ion $i$, and $\mathbf{r}_{ij} = \mathbf{r}_j - \mathbf{r}_i$ is the vector position between ions $i$ and $j$. The estimated values of $\mathcal{J}$ and $\mathcal{D}$ for $Tb_2Ti_2O_7$ are respectively, 0.167 K and 0.0315 K (Section 1.3). With these values of the couplings, the interaction between $Tb^{3+}$ ions ($\sim$1 K) are much smaller than the crystal field gap between the ground state and excited states ($\Delta > 18.7$ K) and,

as a result, we can implement perturbation theory to deal with the interacting part of the Hamiltonian. In addition, crystal field states are good quantum states and we choose them as the basis for determining the matrix elements of the interacting part of the Hamiltonian. We should comment that by good quantum states we mean states that combine linearly under a perturbation and the structure of states does not change. Based on these assumptions, we split the Hamiltonian in two parts,

- The crystal field Hamiltonian, $H_{\rm cf}$, which is the model Hamiltonian, $H_0$.
- A perturbative Hamiltonian, $V$, which is the dipole-dipole plus isotropic exchange terms. We calculate the matrix elements of the perturbative Hamiltonian $V$ in the crystal field basis.

Hence, the model Hamiltonian, $H_0$, and the perturbative Hamiltonian, $V$, can be written as,

$$\begin{aligned} H_0 &= H_{\rm cf} && \text{(4.2a)} \\ V &= \mathcal{J}\sum_{\langle ij\rangle}\mathbf{J}_i\cdot\mathbf{J}_j \\ &+ \mathcal{D}r_{\rm nn}^3\sum_{i>j}\frac{\mathbf{J}_i\cdot\mathbf{J}_j}{|\mathbf{r}_{ij}|^3}-\frac{3(\mathbf{J}_i\cdot\mathbf{r}_{ij})(\mathbf{J}_j\cdot\mathbf{r}_{ij})}{|\mathbf{r}_{ij}|^5}\,. && \text{(4.2b)} \end{aligned}$$

With this decomposition of the model Hamiltonian, we define the basis states for our calculation as the tensor product of single ion crystal field states $|\Phi_{0,\{k\}}\rangle$, $|\Phi_{n,\{m\}}\rangle$, with energies $E^0$ and $E^n$,

$$|\Phi_{0,\{k\}}\rangle = \prod_{i=1}^{N}|\phi_{i,0}^{(k_i)}\rangle\,, \qquad \text{(4.3a)}$$

$$|\Phi_{\{n\},\{m\}}\rangle = \prod_{i=1;\sum n_i\neq 0}^{N}|\phi_{i,n_i}^{(m_i)}\rangle\,, \qquad \text{(4.3b)}$$

where $|\phi_{i,0}^{(k_i)}\rangle$ is the $k_i^{th}$ state of the crystal field ground state of $Tb^{3+}$ ion sitting at site $i$, $|\phi_{i,n_i}^{(k_i)}\rangle$ is the $k_i^{th}$ state of the $n_i$ level of crystal field state for ion at site $i$. The

multiplication is over all $Tb^{3+}$ ions $N$ in the crystal and $\sum n_i \neq 0$ imposes that at least one of the $Tb^{3+}$ ions in the system is in an excited crystal field state.

After defining all the necessary element of our calculation, we can now proceed to calculate the effective Hamiltonian by integrating out the fluctuations via the excited crystal field states and recast their effect as an effective interaction between the crystal field ground states of $Tb^{3+}$ ions. Since the ground state of the crystal field Hamiltonian is a doublet, we have to use the Rayleigh-Schrödinger expansion for a degenerate model space to calculate the effective Hamiltonian. From the previous chapter, the general expression for the effective Hamiltonian in terms of the projection operator, $P$, and the resolvent, $R$, to second order is,

$$H_{\text{eff}} = PVP + PVRVP\,, \tag{4.4a}$$

$$P = \sum_{\{k\}} |\Phi_{0,\{k\}}\rangle\langle\Phi_{0,\{k\}}|\,, \tag{4.4b}$$

$$R = \sum_{\{n\},\{m\}} \frac{|\Phi_{\{n\},\{m\}}\rangle\langle\Phi_{\{n\},\{m\}}|}{(E^0 - E^n)}. \tag{4.4c}$$

Where $V$ is given by Eq. (4.2b). The sum over $\{k\} = \{k_1, k_2, ..., k_N\}$ is over all the combinations of single ion crystal field ground states, sum over $\{n\}\{m\} = \{n_1, n_2, ..., n_n\}\{m_1, m_2, ..., m_N\}$ is over all the combinations of crystal field ground states and at least one $Tb^{3+}$ ion is in an excited crystal field state. $E^0$ and $E^n$ are defined as,

$$E^n = \sum_i E^{n_i}, \tag{4.5}$$

where $E^{n_i}$ is the energy of the $n^{th}$ crystal field excited states and sum is over all $Tb^{3+}$ ions in the crystal. Now we desire to determine the effective Hamiltonian to second order. To unravel quantum effects that may be at play, we break the effective Hamiltonian in two terms, the classical term, $PVP$ in Eq. (4.4a), which gives the effective Hamiltonian without any quantum excitations from the excited crystal field states, and the quantum correction, $PVRVP$ in (Eq. (4.4a)). We call $PVP$ the classical term because in this problem we can map this term to a strictly classical Ising model having local $\langle 111\rangle$ axis.

## 4.2 The Classical Term of the Effective Hamiltonian $PVP$

In this subsection, we calculate the classical part of the effective Hamiltonian. As we mentioned in the previous section, we name this part the classical Hamiltonian because the Hamiltonian calculated in the manifold of the crystal field ground state maps, as we show later, to a local $\langle 111\rangle$ Ising model. Substituting Eq. (4.4b) in $PVP$ we get,

$$H_{\text{eff}}^{(\text{classic})} = \sum_{\{k'\}\{k\}} |\Phi_{0,\{k'\}}\rangle\langle\Phi_{0,\{k'\}}|V|\sum|\Phi_{0,\{k\}}\rangle\langle\Phi_{0,\{k\}}|. \tag{4.6}$$

Substituting $V$ form Eq. (4.2b) and $|\Phi_{0,\{k\}}\rangle$ from Eq. (4.3a) in the above equation, we must recall that the operators $\mathbf{J}$ in the perturbative Hamiltonian $V$ are written in the global basis while the crystal field states $|\phi_{i,0}^{(k_i)}\rangle$ in the basis state $|\Phi_{0,\{k\}}\rangle$ are written in the local $\langle 111\rangle$ basis. Therefore, we need to use the rotational theorem to calculate the matrix elements of $\mathbf{J}$ operator in the crystal field basis. Transformation of the matrix elements of the angular momentum from the local easy axis to the global axis reads

$$\langle\phi_{i,0}^{(l_i)}|J_{i,a}^{\alpha}|\phi_{i,0}^{(m_i)}\rangle = u_{i,a}^{\alpha\beta}\langle\phi_{i,0}^{(l_i)}|\tilde{J}^{\beta}|\phi_{i,0}^{(m_i)}\rangle\ , \tag{4.7}$$

where $u_{i,a}^{\alpha\beta}$ is the $\alpha\beta$ component of the transformation matrix from the global axis to the local easy axis for sublattice $a$ given in Appendix C, $J_{i,a}^{\alpha}$ is the $\alpha$ component of the total angular momentum of $Tb^{3+}$ ion on sublattice $a$ in the global axis frame and $\tilde{J}^{\alpha}$ is the $\alpha$ component of the total angular momentum of $Tb^{3+}$ ion in the local axis frame. As we showed in Chapter 2, the only non-zero $\mathbf{J}$ matrix elements in the ground state doublet is the diagonal part of the $J^z$ matrix elements. Hence, two states of the crystal field ground state with the z direction towards the local $\langle 111\rangle$ axis can be described by a local $\langle 111\rangle$ Ising model. The classical part of the effective Hamiltonian then reads,

$$\begin{aligned} H_{\text{eff}}^{(\text{classic})} &= J\sum_{\langle ij,ab\rangle}\mathbf{S}_{i,a}^{z_a}\cdot\mathbf{S}_{j,b}^{z_b} \\ &+ Dr_{\text{nn}}^3\sum_{i,a>j,b}\frac{\mathbf{S}_{i,a}^{z_a}\cdot\mathbf{S}_{j,b}^{z_b}}{|\mathbf{r}_{ij,ab}|^3} - \frac{3(\mathbf{S}_{i,a}^{z_a}\cdot\mathbf{r}_{ij,ab})(\mathbf{S}_{j,b}^{z_b}\cdot\mathbf{r}_{ij,ab})}{|\mathbf{r}_{ij,ab}|^5}\ , \end{aligned} \tag{4.8}$$

where $J = \mathcal{J}|\langle J^z\rangle|^2$=1.57 K and $D = \mathcal{J}|\langle J^z\rangle|^2$=0.30 K are respectively exchange and dipole-dipole couplings between Ising spins (Section 1.3), $\mathbf{S}_{i,a}^{z_a}$ is the classical $\langle 111\rangle$ Ising vector at site $\{i, a\}$ where $i$ denotes the lattice point of the FCC lattice and $a$ denotes the sublattice. From now on we drop the sublattice indices from $z_a$ because it has been implied in $\mathbf{S}_{i,a}$ and we use this notation in the rest of this Chapter. The Hamiltonian in Eq. (4.8) is the Hamiltonian of a $\langle 111\rangle$ Ising model on a pyrochlore lattice and it is a model Hamiltonian for spin ice systems [32]. It is worthwhile to remind that this model, as we discussed in Section 1.2, has been extensively investigated by Monte Carlo simulations and the phase diagram as a function of temperature the ratio between the exchange coupling to the dipole-dipole coupling is discussed (Fig. 1.10) in Reference [32]. Depending upon this ratio, two phases arise at low temperatures. The all-in/all-out phase which is an ordered state and a spin-ice phase which is frustrated. It is shown that for low temperatures, there is a transition from the frustrated spin ice phase to a so-called Melko ordered phase [39]. Based on this phase diagram, and for the estimated exchange, and dipole-dipole couplings for $Tb_2Ti_2O_7$, $Tb_2Ti_2O_7$ is predicted to have a transition to the all-in/all-out ordered state at approximately 1.2K [32], inconsistent with the experimental results. In the next section, we consider the first correction due to the single ion crystal field excitations and explain how this correction renormalizes the classical phase boundary.

## 4.3 Quantum Term PVRVP

In this section, we calculate the first correction from the crystal field excited states to the classical term of the effective Hamiltonian, and address the incompleteness of the classical Hamiltonian in describing the behaviour of $Tb_2Ti_2O_7$. At this (second) order in perturbation theory, for each $Tb^{3+}$ ion, one virtual process between the crystal field ground state and the crystal field excited states occurs via the interaction Hamiltonian $V$. Hence, for a perturbative bi-particle Hamiltonian, the Hamiltonian in Eq. (4.2b), only single and double ion processes accrue. In the next two sections, we show how these processes create not only new terms with different symmetries than the classical term in the effective Hamiltonian, but also, and

perhaps most importantly, renormalize the interacting part of the classical term of the effective Hamiltonian $PVP$ and change the physical description of the system in the Ising sector of the low energy Hamiltonian.

To organize the calculations, we decompose the interaction Hamiltonian $V$ into its exchange and the dipole-dipole parts:

$$V = V_{\text{ex}} + V_{\text{dip}}, \tag{4.9}$$

where $V_{\text{ex}}$ is the exchange part of Hamiltonian $V$ and $V_{\text{dip}}$ is the dipole-dipole part of Hamiltonian $V$. Substituting $V \equiv V_{\text{ex}} + V_{\text{dip}}$ in $PVRVP$ gives,

$$\begin{aligned} H_{\text{eff}}^{(\text{Quantum})} &= PV_{\text{ex}}RV_{\text{ex}}P + (PV_{\text{ex}}RV_{\text{dip}}P + PV_{\text{dip}}RV_{\text{ex}}P) \\ &+ PV_{\text{dip}}RV_{\text{dip}}P\ , \end{aligned} \tag{4.10}$$

In this way, besides simplifying the calculations, we can figure out the effect of individual interactions in making up the effective Hamiltonian to order of $V^2$. In the next subsections, we study the single ion and double ion excitations arising from these individual terms, and derive the resulting effective Hamiltonian in terms of pseudo-spin 1/2 operators.

### 4.3.1 Single Ion Excitation

Following the discussion of the previous section, in this section we discuss the single ion excitation process and derive the contribution to the effective Hamiltonian generated by this process for a general bi-particle Hamiltonian. We then apply it to the individual terms of Eq. (4.10) to calculate the consequential effective Hamiltonian by the single ion process for $Tb_2Ti_2O_7$. To begin, we categorize the single ion process terms in the effective Hamiltonian in two distinct sets:

- Ion $i$ interacts with ion $k$ such that ion $k$ is excited to one of its crystal field excited states (Fig. 4.1(a)). In the second step, ion $k$ interacts back with same ion $i$ and returns to the crystal field ground state (Fig. 4.1(b)). If ion $k$ returns to its initial state, the net result of this virtual fluctuation of ion

$k$ is a renormalization of the crystal field ground state energy. On the other hand, if ion $k$ returns to a different state, the result of the process is a single ion transverse magnetic field at the position of ion $k$. It should be mention that there are allowed $J^x$, $J^y$ and $J^z$ matrix elements between the crystal field ground state and excited states. Therefore, all the discussed fluctuations are allowed between the states.

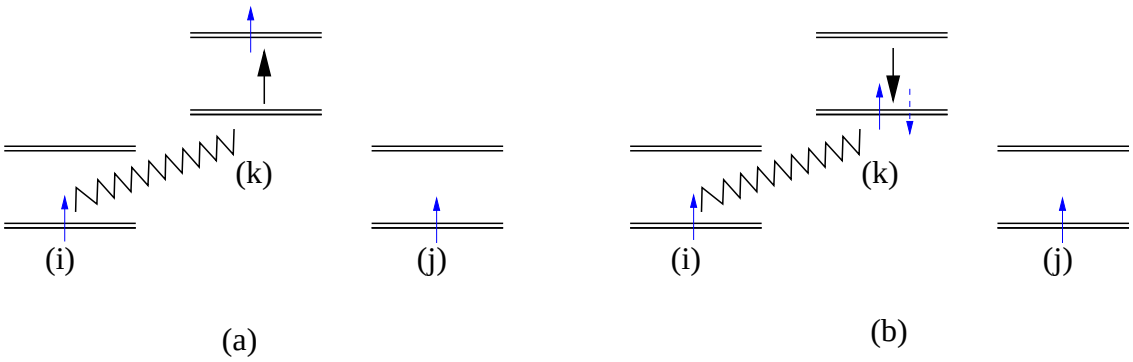


Figure 4.1: (a) Ion $i$ interacts with ion $k$ and excites it from the crystal field ground state to one of the crystal field excited states. (b) Ion $k$ interacts with ion $i$ and return to one of the states of the ground state. If the final state of the ground state is the same as the initial state this process renormalizes the crystal field ground state energy. However if the initial and final states of ion $k$ are different (dashed vector) this process creates a single ion transverse field at the site of ion $k$.

- Ion $i$ interacts with ion $k$ and excites it to one of the crystal field excited states (Fig. 4.2(a)). In the next step, ion $k$ interacts with another ion $j$ and returns to the crystal field ground state (Fig. 4.2(b)). If in this process ion $k$ returns to its initial state, an effective (mediated) interaction is created between ions $i$ and $j$ (Fig. 4.2(c)). Since in this process the states of ions $i$ and $j$ do not change, the derived effective interaction has the symmetry of the classical term, $PVP$ of the effective Hamiltonian. In the case that $PVP$ between ions $i$ and $j$ is zero, this process generates an interaction between ion $i$ and $j$ while if the $PVP$ term between ions $i$ and $j$ is not zero, this process renormalizes the classical term of the effective Hamiltonian. We name

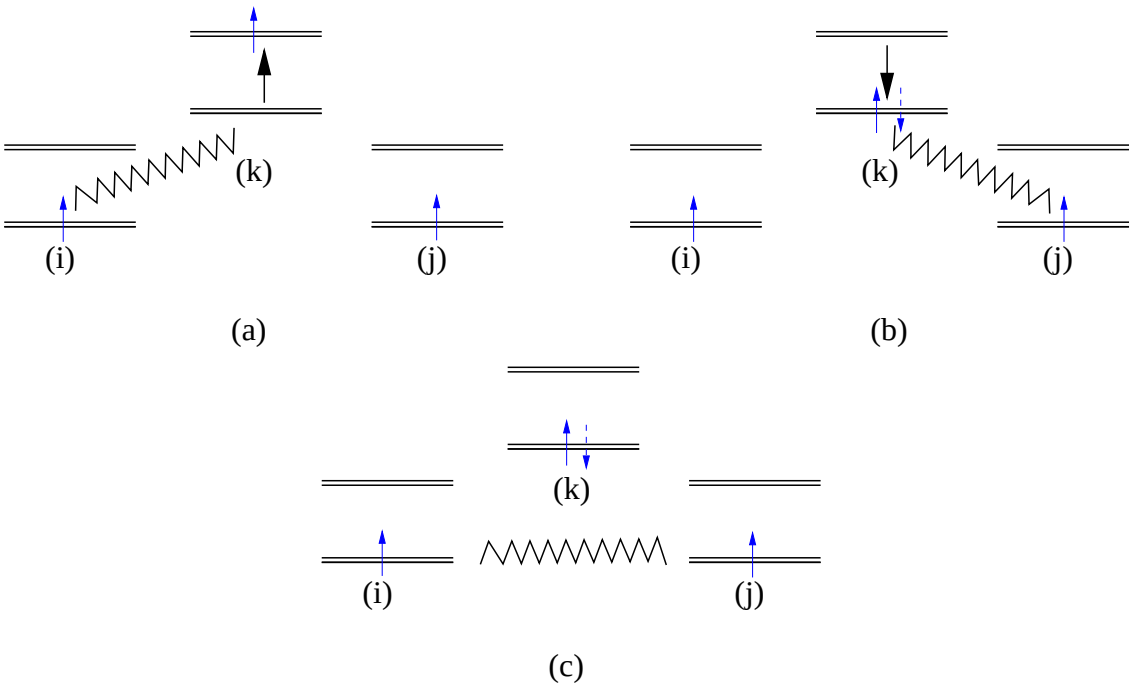


Figure 4.2: (a) Ion $i$ interacts with ion $k$ and excites it from the crystal field ground state to one of the crystal field excited states. (b) Ion $k$ interacts with ion $j$ and returns to one of the states of the ground state. If the final state of ion $k$ is the same as the initial state (solid spin vector) this process generates an effective interaction between ion $i$ and $j$ (c). If, however, the initial and final states of ion $k$ are different (dashed spin vector), this process creates a single ion transverse field at the site of ion $k$ (c).

this generated interaction, that has the local $\langle 111 \rangle$ Ising symmetry and is generated by the quantum fluctuations, a *quantum Ising interaction*. On the other, hand if the state of ion $k$ changes, the result of this process is a single ion transverse field at site $k$. Here we should comment that the single-ion transverse term discussed in part (a) becomes zero when we consider the tetragonal and translation symmetries of the system. Since all ions that surround a given ion $i$ create single ion transverse terms at the site of ion $i$ and are connected by the tetragonal and translation symmetries. As a result, the transverse terms created by these ions are also connected by the tetragonal symmetry and their sum is zero.

As an example of the importance of the quantum Ising interaction, we consider the pyrochlore lattice with only first nearest neighbor exchange interaction between ions. As we discuss it later for this lattice, the quantum Ising interaction renormalizes the exchange interaction between nearest neighbors and generates second and third nearest neighbor interactions between Ising spins. The quantum Ising interaction thus changes a classical first nearest neighbor Hamiltonian into an effective $\mathcal{J}_1$, $\mathcal{J}_2$ and $\mathcal{J}_3$ Hamiltonian on a pyrochlore lattice. The strength of these interactions depend on the matrix elements of $\mathbf{J}$ and the gap between the ground state and excited states. Although it seems that this is a small correction to the classical Hamiltonian, we can imagine cases in which this correction could be very important. For example, consider a frustrated system at the classical level. Any new term in the Hamiltonian, although small, can partially remove the frustration and change the physical properties of the system. In the next subsection, we calculate the quantum Ising term of the effective Hamiltonian for a general bi-particle Hamiltonian and then apply it to the perturbation Hamiltonian terms (4.10).

### Quantum Ising Interaction (QIT)

Following our discussion about the single ion process and especially the importance of the quantum Ising interaction, in this subsection, we calculate the quantum Ising interaction for a general bi-particle Hamiltonian and the crystal field levels of $Tb^{3+}$.

We start the calculations by considering a general case in which ions $i$ and $j$ interact with ion $k$ with the most general bi-particle Hamiltonian as

$$H_1 = D_{ij}^{\alpha\beta} J_i^{\alpha} J_j^{\beta} \,, \tag{4.11a}$$

$$H_2 = D_{jk}^{'\gamma\delta} J_j^{\gamma} J_k^{\delta} \,, \tag{4.11b}$$

Where, from now on, we use the sum rule in which repeated Greek indices indicates a sum over the three dimensional spin directions. As we discussed it in the previous section, to calculate the quantum Ising term we need to sum over all intermediate $Tb^{3+}$ ions in the system. In the following calculations we only consider one fluctuating ion ($k$) as the third ion. Substituting $H_1$ and $H_2$ in $PVRVP$ we obtain

$$\begin{aligned} H_{\text{eff}}^{\text{QIT}} &= |\phi_{i,0}^{(l_i)}\phi_{j,0}^{(p_j)}\phi_{k,0}^{(m_k)}\rangle\langle\phi_{i,0}^{(l_i)}\phi_{j,0}^{(p_j)}\phi_{k,0}^{(m_k)}| D_{ik}^{\alpha_1\alpha_2} J_i^{\alpha_1} J_k^{\alpha_2} \\ &\quad \sum_{n,r_k} \frac{|\phi_{i,0}^{(l_i)}\phi_{j,0}^{(p_j)}\phi_{k,n}^{(r_k)}\rangle\langle\phi_{i,0}^{(l_i)}\phi_{j,0}^{(p_j)}\phi_{k,n}^{(r_k)}|}{(E_k^0 - E_k^n)} \\ &\quad D_{jk}^{'\beta_1\beta_2} J_j^{\beta_1} J_k^{\beta_2} |\phi_{i,0}^{(l_i)}\phi_{j,0}^{(p_j)}\phi_{k,0}^{(t_k)}\rangle\langle\phi_{i,0}^{(l_i)}\phi_{j,0}^{(p_j)}\phi_{k,0}^{(t_k)}|, \end{aligned} \tag{4.12}$$

where $E_k^n$ is the energy of $n^{th}$ single ion crystal field level. We employ Eq. (4.7) to calculate the matrix elements of $\mathbf{J}$ in the local crystal field basis. Eq. (4.12) can be simplified as

$$\begin{aligned} H_{\text{eff}}^{\text{QIT}} &= |\phi_{i,0}^{(l_i)}\phi_{j,0}^{(p_j)}\phi_{k,0}^{(m_k)}\rangle\langle\phi_{i,0}^{(l_i)}\phi_{j,0}^{(p_j)}\phi_{k,0}^{(m_k)}| D_{ik}^{\alpha_1\alpha_2} u^{\alpha_1\gamma_1} u^{\alpha_2\gamma_2} \tilde{J}_i^{\gamma_1} \tilde{J}_k^{\gamma_2} \\ &\quad \sum_{n,r_k} \frac{|\phi_{i,0}^{(l_i)}\phi_{j,0}^{(p_j)}\phi_{k,n}^{(r_k)}\rangle\langle\phi_{i,0}^{(l_i)}\phi_{j,0}^{(p_j)}\phi_{k,n}^{(r_k)}|}{(E_k^0 - E_k^n)} \\ &\quad D_{jk}^{'\beta_1\beta_2} u^{\beta_1\eta_1} u^{\beta_2\eta_2} \tilde{J}_j^{\eta_1} \tilde{J}_k^{\eta_2} |\phi_{i,0}^{(l_i)}\phi_{j,0}^{(p_j)}\phi_{k,0}^{(t_k)}\rangle\langle\phi_{i,0}^{(l_i)}\phi_{j,0}^{(p_j)}\phi_{k,0}^{(t_k)}|, \end{aligned} \tag{4.13}$$

where $\tilde{J}_i^{\alpha}$ is the $\alpha$ component of the total angular momentum of ion $i$ in the local basis. Ions $i$ and $j$ can not change their states because $\langle\phi_{i,0}^{(l_i)}|\tilde{J}^{\alpha}|\phi_{i,0}^{(t_i)}\rangle$ is non-zero only if $\alpha$=$z$ and $l_i = t_i$ (the only non-zero $\mathbf{J}$ matrix elements in the crystal field ground state basis are diagonal $J^z$ matrix elements). Thus, Eq. (4.13) can be simplified by assuming $|\phi_{i,0}^{(l_i)}\rangle\langle\phi_{i,0}^{(l_i)}|\tilde{J}^{\alpha}|\phi_{i,0}^{(l_i)}\rangle\langle\phi_{i,0}^{(l_i)}| = |\langle J^z\rangle|\sigma_i^z$ (two states of the crystal field ground

state make an Ising spin) and using the fact that $\gamma_1 = z$ and $\eta_1 = z$;

$$H_{\text{eff}}^{\text{QIT}} = |\langle J^z \rangle|^2 \sum_{n\neq 0} u_i^{\alpha_1 z} u_k^{\alpha_2 \gamma_1} u_j^{\beta_1 z} u_k^{\beta_2 \gamma_2} D_{ik}^{\alpha_1 \alpha_2} D_{jk}^{'\beta_1 \beta_2}$$
$$\times \langle \phi_{k,0}^{(l_k)} | \tilde{J}_k^{\gamma_1} | \frac{|\phi_{k,n}^{(p_k)}\rangle\langle\phi_{k,n}^{(p_k)}|}{(E_k^0 - E_k^n)} | \tilde{J}_k^{\gamma_2} | \phi_{k,0}^{(l_k)} \rangle \sigma_i^z \otimes \sigma_j^z \ , \tag{4.14}$$

where $\sigma_i^z$ is the $z$ component of Pauli's sigma matrix and $\langle J^z \rangle$ is the matrix elements of operator $J^z$ in the crystal field ground state. We should mention that the effective coupling between two ions is a complicated function of matrix elements and the gap between the ground state and excited states. Eq. (4.14) is a general formula for calculating the quantum Ising coupling between ion $i$ and $j$ mediated by an ion $k$. As we mentioned before for a system of many ions, we have to sum this expression over all such third ions in the system.

Now we use this general Hamiltonian to derive the individual contribution to the quantum Ising term in Eq. (4.10). To simplify the labeling, we name each term of the effective Hamiltonian by the first initial of the two terms in the Hamiltonian that contribute to the effective Hamiltonian. For example, E-D interaction means that the first interaction ($H_1$) that connects the ground state to the excited state is the exchange interaction and the second interaction ($H_2$) which connects the excited state back to the ground state is the dipole-dipole interaction. For clarity, we present the calculations of quantum Ising interaction for each term in Eq. (4.10) in subsections.

### E-E Interaction

We consider a calculation of the first term of Eq. (4.10). In this term, ions interact via the first nearest neighbor interaction and hence both $H_1$ and $H_2$ are exchange interactions. Depending on the relative position of two interacting ions, two possibilities can occur:

**a.** For a pair of nearest neighbor ions there are only two other nearest neighbors making a tetrahedron with that pair (Fig. 4.4). These two ions are the only ions connected to the nearest neighbor pair by the exchange interaction and renormalize

the interaction between them. Substituting $D_{ij}^{\alpha\beta}$ and $D_{ij}^{'\alpha\beta}$ with $\mathcal{J}\delta^{\alpha\beta}$ in Eq. (4.14), the effective coupling between this pair of ions reads,

$$\begin{aligned}\mathcal{J}_1 &= 2|\langle J^z\rangle|^2 \sum_n \mathcal{J}^2 u_a^{\gamma_1 z} u_b^{\gamma_2 z} u_c^{\gamma_1\alpha_1} u_c^{\gamma_2\beta_1} \\ &\quad \langle\phi_{k,0}^{(l_k)}|\tilde{J}_k^{\alpha_1}|\frac{|\phi_{k,n}^{(p_k)}\rangle\langle\phi_{k,n}^{(p_k)}|}{(E_k^{(0)}-E_k^{(n)})}|\tilde{J}_k^{\beta_1}|\phi_{k,0}^{(l_k)}\rangle(1-\delta_{ac})(1-\delta_{bc}) \ , \end{aligned} \tag{4.15}$$

where $\mathcal{J}_1$ is the induced first nearest neighbor coupling between ions in lattice sites $\{i,a\}$ and $\{j,b\}$. In Fig. 4.3(a) this induced first nearest neighbor coupling is plotted as a function of the microscopic exchange coupling $\mathcal{J}$. The classical Ising curve in this plot shows the exchange coupling between Ising spins to first order in $PVP$ (Section 4.2).

**b.** If two ions are second or third nearest neighbors among themselves (Fig. 4.4), an effective second or third nearest neighbor interaction is created between them. Their effective couplings are

$$\begin{aligned}\mathcal{J}_2 &= |\langle J^z\rangle|^2 \sum_n \mathcal{J}^2 u_a^{\gamma_1 z} u_b^{\gamma_2 z} u_c^{\gamma_1\alpha_1} u_c^{\gamma_2\beta_1} \\ &\quad \langle\phi_{k,0}^{(m_k)}|\tilde{J}_k^{\alpha_1}|\frac{|\phi_{k,n}^{(p_k)}\rangle\langle\phi_{k,n}^{(p_k)}|}{(E_k^{(0)}-E_k^{(n)})}|\tilde{J}_k^{\beta_1}|\phi_{k,0}^{(l_k)}\rangle, \end{aligned} \tag{4.16a}$$

$$\begin{aligned}\mathcal{J}_3 &= |\langle J^z\rangle|^2 \sum_n \mathcal{J}^2 u_a^{\gamma_1 z} u_b^{\gamma_2 z} u_c^{\gamma_1\alpha_1} u_c^{\gamma_2\beta_1} \\ &\quad \langle\phi_{k,0}^{(l_k)}|\tilde{J}_k^{\alpha_1}|\frac{|\phi_{k,n}^{(p_k)}\rangle\langle\phi_{k,n}^{(p_k)}|}{(E_k^{(0)}-E_k^{(n)})}|\tilde{J}_k^{\beta_1}|\phi_{k,0}^{(l_k)}\rangle \ , \end{aligned} \tag{4.16b}$$

where $\mathcal{J}_2$ and $\mathcal{J}_3$ are, respectively, the induced second and third nearest neighbor exchange couplings.

We should mention that in the pyrochlore lattice there are two kinds of third nearest neighbors which are shown in Fig. 4.4. The first kind of third nearest neighbors which are directly connected by a third ion (shown with magenta line) and the second kind nearest neighbors which are not connected by the third ion (blue line). The third nearest neighbor coupling ($\mathcal{J}_3$) can only be created for the first kind of ions. A plot of the second and third nearest neighbor couplings as a function of exchange coupling $\mathcal{J}$ is shown in Fig. 4.3(b).

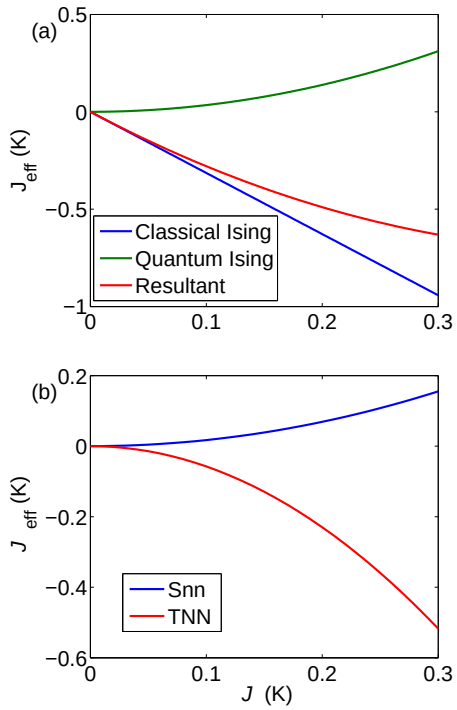


Figure 4.3: (a) Classical exchange interaction, quantum Ising interaction and the effective first nearest neighbor interaction (resultant) as a function of the classical exchange interaction in the local basis. (b) Generated second nearest neighbor (SNN) and third nearest neighbor (TNN) couplings by the quantum Ising interaction as a function of the classical exchange interaction $\mathcal{J}$.

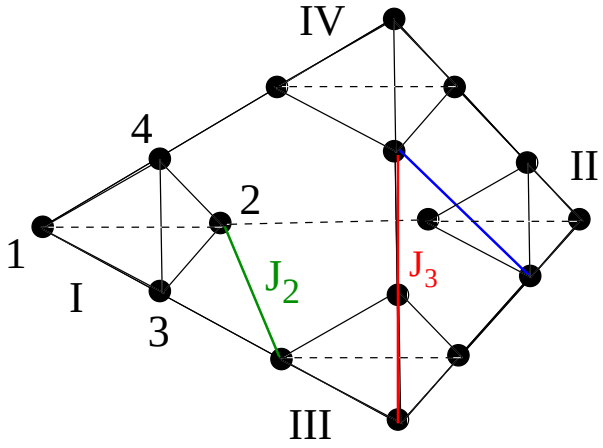


Figure 4.4: Generated first, second (green), and third nearest neighbor (red) interactions by the quantum Ising terms. Two ions that are connected by blue color line are third nearest neighbor, however, no third nearest neighbor interaction is created between them since they are connected by one $Tb^{3+}$ ion.

### E-D Interaction

In this subsection, we calculate the E-D contribution of the quantum Ising term. Therefore $H_1$ and $H_2$ are respectively exchange and dipole-dipole interactions plus their permutation. Owing to the dipole part of the generated effective interaction, the E-D term is a long-range interaction which drops off asymptotically as $\frac{1}{r^3}$, where $r$ is the distance between two ions. On the other hand, the exchange interaction is non-zero at the first nearest neighbor and, as a result, the only ions that renormalize the interaction are the six nearest neighbors of each ion. Writing the dipole-dipole interaction in the similar form as $H_2$ in Eq. (4.11b) reads

$$H_{\text{dipole}-\text{dipole}} = \sum_{ij;ab} \mathcal{D}^{\alpha\beta}_{ij;ab} J^{\alpha}_{i,a} J^{\beta}_{j,b} \,, \tag{4.17a}$$

$$\mathcal{D}^{\alpha\beta}_{ij;ab} = \frac{\mathcal{D}}{r^3_{ij;ab}} (\delta^{\alpha\beta} - 3(\hat{r}^{\alpha}_{i,a} \hat{r}^{\beta}_{j,b})) \,, \tag{4.17b}$$

where $\mathcal{D}_{ij;ab}$ is the coupling between ions at sites $\{i, a\}$ and $\{j, b\}$. Substituting the dipole-dipole coupling tensor $\mathcal{D}_{ij;ab}$ and the exchange $\mathcal{J}$ couplings in Eq. (4.14) the

quantum Ising term from the E-D interaction reads,

$$H_{\text{eff}}^{\text{E-D}} = |\langle J^z\rangle|^2 \sum_{\langle k,c\rangle}\sum_{n} \mathcal{J} u_a^{\alpha_1 z} u_c^{\alpha_2\gamma_1} u_b^{\beta_1 z} u_c^{\beta_1\gamma_2} \mathcal{D}_{ik;ac}^{\alpha_1\alpha_2} \mathcal{J} \langle\phi_{k,0}^{(l_k)}|\tilde{J}_k^{\gamma_1}|\frac{|\phi_{k,n}^{(p_k)}\rangle\langle\phi_{k,n}^{(p_k)}|}{(E_k^0 - E_k^n)}|\tilde{J}_k^{\gamma_2}|\phi_{k,0}^{(l_k)}\rangle \sigma_{i,a}^z \otimes \sigma_{j,b}^z + Per(i \leftrightarrow j)\ , \quad (4.18)$$

where $\langle k, c\rangle$ denotes the sum over the 6 nearest neighbors of ions $\{i, a\}$. For two ions separated by large distances ($r_{ik;ac} \gg a$ where $a$ is the nearest neighbor distance), we can approximate $r_{ik;ac}$ with $r_{ij;ab}$ because the sum over $k$ and $c$ is restricted to the first nearest neighbors ($r_{ik;ac} = a$). Hence, for two well separated ions the E-D interaction drops off as $\frac{1}{r_{ij;ab}^3}$ similarly to the dipole-dipole interaction. In Fig. 4.5 a log-log plot of the E-D coupling between two ions in the [100], [110] and [111] directions are depicted as a function of distance between them. For distances larger than few unit cells, the slope is exactly -3 which confirms our analytical argument that the interaction between two far ions drops off as $\frac{1}{r_{ij;ab}{}^3}$ as a function of distance between them. Different intercepts, observed in different directions in Fig. 4.5, show that the E-D coupling depends on the position vectors, their orientations in the space, and the sublattices of ions $i$ and $j$.

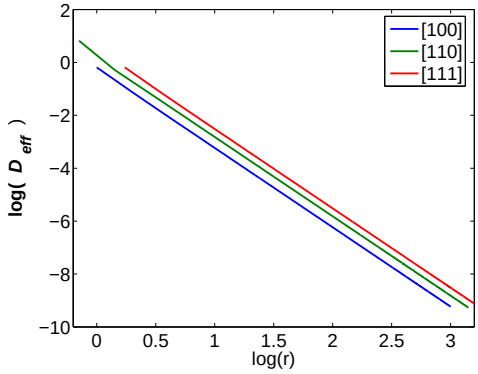


Figure 4.5: Log-log plot of the E-D coupling as a function of distance and for [100], [110] and [111] directions.

### D-D Interaction

Calculation of the D-D interaction is a much more difficult task than the E-D and E-E interactions. The difficulty is not only due to the long-range nature of the dipole-dipole interaction but is also from the sum over all third ions that mediate the interaction between two ions. Substituting the dipole-dipole coupling $\mathcal{D}_{ij}$ into Eq. (4.14) we derive the general formula for calculating the D-D interaction as

$$\begin{aligned} H_{\text{eff}}^{\text{D-D}} &= |\langle J^z \rangle|^2 \sum_k \sum_n u_i^{\alpha_1 z} u_k^{\alpha_2 \gamma_1} u_j^{\beta_1 z} u_k^{\beta_2 \gamma_2} \mathcal{D}_{ik}^{\alpha_1 \alpha_2} \mathcal{D}_{jk}^{\beta_1 \beta_2} \\ &\quad \langle \phi_{k,0}^{(l_k)} | \tilde{J}_k^{\gamma_1} | \frac{|\phi_{k,n}^{(p_k)}\rangle\langle\phi_{k,n}^{(p_k)}|}{(E_k^0 - E_k^n)} | \tilde{J}_k^{\gamma_2} | \phi_{k,0}^{(l_k)} \rangle \sigma_i^z \otimes \sigma_j^z \ . \end{aligned} \tag{4.19}$$

A general method for calculating this sum is to consider a sphere with its center at the middle of two ions whose radius is much larger than the distance between them and sum over all ions inside the sphere (Fig. 4.6). The radius of the sphere is much larger than the distance between two ions, $r_{12}$. We can assume that for ion $k$ outside of the sphere $r_{1k}$=$r_{2k} = R$. As a result, for the ions outside the sphere the D-D interaction which is the multiplication of two dipole-dipole interactions drops of as $\frac{1}{R^6}$. We can thus neglect the contribution of these ions to D-D interaction. This cut off method only works for two close ions where $R$ is not very large and the computation is feasible.

For two well separated ions, the sum must be calculated exactly which makes the computation unfeasible. However, our numerical calculation for two far ions shows that the D-D interaction drops off as $\frac{1}{r_{12}^3}$, where $r_{12}$ is the distance between two ions. In Fig. 4.7 we depict the log-log plot of the D-D coupling as a function of $r_{12}$. For large distance ($r_{12} > 10a$) the slope of this coupling is -3 showing that this interaction is proportional to $\frac{1}{r_{12}^3}$ for two distance ions. In Chapter 7, we show that for the given exchange, $\mathcal{J}$, and dipole-dipole, $\mathcal{D}$, couplings of $Tb_2Ti_2O_7$ , the D-D coupling is at least three times smaller than the E-D coupling.

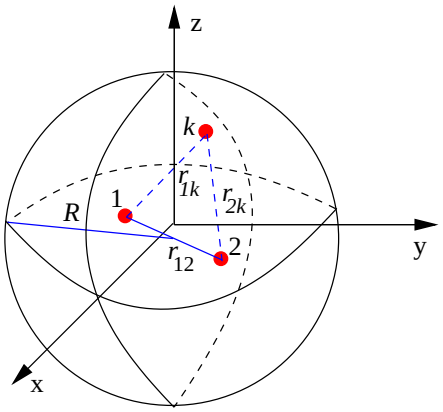


Figure 4.6: All ions inside the sphere (such as ion $k$) renormalize the interaction between ion 1 and 2. For ions outside of the sphere with radius $R \gg r_{12}$ the interaction drops off as $\frac{1}{R^6}$ and we neglect their contribution in the sum over $Tb^{3+}$ ions.

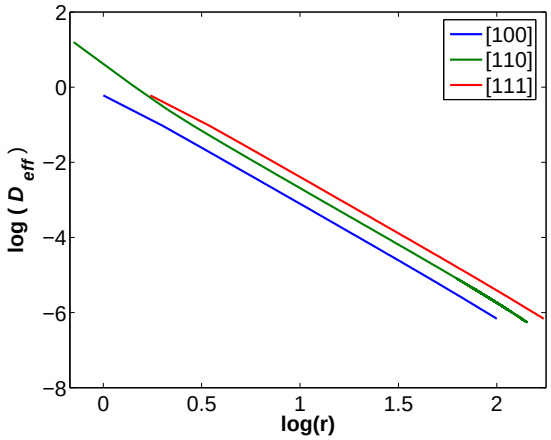


Figure 4.7: Log-log plot of the D-D coupling as a function of distance and for [100], [110] and [111] directions.

## 4.4 Two Ion Excitations

In the previous section we discussed and calculated the effective Hamiltonian due to virtual single ion crystal field excitations. In this section, we continue the discussion by considering virtual two-ion excitations and derive a relevant formula to calculate the effective Hamiltonian for this process. In contrast to the single ion excitations, which give the same symmetry as the classical Ising part of the effective Hamiltonian, two ion excitations have a different symmetry than the classical term of the effective Hamiltonian. To explain this, we use the four lowest crystal field states of $Tb^{3+}$ ion and show that the matrix elements between the two states of the crystal field ground state is not zero in the presence of a bi-particle interaction. This is because the interaction creates quantum fluctuations from the ground state to the excited states and the net result of these quantum fluctuations can be considered as induced matrix elements between the two states of the ground state. These non-zero matrix elements can be interpreted as the transverse terms in the pseudo-spin 1/2 effective Hamiltonian in which the two states of the crystal field ground state map to the spin up and spin down states of the pseudo-spin.

### 4.4.1 Two Ion Excitations, Spin Flip Mechanism and Transverse Magnetic Field

In the second chapter, we mentioned that all the matrix elements of $\mathbf{J}$ are zero within the crystal field ground state doublet except the diagonal terms of the $J^z$ matrix element and we mapped the two states of the ground state to a local $\langle 111 \rangle$ Ising spin. In this section, we show that the virtual transitions between the crystal field ground state and the first excited state mediated via magnetic interactions creates matrix elements between the two states of the crystal field ground state. These virtual transitions create terms in the effective Hamiltonian which have a different symmetry from the local $\langle 111 \rangle$ Ising symmetry and is the microscopic source for the insufficiency of the Ising assumption for a description of $Tb_2Ti_2O_7$.

In Fig. 4.8 we show the crystal field ground state and first excited state doublets for a single $Tb^{3+}$ ion, separately, to illustrate the different matrix elements that exist

between them. We call the two states of the ground state doublet $|1\rangle$ and $|2\rangle$, and the two states of the first crystal field excited state doublet $|3\rangle$ and $|4\rangle$. Their eigenfunctions in the $J^z$ basis are given in Table 2.4.

Imagine a magnetic interaction between two $Tb^{3+}$ ions $i$ and $j$ where the ion $i$ is in state $|1\rangle$ and ion $j$ is in the state $|2\rangle$ (Fig. 4.9(a)). The i interaction between two ions can excite ion $i$ from state $|1\rangle$ to state $|3\rangle$ and ion $j$ from state $|2\rangle$ to state $|4\rangle$ by $J^x$ or $J^y$ matrix elements $PVR = \langle 1_i 2_j | J_i^\alpha J_j^\beta | 3_i 4_j \rangle$ (Fig. 4.9(b)). These ions return the ground state by interacting with each other. In this process ion $i$ can transit from state $|3\rangle$ to state $|2\rangle$ and ion $j$ form state $|4\rangle$ to state $|1\rangle$ via $J^z$ operator $RVP = \langle 3_i 4_j | J_i^\alpha J_j^\beta | 2_i 1_j \rangle$ (Fig. 4.9(c)). The net result of these processes is a transition of ion $i$ state $|1\rangle$ to state $|2\rangle$ and ion $j$ from state $|2\rangle$ to state $|1\rangle$. This change of states within the manifold of the crystal field ground state can be interpreted as a spin flip mechanism in the pseudo-spin 1/2 representation in which two states of the crystal field ground state are mapped to spin up and spin down states.

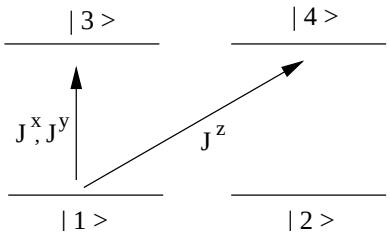


Figure 4.8: The ground state and first excited state of the crystal field Hamiltonian. Two degenerate states of the ground state ($|1\rangle$ and $|2\rangle$) and first excited state ($|3\rangle$ and $|4\rangle$) are drawn separately to show the different matrix elements at play between these states.

Another important process that we need to mention is the creation of single ion transverse field via the two ion excitations. In this process ion $i$ interacts twice with ion $j$ and is excited from one of the states of the ground state doublet to the excited states and comes back to the same state of the ground state doublet. At the same time, ion $j$ undergoes the same process with the difference that it is flipped from one state to the other state of the ground state doublet. The net result of this

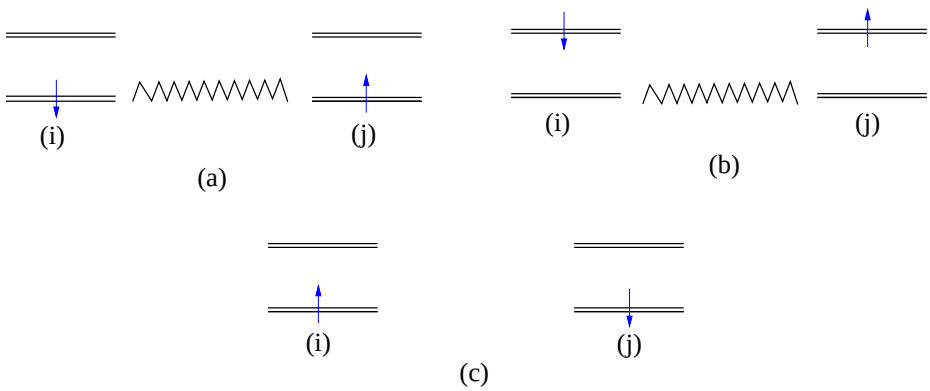


Figure 4.9: Spin flip mechanism via the crystal field excited states in $Tb_2Ti_2O_7$. Ion $i$ interacts with ion $j$ (a) and both ions are excited to one of the excited states (b). This state of the system is energetically unstable, hence they interact again and come back to the ground state with the difference that the states of ion $i$ and $j$ are changed.(c).

process leaves the state of ion $i$ unchanged and changes the state of ion $j$. Within the manifold of the ground state doublet, in which the two states of the ground state map to the spin up and spin down states, this process can be described by a term in the effective Hamiltonian such as $\Gamma S_j^x$ or $\Gamma S_j^y$, where $\mathbf{S}$ is the pseudo-spin 1/2 operator. We comment about this single ion transverse fields in this section.

### Effective Hamiltonian of Two Ion Excitations

Having discussed the two important processes for the two ion excitation, we derive in this section a formalism to calculate an effective Hamiltonian generated by two ion excitations. Considering the two terms $H_1$ and $H_2$ in Eq. (4.11a) and (4.11b) and substituting them into the second order perturbation theory (Eq. (4.4a)) leads to an effective Hamiltonian given by

$$\begin{aligned} H_{\text{eff}} &= |\phi_{i,0}^{(p_i)}\phi_{j,0}^{(p_j)}\rangle\langle\phi_{i,0}^{(p_i)}\phi_{j,0}^{(p_j)}|D_{ij}^{\alpha_i\alpha_j}J_i^{\alpha_i}J_j^{\alpha_j} \\ &\quad [\frac{|\phi_{i,n}^{(r_i)}\phi_{j,m}^{(r_j)}\rangle\langle\phi_{i,n}^{(r_i)}\phi_{j,m}^{(r_j)}|}{(E_i^0+E_j^0-E_i^n-E_j^m)}]D_{ij}^{'\beta_i\beta_j}J_i^{\beta_i}J_j^{\beta_j}|\phi_{i,0}^{(s_i)}\phi_{j,0}^{(s_j)}\rangle\langle\phi_{i,0}^{(s_i)}\phi_{j,0}^{(s_j)}|\,, \end{aligned} \quad (4.20)$$

where $|\phi_{i,0}^{(p_i)}\rangle$ is the $p_i^{th}$ state of the crystal field ground state doublet of ion $i$, $|\phi_{i,n}^{(r_i)}\rangle$ is the $r_i$ state of the $n$th degenerate crystal field level of ion $i$, $E_i^0$ is the crystal field ground state energy, $E_i^n$ is the energy of the $n^{\text{th}}$ crystal field level and $J_i^{\alpha_i}$ is the $\alpha_i^{th}$ component of the total angular momentum operator for ion $i$. With double excitation, and to this order of perturbation theory, only two spins can participate in each process because $PV_{ij}RV_{kl}P$ is non-zero when $i=k$ and $j=l$, or $i=l$ and $j=k$, otherwise the orthonormality of the crystal field states make this term vanish. Based on Eq. (4.20) we can calculate different terms emerging from substituting $H_1$ and $H_2$ with exchange and dipole-dipole interactions.

We first consider the simplest case where both $H_1$ and $H_2$ are exchange interactions and substitute them in Eq. (4.20). Since the operator $\mathbf{J}$ is expressed in a global basis and the crystal field states are expressed in a local basis, one has to use Eq. (4.7) to determine the matrix elements of operator $\mathbf{J}$ in the crystal field basis. Doing this calculation we derive the effective Hamiltonian as,

$$\begin{aligned} H_{\text{eff}} &= \mathcal{J}^2|\phi_{i,0}^{(l_i)}\phi_{j,0}^{(m_j)}\rangle\langle\phi_{i,0}^{(l_i)}\phi_{j,0}^{(m_j)}|u_a^{\alpha_1\alpha_2}u_b^{\alpha_1\beta_2}\tilde{J}_a^{\alpha_2}\tilde{J}_b^{\beta_2}[\sum_{rn;t_ip_j}\frac{|\phi_{i,r}^{(t_i)}\phi_{j,n}^{(p_j)}\rangle\langle\phi_{i,r}^{(t_i)}\phi_{j,n}^{(p_j)}|}{(2E_i^{(0)}-E_i^{(r)}-E_j^{(n)})}] \\ &\quad u_a^{\gamma_1\gamma_2}u_b^{\gamma_1\theta_2}\tilde{J}_a^{\gamma_2}\tilde{J}_b^{\theta_2}|\phi_{i,0}^{(l_i)}\phi_{j,0}^{(l_k)}\rangle\langle\phi_{i,0}^{(l_i)}\phi_{j,0}^{(l_j)}|\,, \end{aligned} \tag{4.21}$$

where $u_a^{\alpha\beta}$ is the $\alpha\beta$ component of the transformation matrix from the global to the local axis for an ion on sublattice $a$, $\tilde{J}_a^{\alpha}$ is the $\alpha^{th}$ component of the total angular momentum in sublattice $a$ and in the local basis.

The next step in calculating the two ion excitation is to substitute $H_1$ and $H_2$ in Eq. (4.20) with exchange and dipole-dipole interactions, respectively, and their permutations. Calculating the matrix elements of operator $\mathbf{J}$ in the local basis, the effective Hamiltonian reads

$$\begin{aligned} &H_{\text{eff}} = \mathcal{J}\mathcal{D}_{ij;ab}^{\alpha_1\alpha_2}|\phi_{i,0}^{(l_i)}\phi_{j,0}^{(m_j)}\rangle\langle\phi_{i,0}^{(l_i)}\phi_{j,0}^{(m_j)}|u_a^{\alpha_1\beta_1}u_b^{\alpha_2\beta_2}\tilde{J}_a^{\beta_1}\tilde{J}_b^{\beta_2} \\ &[\sum_{rn;t_ip_j}\frac{|\phi_{i,r}^{(t_i)}\phi_{j,n}^{(p_j)}\rangle\langle\phi_{i,r}^{(t_i)}\phi_{j,n}^{(p_j)}|}{(2E_i^{(0)}-E_i^{(r)}-E_j^{(n)})}]u_a^{\gamma_1\gamma_2}u_b^{\gamma_1\theta_2}\tilde{J}_a^{\gamma_2}\tilde{J}_b^{\theta_2}|\phi_{i,0}^{(l_i)}\phi_{j,0}^{(l_k)}\rangle\langle\phi_{i,0}^{(l_i)}\phi_{j,0}^{(l_j)}| \\ +\quad &\text{Per}\{i\to j;a\to b\}, \end{aligned} \tag{4.22}$$

where $\mathcal{D}_{ij;ab}$ is the dipole-dipole coupling defined in Eq. (4.17b). This term of the

effective Hamiltonian is non-zero only for nearest neighbor ions due to the exchange interaction.

The last term to discuss is generated by substituting both $H_1$ and $H_2$ in Eq. (4.20) with the dipole-dipole interaction. Following the same prescription as the previous, terms this term of the effective Hamiltonian reads

$$H_{\text{eff}} = \mathcal{D}^{\kappa_1\kappa_2}_{ij;ab}\mathcal{D}^{\alpha_1\alpha_2}_{ij;ab}|\phi^{(l_i)}_{i,0}\phi^{(m_j)}_{j,0}\rangle\langle\phi^{(l_i)}_{i,0}\phi^{(m_j)}_{j,0}|u^{\alpha_1\beta_1}_a u^{\alpha_2\beta_2}_b \tilde{J}^{\beta_1}_a \tilde{J}^{\beta_2}_b$$
$$[\sum_{rnt_ip_j}\frac{|\phi^{(t_i)}_{i,r}\phi^{(p_j)}_{j,n}\rangle\langle\phi^{(t_i)}_{i,r}\phi^{(p_j)}_{j,n}|}{(2E^{(0)}_i - E^{(r)}_i - E^{(n)}_j)}]u^{\kappa_1\gamma_2}_a u^{\kappa_2\theta_2}_b \tilde{J}^{\gamma_2}_a \tilde{J}^{\theta_2}_b|\phi^{(l_i)}_{i,0}\phi^{(l_k)}_{j,0}\rangle\langle\phi^{(l_i)}_{i,0}\phi^{(l_j)}_{j,0}|. \quad (4.23)$$

Notice that this term converges very fast as $\frac{1}{r^6_{ij;ab}}$ where $r_{ij;ab}$ is the distance between two ions ($\mathcal{D}^{\alpha_1\alpha_2}_{ij;ab}\mathcal{D}^{\kappa_1\kappa_2}_{ij;ab} \propto \frac{1}{r^6_{ij;ab}}$). To derive the total effective Hamiltonian generated by the two-ion excitations we sum up Eqs. (4.21), (4.22) and (4.23) over all the ions in the lattice and map them to a pseudo-spin 1/2 system as,

$$H_{\text{eff}} = \sum_{i,a;j,b}\jmath^{\alpha\beta}_{ij;ab}\sigma^{\alpha}_{i,a}\sigma^{\beta}_{j,b} + \sum_{i,a}\Gamma^x_{i,a}\sigma^x_{i,a} + \Gamma^y_{i,a}\sigma^y_{i,a}\ , \quad (4.24)$$

where $\jmath_{ij;ab}$ is the effective coupling between pseudo-spins at $\{i,a\}$ and $\{j,b\}$ and $\Gamma^x_{i,a}$ and $\Gamma^y_{i,a}$ are the transverse fields in $x$ and $y$ directions at lattice point $i$ and sublattice $a$. The effective couplings and transverse fields are a function of the exchange and dipole-dipole couplings, the gap between the ground state and the excited state and the matrix elements of the angular momentum between the ground state and excited states. In general $\jmath^{\alpha\beta}_{ij;ab}$ can have different combinations of spatial components and therefore the derived effective Hamiltonian breaks Ising symmetry of the classical term of the effective Hamiltonian $PVP$. The single-ion transverse fields break the time-reversal symmetry for a pair of ions. However, these single-ion transverse fields cancel out each other, recovering the tetragonal and inversion symmetry of $Tb_2Ti_2O_7$. This is because all environmental $Tb^{3+}$ ions around ion $i$ transform to each other by the point symmetry group of the lattice. Hence, any transverse field created by an ion at site $i$ is cancelled out by the transverse fields created by the point symmetry transformed versions of ion $i$.

## 4.5 Summary

In this chapter, we derived a general formalism for calculating the effective Hamiltonian of $Tb_2Ti_2O_7$. Considering the fact that crystal field gap between the ground state and first excited state doublets is much larger than the exchange and dipole-dipole couplings, we chose the crystal field Hamiltonian as the model Hamiltonian and the interacting Hamiltonian as the perturbation. We showed that, to first order, the effective Hamiltonian is made of local $\langle 111 \rangle$ Ising spins interacting via the exchange and dipole-dipole interactions and we called this term a classical Ising term. We showed that to second order of perturbation, the virtual single ion excitations give a new contribution that we call quantum Ising term and which also has local $\langle 111 \rangle$ Ising symmetry. These terms renormalize the interaction at the classical Ising level and also create new terms such as second and third nearest neighbors into the effective Hamiltonian. We presented a method for calculating the quantum Ising term for all allowed combinations of exchange and dipole-dipole interactions. By considering the two-ion excitations to second order of perturbation, we found a channel for spin flip mechanism via the crystal field excited states and we showed that this mechanism changes the symmetry of the magnetic moments from $\langle 111 \rangle$ Ising spins to more isotropic effective spins.

# Chapter 5

# Single Tetrahedron Approximation

We discussed in Chapter 1 that the diffuse neutron scattering experiment on $Tb_2Ti_2O_7$ down to 60mK shows that the magnetic correlation length remains of the order of the nearest neighbor interatomic distance [27, 28]. Therefore, any reasonable model which gives the correlation function at the first nearest neighbor may be a good candidate to describe some of the physical properties of $Tb_2Ti_2O_7$. In $Tb_2Ti_2O_7$, four $Tb^{3+}$ ions on a single tetrahedron make the smallest magnetic building block. Hence, a non-interacting single tetrahedron approximation is a good approximation for describing the correlation functions in $Tb_2Ti_2O_7$. In this approximation it is assumed that the pyrochlore lattice is made of non-interacting tetrahedra and there is only interactions between the four $Tb^{3+}$ ions or individual tetrahedra. This approximation has been used in other frustrated systems such as the classical Heisenberg model on the pyrochlore lattice and gives a very good results in good agreement with the exact results [18, 43]. In this Chapter we calculate the phase diagram of $Tb_2Ti_2O_7$ at zero temperature using four lowest crystal field states per $Tb^{3+}$ ion and in the single tetrahedron approximation. In this phase diagram we plot the exchange coupling as a function of the gap between the crystal field ground state and first excited state. We show that the ground state of $Tb_2Ti_2O_7$ in the single tetrahedron approximation is a singlet state which is a linear

combination of all two-in/two-out states plus a small contribution from the excited crystal field states. We also use the effective Hamiltonian method of Chapter 4 and calculate the phase diagram from the effective Hamiltonian and compare it with exact results with four and six crystal field states per ion for a single-tetrahedron. This single tetrahedron calculation therefore allows us to assess the quantitative range of validity of the effective Hamiltonian description based on second order perturbation theory.

## 5.1 Single Tetrahedron Approximation

In this section we introduce a Hamiltonian to describe $Tb_2Ti_2O_7$ in a single tetrahedron approximation and choose the crystal field basis for calculating the properties of $Tb_2Ti_2O_7$. We use this Hamiltonian to calculate a phase diagram and diffuse neutron scattering of $Tb_2Ti_2O_7$ in the single tetrahedron approximation. In the single tetrahedron approximation the Hamiltonian reads,

$$\begin{aligned} H &= \sum_{a}^{4} (H_{\rm cf})_a + \mathcal{J} \sum_{ab;a>b} \mathbf{J}_a \cdot \mathbf{J}_b \\ &+ \mathcal{D} r_{\rm nn}^3 \sum_{a>b} \frac{\mathbf{J}_a \cdot \mathbf{J}_b}{|\mathbf{r}_{ab}|^3} - \frac{3(\mathbf{J}_a \cdot \mathbf{r}_{ab})(\mathbf{J}_b \cdot \mathbf{r}_{ab})}{|\mathbf{r}_{ab}|^5} \,, \end{aligned} \tag{5.1}$$

where $H_{\rm cf}$ is the crystal field Hamiltonian for $Tb^{3+}$ ion in $Tb_2Ti_2O_7$ given in Eq. (2.13), $\mathcal{J}$ is the exchange coupling, $\mathcal{D}$ is the dipolar coupling at nearest neighbor, $\mathbf{J}_a$ is the J=6 total angular momentum operator and $\mathbf{r}_{ab}$ is the vector position between ions in sublattices $a$ and $b$. The estimated values of $\mathcal{J}$ and $\mathcal{D}$ for $Tb_2Ti_2O_7$ are, respectively, 0.167 K and 0.0315 K. To simplify the equations we write down Hamiltonian (5.1) as,

$$H = \sum_{a=1}^{4} H_a^{\rm cf} + \sum_{ab} \mathcal{F}_{ab}^{\alpha\beta} J_a^{\alpha} J_b^{\beta} \,, \tag{5.2a}$$

$$\mathcal{F}_{ab}^{\alpha\beta} = \mathcal{J}\delta^{\alpha\beta} + \mathcal{D}(\delta^{\alpha\beta} - 3(\hat{r}_a^{\alpha}\hat{r}_b^{\beta})) \,, \tag{5.2b}$$

where $\hat{r}_a^{\alpha}$ is the $\alpha$ component of the unit vector of the position vector of sublattice $a$ and $\mathcal{F}_{ab}$ is the coupling between ions at sublattices $a$ and $b$. It was discussed

in Section 4.1 that the crystal field basis is a good basis, and we use this basis to calculate the matrix elements of the Hamiltonian. We define the four-body basis state as the direct product of the single-ion crystal field states as,

$$|\Phi_{\{n\},\{m\}}\rangle \;=\; \prod_{a=1}^{4} |\phi_{a,n_a}^{(m_a)}\rangle \;, \tag{5.3}$$

where $|\phi_{a,n_a}^{(k_a)}\rangle$ is the $k_a^{th}$ state of the $n_a^{th}$ energy level of the crystal field for ion on sublattice $a$. Because the eigenstates of the crystal field Hamiltonian are in the local Cartesian frame and, the angular momentum operators expressed in the interacting Hamiltonian are in the global Cartesian frame we use the transformation theorem (Eq. (4.7)) to calculate the matrix elements of the interacting part of the Hamiltonian. After applying this transformation the matrix elements of Hamiltonian (5.2a) in this basis are,

$$\begin{aligned}\langle\Phi_{\{n\},\{m\}}|H|\Phi_{\{k\},\{l\}}\rangle \;=\; & \sum_{a}^{4} E_a^n + \sum_{a>b} \mathcal{F}_{ab}^{\alpha_1\beta_1} u_a^{\alpha_1\alpha_2} u_b^{\beta_1\beta_2} \\ & \langle\phi_{a,n_a}^{(m_a)}|\tilde{J}_a^{\alpha_2}|\phi_{a,k_a}^{(l_a)}\rangle\langle\phi_{b,n_b}^{(m_b)}|\tilde{J}_b^{\beta_2}|\phi_{b,k_b}^{(l_b)}\rangle,\end{aligned} \tag{5.4}$$

where $u_a^{\alpha\beta}$ is the $\alpha\beta^{th}$ component of the transformation matrix from the global axis to the local easy axis for sublattice $a$ and, $\tilde{J}^{\alpha}$ is the $\alpha$ component of the total angular momentum for a $Tb^{3+}$ ion in the local frame ( Appendix C). In the rest of this chapter, we use this Hamiltonian to calculate the physical properties of $Tb_2Ti_2O_7$ within the single tetrahedron approximation.

## 5.2 Phase Diagram of $Tb_2Ti_2O_7$ in the Single Tetrahedron Approximation

In this section we calculate the zero-temperature phase diagram of $Tb_2Ti_2O_7$ in the single tetrahedron approximation with the two states of the ground state doublet and also with the four states of the crystal field ground state and first excited state. We use the four lowest crystal field states because, while working with four ions and thirteen crystal field states per ion is doable, it needs a needlessly

large amount of computational resources. Moreover, using the four lowest crystal field states gives quantitative results in agreement with a calculation using thirteen states per ion. This can be naively justified based on the fact that the four lowest crystal field states are well separated from the rest of the excited states by a further energy gap of 100 K (Section 2.2). We also confirmed this assumption quantitatively by showing that the phase diagram and the diffuse neutron scattering do not change by including more crystal field states into the calculation.

We start the calculation by finding the phase diagram of a single tetrahedron considering only two states of the ground state doublet per ion. These two states of the ground state (Section 4.2) make a local $\langle 111 \rangle$ Ising spin. This model was discussed in Section 1.2 and because of its importance for our discussion it is restated here. For this system of Ising spins, the number of states are 16 and, using this basis of states, we determine the eigenstates and eigenvalues of Hamiltonian (5.4). By varying the exchange and dipole-dipole couplings two (collective) ground states are obtained: the all-in/all-out state where all Ising spins are either parallel or anti-parallel to the local $\langle 111 \rangle$ axis and, the two-in/two-out state where two Ising spins are parallel and two other Ising spins are anti-parallel to the local easy axis. The two-in/two-out state is six-fold degenerate and it is frustrated on the pyrochlore lattice (Section 1.2) [25]. The transition from all-in/all-out state to two-in/two-out state occurs at $\mathcal{J} = 5\mathcal{D}$ (Because of the different orientation of easy axis the effective exchange coupling between Ising spin is $\frac{\mathcal{J}|\langle J^z \rangle|^2}{3}$ and effective dipole-dipole coupling is $\frac{5\mathcal{D}|\langle J^z \rangle|^2}{3}$). The parameters for $Tb_2Ti_2O_7$ give the all-in/all-out state as the ground state (Fig. 5.1).

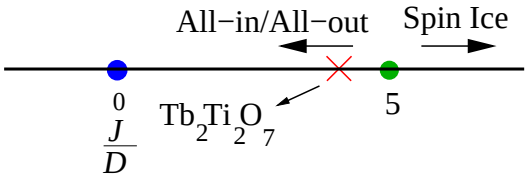


Figure 5.1: Classical phase diagram of a local $\langle 111 \rangle$ Ising spins in a single tetrahedron approximation. $Tb_2Ti_2O_7$ with $\frac{\mathcal{J}}{\mathcal{D}}$=5.3, should be in the all-in/all-out phase within a classical $\langle 111 \rangle$ Ising model description.

Before we start to incorporate the effect of the first excited crystal field state into the calculation, we need to mention an important point about the crystal field states. In Fig. 5.2, the ground state and first excited state of the crystal field Hamiltonian with the **J** matrix elements between them is depicted. In Section 4.4, we introduced a crystal field fluctuation channel via which generates matrix elements between the two states of the ground state doublet. One of the important elements for the presence of this channel is the non-zero $J^z$ value of matrix elements between the states of the ground state and the first excited state. If we artificially remove these matrix elements, the manifold of the crystal field states breaks in two subsets of states with states $|1\rangle$ and $|3\rangle$ in one subset and states $|2\rangle$ and $|4\rangle$ in the other subset. These subsets behave like Ising spins in which each state of the Ising state has one corresponding excited state. Hence, with zero off-diagonal $J^z$ matrix elements the Ising symmetry of the system in the ground state cannot be broken by the excited states. We can use this fact to track down the quantum Ising terms in the exact calculation that uses four crystal field states per ion. To investigate this artificial case, which will prove crucial in understanding what follows, we set the $J^z$ matrix elements laying between the states of the ground state doublet and states of the first excited state doublet to zero and calculate the phase diagram of the system.

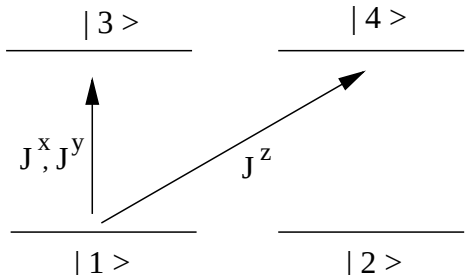


Figure 5.2: The ground state and the first excited states of the crystal field Hamiltonian. Two states of the ground state and first excited states are plotted separately to show the different matrix elements between these states. There are no matrix elements between the two states of the ground state via the excited states if the $J^z$ matrix elements are zero.

Following the above discussion, we use the four lowest crystal field states with

zero off-diagonal $J^z$ matrix elements to calculate the phase diagram of the system. The number of states for four $Tb^{3+}$ ions and four states per ion is $4^4$=256. We calculate the matrix elements of Hamiltonian (5.4) in this basis, using the exact diagonalization method, and we diagonalize the resulting 256×256 matrix and find its eigenvalues and eigenstates. The eigenstates of the system can be divided in two sets:

- The sixteen lowest states which are decomposed into one doublet, one sextet and one octet.
- All the remaining excited states (256-16=240) which are separated from the ground state by a gap of at least 15K.

Varying the exchange and dipole-dipole couplings, two states are found as the ground state of the system (four interacting $Tb^{3+}$ ions on a tetrahedron). A doublet state which is mostly comprised of the all-in/all-out classical states plus a small part of the crystal field excited states, and a sextet state which is comprised mostly of the two-in/two-out classical states plus a small part of the crystal field excited states. We mention that we also refer at times to the two states of the ground state doublet as the "in" and "out" states.

To investigate the role of the excited crystal field states on the $\frac{\mathcal{J}}{\mathcal{D}}$ phase diagram, we use the gap between the ground state and the first excited state, $\Delta$, as a free parameter that controls the strength of the quantum fluctuation via the excited crystal field states. However, $\frac{1}{\Delta}$ is more suitable for displaying this strength since, for $\frac{1}{\Delta}$=0, the quantum fluctuations between the crystal field ground state and first excited state are zero and by increasing the value of $\frac{1}{\Delta}$, the fluctuations become stronger. We determine the phase boundary between the sextet and the doublet states as a function of $\frac{1}{\Delta}$ and for $\mathcal{D}$=0.0315 K, the dipolar coupling strength appropriate for $Tb_2Ti_2O_7$.

The resulting phase diagram is shown in Fig. 5.3. The boundary between the doublet and the sextet states, which have their predominant weight respectively in the all-in/all-out and two-in/two-out states, is moved towards the doublet state compared to the classical phase boundary (dashed line in Fig. 5.3). This upward

shift of the boundary is essential in understanding the physics of $Tb_2Ti_2O_7$ within the present single tetrahedron approximation because, for the given couplings of $Tb_2Ti_2O_7$, $Tb_2Ti_2O_7$ is in the sextet (spin ice like) state instead of the doublet state of the classical phase diagram. We stress here that this sextet state is frustrated and this may play a key role in understanding the resurgence of quantum fluctuations in $Tb_2Ti_2O_7$ at very low temperatures.

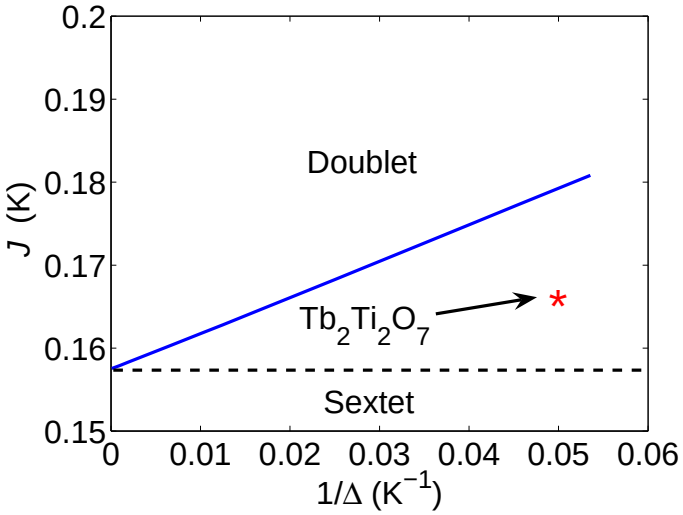


Figure 5.3: Phase diagram of $Tb_2Ti_2O_7$ with four lowest crystal field states and zero off-diagonal $J^z$ matrix elements in the single tetrahedron approximation and with $\mathcal{D}$=0.0315 K. In this phase diagram the exchange interaction is plotted as a function of $\frac{1}{\Delta}$ and $Tb_2Ti_2O_7$ is in the sextet phase (spin ice phase). Black dashed line shows the classical phase boundary between the doublet and the sextet.

Now, we consider the four lowest states of the crystal field Hamiltonian with all matrix elements including those with the $J^z$ operator in order to find the phase diagram of $Tb_2Ti_2O_7$ within the single tetrahedron approximation. To accomplish this we find the matrix elements of Hamiltonian (5.4) in the four crystal field basis and diagonalize it. The Hamiltonian matrix in this basis is a 256×256 matrix and we specify two sets of states based on their eigenvalues:

- The sixteen lowest states of the system are spread within a 0.5 K band of

energy. These states are made of one singlet, three doublets and three triplets which are the irreducible representation of the tetragonal symmetry. The singlet state is a linear combination of all two-in/two-out states plus a small part of the crystal field excited states. One of the doublets is made of an all-in state plus a small part of the excited states and the time reversal of this state (from now on we use the word doublet for this state unless we mention it explicitly). Other states are made of linear combinations of two-in/two-out, three-in/one-out and three-out/one-in states plus a small contribution from the crystal field excited states.

- The other 256-$2^4$=240 states minus the first set. These states are separated from the first set by a gap of approximately 16 K. Because of the large gap between the second and the first set of states the low energy physics of $Tb_2Ti_2O_7$ is governed by the 16 lowest states.

To find the possible phases we vary the exchange and dipole-dipole couplings and we find that the ground state of this system is either the singlet or the doublet. In Fig. 5.4 we plot the phase diagram of this system in terms of the exchange coupling and as a function of $\frac{1}{\Delta}$ for the given dipole-dipole coupling of $Tb_2Ti_2O_7$ ($\mathcal{D} = 0.0315$ K). The boundary between the singlet and the doublet states can be considered as the quantum variant of the boundary between the two-in/two-out and all-in/all-out states in the Ising phase diagram. This boundary shifts slightly further towards the doublet state compared to the boundary of Fig. 5.3. Therefore, the effect of non-zero $J^z$ matrix elements is not only to make a singlet out of all two-in/two-out states, but also to move the phase boundary upward towards the all-in/all-out state. Based on this phase diagram and the given exchange and dipole-dipole couplings of $Tb_2Ti_2O_7$, $Tb_2Ti_2O_7$ finds itself in the singlet state. Therefore, in the single tetrahedron approximation, $Tb_2Ti_2O_7$ is in the quantum version of the spin ice states. We name this state *quantum spin ice* and this state could be considered as a variational basis state for making the ground state of $Tb_2Ti_2O_7$ on the pyrochlore lattice.

In Fig. 5.5 we plot the three phase boundaries in the same plot to illustrate the movement of the phase boundary due to the virtual crystal field transitions induced

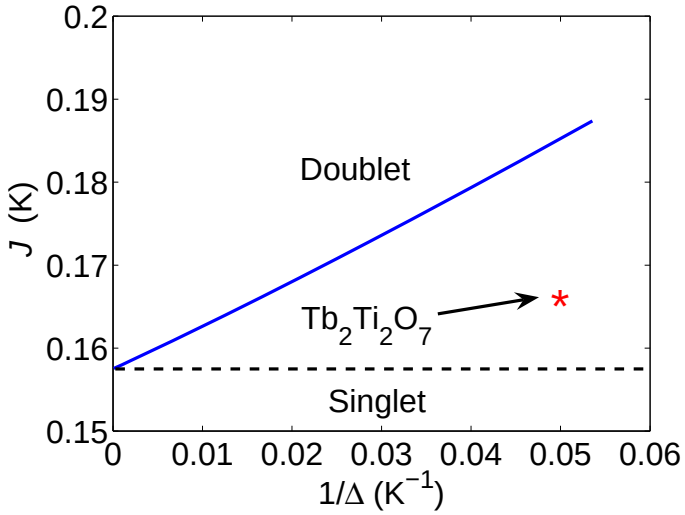


Figure 5.4: Phase diagram of $Tb_2Ti_2O_7$ with four $Tb^{3+}$ lowest crystal field states in the single tetrahedron approximation and with $\mathcal{D}$=0.0315 K. In this phase diagram the exchange interaction is plotted as a function of $\frac{1}{\Delta}$ and $Tb_2Ti_2O_7$ is in the singlet phase which is a linear combinations of all two-in/two-out states plus a small part of excited states. Black dashed line shows the classical phase boundary between the doublet and the sextet.

by the spin interactions. To investigate the change of this boundary in terms of

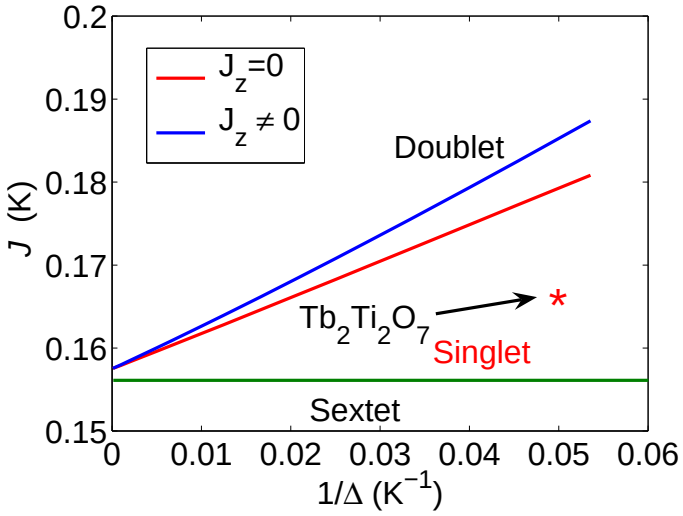


Figure 5.5: Phase diagram of $Tb_2Ti_2O_7$ with four lowest crystal field states in the single tetrahedron approximation and with $\mathcal{D}$=0.0315 K. In this phase diagram the exchange interaction is plotted as a function of $\frac{1}{\Delta}$. Blue and red phase boundaries respectively separate the singlet/doublet and sextet/doublet phase boundaries. In this phase diagram $Tb_2Ti_2O_7$ is in the sextet ($J^z = 0$) or its quantum variant singlet state ($J^z \neq 0$). We use the notation $J^z = 0$ and $J^z \neq 0$ to imply that the $J^z$ matrix elements between the crystal field ground state doublet and first excited crystal field state have been manually set respectively to zero and non-zero.

dipole-dipole coupling we set the exchange coupling to the estimated value for $Tb_2Ti_2O_7$ ($\mathcal{J}$=0.167 K) and plot the dipole-dipole coupling as a function of $\frac{1}{\Delta}$. The result of this calculation in the classical limit and also with zero and non-zero off-diagonal $J^z$ matrix elements is plotted in Fig. 5.6. The quantum effects move the phase boundary downwards, hence a smaller dipole-dipole coupling is needed to keep the system in the sextet state (spin-ice state) or its quantum variant, the singlet state. Here we should add that we calculate this phase boundary using the six lowest crystal field states and we derived a phase boundary with about 0.05% deviation from the phase boundary of Fig 5.5. So we conclude that the effect of higher crystal field states in this calculation is negligible.

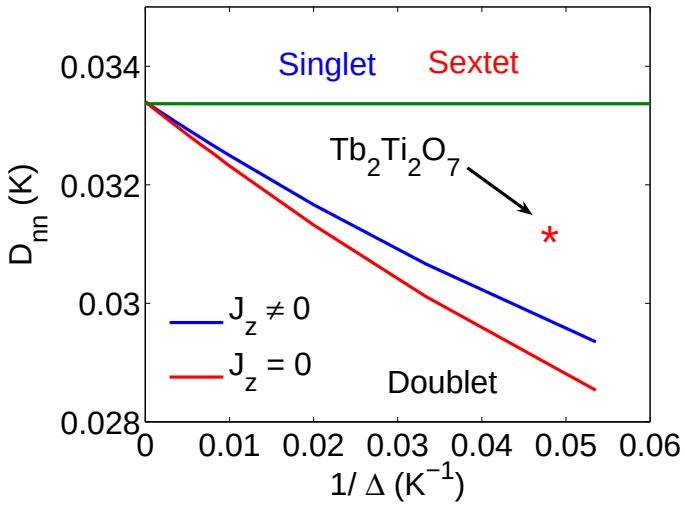


Figure 5.6: Phase diagram of $Tb_2Ti_2O_7$ with four lowest crystal field states in the single tetrahedron approximation and with $J^z$=0 and $J^z \neq 0$ and with $\mathcal{J}$=0.167 K. In this phase diagram the dipole-dipole interaction is plotted as a function of $\frac{1}{\Delta}$. Blue and red phase boundaries are respectively separating the singlet/doublet and sextet/doublet phase boundaries. In this phase diagram $Tb_2Ti_2O_7$ is in the sextet or its quantum variant singlet state.

In the next section we use the effective Hamiltonian results of Chapter 4 to find the phase diagram of $Tb_2Ti_2O_7$ within the single tetrahedron approximation. We also give a physical description for the movement of the phase boundary between the all-in/all-out and two-in/two-out states using the effective Hamiltonian description, and by focusing especially on the quantum Ising term of the effective Hamiltonian.

## 5.3 Phase Diagram of the Effective Hamiltonian in the Single Tetrahedron Approximation

In the previous section we derived the phase boundary of $Tb_2Ti_2O_7$ within the single tetrahedron approximation using a direct (brute force) approach in diagonalizing Eq. (5.4). In this section we calculate the phase boundary of $Tb_2Ti_2O_7$ using the effective Hamiltonian method. We remind the reader of Chapter 4 where an effective Hamiltonian for $Tb_2Ti_2O_7$ was derived by integrating out the effect of excited crystal field states which led to a mapping of the system onto a pseudo-spin 1/2 model.

In analogy with the procedure followed in Section 5.2 we begin the calculations with zero off-diagonal $J^z$ matrix elements and derive an effective Hamiltonian within the single tetrahedron approximation. We recall that the zero off-diagonal $J^z$ matrix elements closes the channel for bi-particle transverse terms in the effective Hamiltonian. As a result, the effective Hamiltonian of the system maps onto a model with strictly local $\langle 111 \rangle$ Ising spins. Hence, the 16 states of the system split into one sextet, one octet and one doublet. The effective interaction between these Ising spins is the sum of the classical interaction term (Section 4.2) between them, the quantum Ising term (Section 4.3), and a small contribution which is the result of the virtual two-ion-excitations effective Hamiltonian (Section 4.4). We remind the reader that the classical term comes from the $PHP$ term of the effective Hamiltonian and the quantum Ising term originates from the virtual single ion excitation of all the third $Tb^{3+}$ ions in the system. Hence, the effective Hamiltonian of the

system is,

$$H_{\text{eff}} = \sum_{a<b} \jmath_{ab} S_a^z S_b^z, \tag{5.5}$$

where $S_a^z$ is the $\langle 111 \rangle$ local Ising spin in sublattice $a$ and $\jmath_{ab}$ is the effective interaction between Ising spins in sublattices $a$ and $b$. In this effective interaction, and for $Tb_2Ti_2O_7$ the quantum Ising term, which is coming from the two nearest neighbors of each pair, is dominant over the classical antiferromagnetic interaction and an Ising interaction which is the local $z$ component of the induced interaction by the virtual two-ion-excitation, making overall an effective $\langle 111 \rangle$ ferromagnetic interaction. It was mentioned in the introduction that the ground state of local Ising spins with a ferromagnetic interaction between them is the sextet state or two-in/two-out state, which is frustrated. Hence, the quantum Ising term changes the sign of the effective $\jmath_{ab}^{\alpha\beta}$ in Eq. (5.5) and makes an originally non-frustrated system in the limit of classical term in the effective interaction($PVP$) "dynamically-frustrated". This result is consistent with the exact result with four states per ion which shows that the ground state of the system is the sextet. In Fig. 5.7 we plot the phase diagram for the effective Hamiltonian for a single tetrahedron in terms of exchange coupling as a function of $\frac{1}{\Delta}$ and for the given dipole-dipole coupling for $Tb_2Ti_2O_7$ ($\mathcal{J}$=0.167 K). To compare, we add the phase boundary without the quantum Ising terms of the Hamiltonian (only the classical Hamiltonian plus two ion excitation effective Hamiltonian) (green curve) and the phase boundary from the exact results of four states per ion to this plot (blue curve). With decreasing $\Delta$, the quantum Ising term becomes larger and the phase boundary moves to the doublet state (Fig. 5.7) which is the indication of increased effective ferromagnetic interaction between Ising spins. These results are in semi-quantitative agreement with the exact results (Fig. 5.7). However, calculating the phase boundary without considering the quantum Ising term, moves the boundary towards the all-in/all-out phase, indicating the increased effective antiferromagnetic interaction between Ising spins. Here, we should mention that the observed deviation between the exact and effective Hamiltonian results are related to the higher order terms in the effective Hamiltonian that we did not include in the calculation of $H_{\text{eff}}$.

It was discussed in Chapter 4 that non-zero off diagonal $J^z$ matrix elements lead

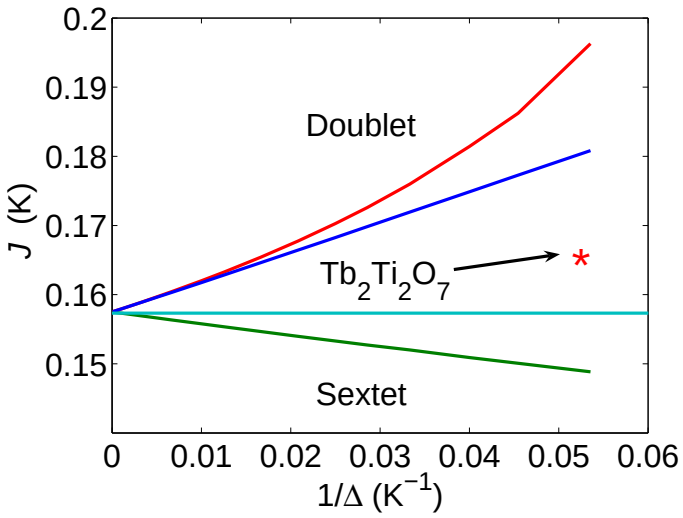


Figure 5.7: Phase diagram of Effective Hamiltonian (red line) of $Tb_2Ti_2O_7$ in the single tetrahedron approximation and with $J^z$=0 and $\mathcal{D}$=0.0315 K. In this phase diagram the exchange interaction is plotted as a function of $\frac{1}{\Delta}$. For comparison the exact results with four states per $Tb^{3+}$ ion (blue line) and effective Hamiltonian result without quantum Ising term (green) are shown in the graph. The line with cyan color shows the classical limit of the phase boundary.

via the interaction between $Tb^{3+}$ ions to induced non-zero matrix elements between the two states of the original crystal field ground state doublet. In the mapping of the two states of the crystal field ground state to the two states of the pseudo-spin 1/2, these non-zero matrix elements are translated into a spin flip mechanism and transverse terms in the effective Hamiltonian. Because of the tetragonal symmetry of the single tetrahedron the single ion transverse terms cancel out each other and consequently the effective Hamiltonian is made of bi-particle terms with the $\langle 111 \rangle$ Ising term as the largest component. Diagonalizing this effective Hamiltonian we find that the 16 states of the effective Hamiltonian are split into one singlet, three doublets and three triplets consistent with the 16 lowest states of the single tetrahedron with four states per $Tb^{3+}$ ion. The singlet state is made of linear

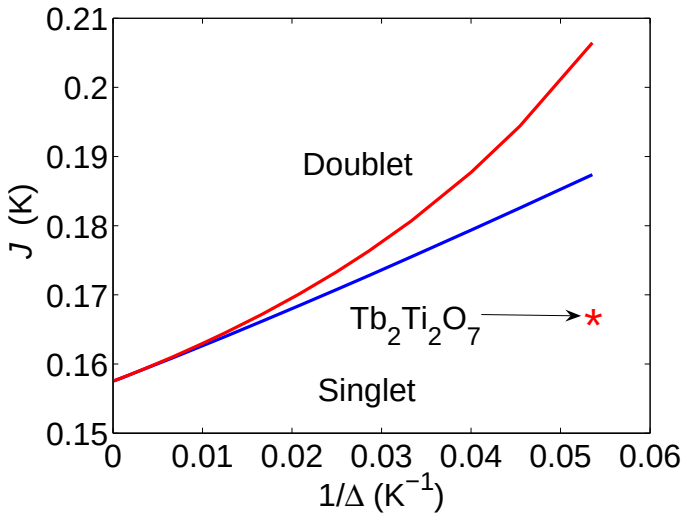


Figure 5.8: Phase diagram of effective Hamiltonian (red line) of $Tb_2Ti_2O_7$ in the single tetrahedron approximation and with $\mathcal{D}$=0.315 K. In this phase diagram the exchange interaction is plotted as a function of $\frac{1}{\Delta}$. For comparison the exact results with four states per $Tb^{3+}$ ion (blue line) is shown in the graph.

combination of all two-in/two-out states and one of the doublets is made of all-in and all-out states. From now by doublet we refer to this state. We calculate the ground state of the effective Hamiltonian for the whole range of dipole-dipole and exchange couplings and we find that the ground state of the effective Hamiltonian

is either the singlet or the doublet. In Fig. 5.8, we plot the phase boundary of the effective Hamiltonian in terms of the exchange coupling as a function of $\frac{1}{\Delta}$. For comparison, we add the exact diagonalization results using the four crystal field states per ion. In the limit of large $\Delta$, both the effective Hamiltonian and exact results are semi-quantitatively the same and, with decreasing $\Delta$, a deviation of the effective Hamiltonian results from the exact results develop. For $\Delta$=18.7 K, which is the gap for $Tb_2Ti_2O_7$, the exact and the effective Hamiltonian results are in a semi-quantitative agreement, with approximately a 10% difference. The discrepancy between the exact and effective Hamiltonian results are from the higher order terms in the construction of the effective Hamiltonian that have not been included in the calculations. In this phase diagram $Tb_2Ti_2O_7$ is in the singlet ground state.

From the results of this section we conclude that the quantum Ising term changes the effective interaction between $Tb^{3+}$ ions from antiferromagnetic to ferromagnetic and dynamically induces frustration. These frustrated states combined together with the bi-particles transverse terms give a singlet ground state which is a linear combination of all these frustrated states (two-in/two-out) with the same weight. Deriving the two-in/two-out-like (spin ice-like) state as the ground state of $Tb_2Ti_2O_7$ raises the question as to why neutron scattering of $Tb_2Ti_2O_7$ has no similarity to the neutron scattering of spin ice systems $Ho_2Ti_2O_7$ and $Dy_2Ti_2O_7$. We address this question in the next Chapter.

## 5.4 Summary

Motivated by the experimental fact that the magnetic correlations in $Tb_2Ti_2O_7$ are of the order of interatomic distances we proposed a single tetrahedron approximation with four $Tb^{3+}$ ions as a good description for $Tb_2Ti_2O_7$. We calculated the phase diagram of $Tb_2Ti_2O_7$ within this approximation using the two states of the crystal field ground state doublet and also four states of the crystal field ground state and first excited state doublets per ion. We showed that in the two states per ion limit, the ground state of the system could be either a sextet or a doublet. The doublet state can be long-range ordered on the pyrochlore lattice and the sextet

state is frustrated. In this two state per ion approximation, $Tb_2Ti_2O_7$ is in the doublet state or all-in/all-out state. When considering the four lowest crystal field states with zero $J^z$ matrix elements between the crystal field ground state and first excited state, we calculated the phase diagram of $Tb_2Ti_2O_7$ and showed that in this limit the ground state of the system is again either a doublet or a sextet. However, the effect of crystal field excited states lead to a movement of the sextet/doublet phase boundary deeper towards the doublet state and puts $Tb_2Ti_2O_7$ in the two-in/two-out (sextet) state. Including the $J^z$ matrix elements in the calculations, we showed that the 16 lowest states decompose into one singlet (which is a linear combination of all two-in/two-out states plus a small part of excited states), three doublets (in which one of the doublet is made of all-in and all-out states plus a small part of excited states) and three triplets. For the whole range of parameters the ground state of the system is either the singlet or the all-in/all-out doublet. In this phase diagram, $Tb_2Ti_2O_7$ is in the singlet state. We also calculated the phase diagram for the effective Hamiltonian in the single tetrahedron approximation. Investigating the behaviour of this phase diagram with and without the quantum Ising term, which comes from the renormalization of the interaction via the intervening third ions, we found that the phase boundary to the doublet state finds its origin from the quantum Ising term. This is the most crucial observation made in this work. To rephrase, the effective interaction between the Ising components of the effective spin $\sigma_i^{z_i}$ and spin $\sigma_j^{z_j}$ changes from being antiferromagnetic and not frustrated to ferromagnetic and frustrated. This effect originates from the virtual crystal field fluctuations of all third ions $k$ which interact with ions $i$ and $j$.

# Chapter 6

# Neutron Scattering of $Tb_2Ti_2O_7$

In Chapter 5 we derived a phase diagram of $Tb_2Ti_2O_7$ within a single tetrahedron approximation and discussed the different phases that may occur as a function of exchange coupling. We also showed that in this approximation, and for a given value of the exchange and dipolar couplings for $Tb_2Ti_2O_7$, this compound is in the quantum spin ice phase which is predominantly made of linear combinations of all spin ice states. However, this prediction of a spin ice like ground state for $Tb_2Ti_2O_7$ would seem to be in contradiction with diffuse neutron scattering results since it is very different from that of the spin ice systems (Chapter 1). In this chapter we address this discrepancy. We use the fact that the magnetic correlations in $Tb_2Ti_2O_7$ are of the order of nearest neighbor and we calculate the diffuse neutron scattering of $Tb_2Ti_2O_7$ in the single tetrahedron approximation. In the first section of this chapter, we give a review of neutron scattering theory and derive an equation for calculating the diffuse neutron scattering in terms of the eigenvalues and eigenfunctions of a system. In the second section, we calculate the diffuse neutron scattering of $Tb_2Ti_2O_7$ with two, four and six lowest states (the six lowest crystal field states are the ground state, first excited state doublets and second and third excited state singlets) of the crystal field states per ion. In this section we show that considering the four and six lowest crystal field states does not quantitatively change the neutron scattering pattern and, hence the crystal field ground state and first excited state doublets are enough to describe the neutron scattering of $Tb_2Ti_2O_7$ within the

single tetrahedron approximation. In the third section we give a falsifiable experiment based on the diffuse neutron scattering in (hh2) direction to confirm whether $Tb_2Ti_2O_7$ indeed posses a quantum spin ice ground state. This calculation shows that in the quantum spin ice state the highest diffuse neutron scattering intensity is at (002), whereas in the doublet state, the highest intensity moves from (002) to two peaks at $(\delta\delta 2)$ and $(\bar{\delta}\bar{\delta}2)$.

## 6.1 Diffuse Neutron Scattering

Neutron scattering is a very powerful tool for investigating the magnetic properties of a solid at an atomic scale. On one hand, neutrons are neutral and they only interact with the environment via the magnetic dipole-dipole interaction, and on the other hand, their interaction with the environment is so weak that they do not disturb the magnetic system significantly. Hence, neutrons can easily penetrate into a magnetic material and are scattered by magnetic moments without disturbing the magnetic structure of the system. These scattered neutrons contain enough information to give all the magnetic properties of the system. In a long range ordered phase, elastically scattered neutrons give magnetic Bragg peaks which reveal the magnetic structure of the system while the inelastically scattered neutrons give information about the dispersion relation of the magnetic excitations. Moreover, the magnetic scattering cross section is related to the time-dependent pair-correlation function and is related to the generalized susceptibility via the fluctuation-dissipation theorem. In this section we give a review of neutron scattering theory and derive a formula for calculating the diffuse neutron scattering in terms of the eigenvalues and eigenfunctions of a system. We use this formula in the next section to calculate the neutron scattering of $Tb_2Ti_2O_7$ within the single tetrahedron approximation.

For a system of identical magnetic ions, the differential neutron scattering cross section is given by [61],

$$\frac{d^2\sigma}{dEd\Omega} = N\frac{k'}{k}(\frac{\hbar\gamma e^2}{mc^2})^2 e^{-2W(\kappa)}|\frac{1}{2}gF(\kappa)|^2 \sum_{\alpha\beta}(\delta_{\alpha\beta} - \hat{\kappa}_\alpha\hat{\kappa}_\beta)S^{\alpha\beta}(\kappa,\omega), \qquad (6.1)$$

where $N$ is the number of magnetic ions, $k$ and $k'$ are unit wave vectors of ongoing and outgoing neutrons, $\hbar$ is the Plank's constant divided by $2\pi$, $\gamma$ is the gyromagnetic ratio of neutrons, $e^2/mc^2$=2.82 fm is the classical electron radius, $W(\kappa)$ is the Debye-Waller factor, $F(\kappa)$ is the magnetic form factor for $Tb^{3+}$ ion, $\kappa_\alpha$ is the scattering vector, $\hat{\kappa}_\alpha$ is the $\alpha$ component of the unit vector of $\kappa_\alpha$, $\omega$ is energy transfer divided by $\hbar$. $S^{\alpha\beta}$ is the Van Hove scattering function defined as [61],

$$S^{\alpha\beta}(\kappa,\omega) = \frac{1}{2\pi\hbar}\int_{-\infty}^{\infty} dt e^{i\omega t}\frac{1}{N}\sum_{jj\prime} e^{-i\kappa.(\mathbf{R}_j-\mathbf{R}_{j'})}\langle J_j^\alpha(t)J_{j'}^\beta(0)\rangle, \tag{6.2}$$

where $J_j^\alpha$ is the $\alpha$ component of the angular momentum of ion $j$ and the sum over $j$ and $j'$ are over all $Tb^{3+}$ ions in the system. Adding and subtracting $\langle J_j^\alpha\rangle\langle J_{j'}^\beta\rangle$, the scattering function can be written as the sum of the elastic and inelastic contributions as,

$$S^{\alpha\beta}(\kappa,\omega) = S^{\alpha\beta}(\kappa) + S^{\alpha\beta}_{\text{inelastic}}(\kappa,\omega), \tag{6.3}$$

where the elastic component is

$$S^{\alpha\beta}(\kappa) = \delta(\hbar\omega)\frac{1}{N}\sum_{jj'}\langle J_{j\alpha}\rangle\langle J_{j'\beta}\rangle e^{-i\kappa.(\mathbf{R}_j-\mathbf{R}'_j)} . \tag{6.4a}$$

$$S^{\alpha\beta}_{\text{inelastic}}(\kappa,\omega) = \frac{1}{\pi}\frac{1}{1-e^{-\beta\hbar\omega}}\chi^{''}_{\alpha\beta}(\kappa,\omega) , \tag{6.4b}$$

where $\omega$ is the energy transfer divided by $\hbar$ and $\chi^{''}_{\alpha\beta}(\kappa,\omega)$ is the imaginary part of the susceptibility defined as,

$$\chi^{''}_{\alpha\beta} = \pi \sum_{\gamma\gamma'}^{E_\gamma\neq E_{\gamma'}} \langle\gamma|J_j^\alpha|\gamma'\rangle\langle\gamma'|J_{j'}^\beta|\gamma\rangle(n_\gamma - n_{\gamma'}) \delta(E_\gamma - E_{\gamma'} - \hbar\omega)e^{-i\kappa.(\mathbf{R}_j-\mathbf{R}_{j'})}. \tag{6.5}$$

where $|\gamma\rangle$ and $|\gamma'\rangle$ are the eigenstates of the system and $n_\gamma = \exp(\frac{E_\gamma}{k_B T})$ is the Boltzmann population of state $|\gamma\rangle$ at temperature $T$.

In a diffuse neutron scattering experiment, the outgoing neutrons from the sample are counted within a narrow range of energy which we call the window of energy. As a result, the inelastic contribution from the lowest states of the system which

are in this energy window has to be included in the total scattering. To accomplish this, we calculate the diffuse neutron scattering by integrating over $S^{\alpha\beta}_{\text{inelastic}}$ in the energy window of the experiment $w$,

$$S_{\text{diffuse}} = \int_{E_0}^{E_0+w} S^{\alpha\beta}_{\text{inelastic}}(\kappa,\omega)d\omega = \int \frac{1}{\pi}\frac{1}{1-e^{-\beta\hbar\omega}}\chi^{''}_{\alpha\beta}(\kappa,\omega). \quad (6.6)$$

The imaginary part of the susceptibility $\chi^{''}_{\alpha\beta}(\kappa,\omega)$ can be written down as follow:

$$\chi^{''}_{\alpha\beta} = \sum_{jj'}\pi \sum_{\gamma\gamma'}^{E_\gamma \neq E_{\gamma'}} \langle\gamma|J^{\alpha}_{j}|\gamma'\rangle\langle\gamma'|J^{\beta}_{j'}|\gamma\rangle e^{\frac{-E_\gamma}{k_BT}}(1-\exp^{-(\frac{E_{\gamma'}-E_\gamma}{k_BT})}) \\ \delta(E_\gamma - E_{\gamma'} - \hbar\omega)e^{-i\kappa.(\mathbf{R}_j-\mathbf{R}_{j'})}. \quad (6.7)$$

Substituting this equation into Eq. (6.6) and taking the integral we derive the diffuse scattering function as,

$$S^{\alpha\beta}_{\text{diffuse}} = \sum_{jj'}\sum_{\gamma,\gamma'}\langle\gamma|J^{\alpha}_{j}|\gamma'\rangle\langle\gamma'|J^{\beta}_{j'}|\gamma\rangle n_\gamma e^{-i\kappa.(\mathbf{R}_j-\mathbf{R}_{j'})}. \quad (6.8)$$

where $|\gamma\rangle$ and $|\gamma'\rangle$ states are in the energy window of the experiment and we have both elastic $E_\gamma = E_{\gamma'}$ and inelastic $E_\gamma \neq E_{\gamma'}$ components. This is a general formula for calculating the diffuse neutron scattering in terms of the eigenvalues and eigenfunctions of a system with a narrow band of energy levels within the energy window of the experiment. In the next section, we apply this formalism to $Tb_2Ti_2O_7$ to calculate the diffuse neutron scattering for this compound.

## 6.2 Diffuse Neutron Scattering of $Tb_2Ti_2O_7$

In this section we calculate the diffuse neutron scattering for $Tb_2Ti_2O_7$ within the single tetrahedron approximation and clarify the effect of excited crystal field states on the magnetic correlations of $Tb_2Ti_2O_7$. In Fig. 6.1 we show the experimental diffuse neutron scattering of $Tb_2Ti_2O_7$ at 9 K [43]. The diffuse neutron scattering of $Tb_2Ti_2O_7$ at 60 mK gives the same pattern as the 9 K result [28]. As a first approximation, we use the crystal field ground state doublet to calculate the neutron scattering of $Tb_2Ti_2O_7$. From Eq. (6.8) the scattering function of some

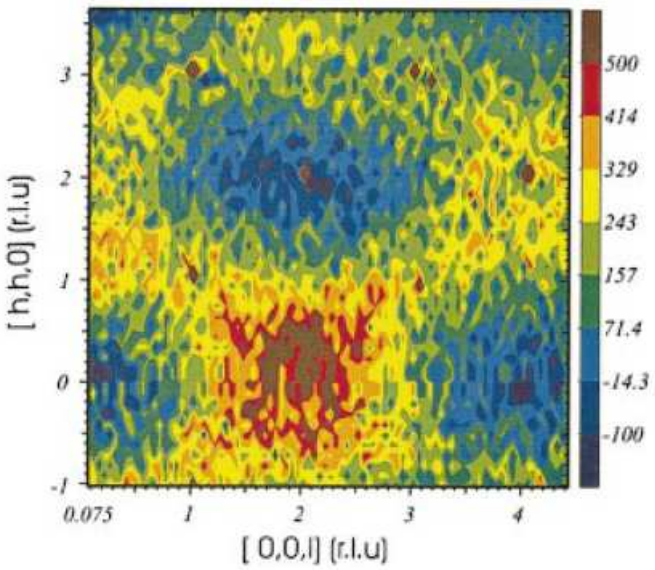


Figure 6.1: Experimental diffuse neutron scattering of $Tb_2Ti_2O_7$ at 9 K. The observed checkerboard pattern with highest intensity at (002) makes a unique scattering pattern for $Tb_2Ti_2O_7$ [43].

identical magnetic ions in terms of the eigenvalues and the eigenstates of the system is given by

$$S^{\alpha\beta} = \sum_{ab}\sum_{\gamma,\gamma'}\langle\gamma|J_a^\alpha|\gamma'\rangle\langle\gamma'|J_b^\beta|\gamma\rangle n_\gamma e^{-i\kappa.(\mathbf{R}_a-\mathbf{R}_b)} \tag{6.9}$$

where $|\gamma\rangle$ and $|\gamma'\rangle$ are eigenstates of the system, $J_a^\alpha$ is the $\alpha$ component of the total angular momentum of ion at sublattice $a$, $n_\gamma$ is the Boltzmann factor equal to $\exp(\frac{-E_\gamma}{k_B T})$ where $E_\gamma$ is the energy of state $|\gamma\rangle$, $k_B$ is the Boltzmann constant, $T$ is the temperature, the sum on $|\gamma\rangle$ and $|\gamma'\rangle$ are over eigenstates of the system with energy within the energy window of the experiment, and the sum on $a$ and $a'$ is over the four sublattices of a single tetrahedron. The eigenstates of the Hamiltonian, made of one doublet, one sextet and one octet, were discussed in Chapter 5. Using this formula and the given exchange and dipole-dipole couplings for $Tb_2Ti_2O_7$ ($\mathcal{D}$=0.0315 K and $\mathcal{J}$=0.167 K), we calculate the scattering function of four $Tb^{3+}$ ions on a single tetrahedron using the crystal field ground state doublet for each $Tb^{3+}$ ion. The result of this calculation is shown in Fig. 6.2. This scattering pattern does not

capture any feature of the diffuse neutron scattering of $Tb_2Ti_2O_7$ and instead, it is similar to the neutron scattering pattern of $\langle 111 \rangle$ Ising spin systems at high temperatures. This is because, in the classical limit, there is no transverse term in the effective Hamiltonian and two states of the crystal field Hamiltonian make local $\langle 111 \rangle$ Ising spins similar to spin ice systems. This pattern, when compared with the experimental pattern of $Tb_2Ti_2O_7$ (Fig. 6.1) [43] shows no consistency between the theoretical results and experimental data. Hence, considering the two states of the crystal field ground state or, in other word, assuming the $\langle 111 \rangle$ Ising assumption is not adequate to describe the experimental data from diffuse neutron scattering of $Tb_2Ti_2O_7$.

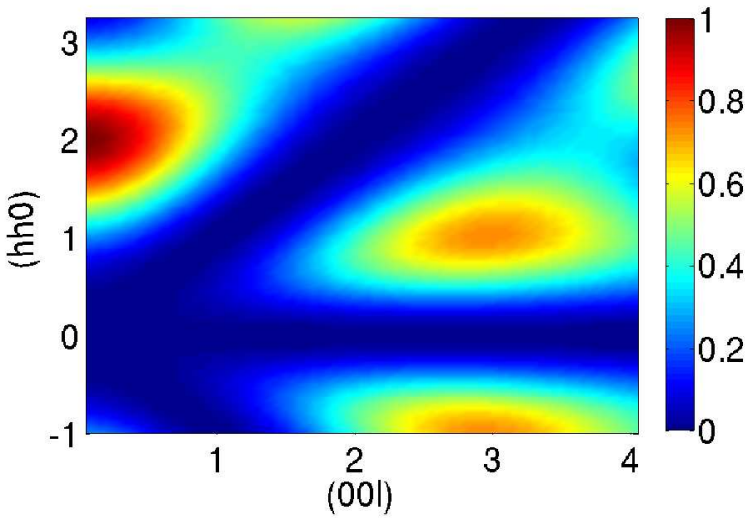


Figure 6.2: Calculated diffuse neutron scattering using the two states of the crystal field ground state of $Tb_2Ti_2O_7$ in the single tetrahedron approximation at T=9 K. This neutron scattering pattern is not compatible with the exact results and it is similar to neutron scattering pattern of spin ice system at high temperatures.

We discussed in Chapter 5 the fact that virtual excitations to the first excited crystal field states play an essential role in displacing the phase boundary to the all-in/all-out state. We also mentioned that zero $J^z$ matrix elements between the crystal field ground state and first excited state eliminates the channel for inducing

matrix elements between the two states of the crystal field ground state doublet. We first use the four states of the crystal field Hamiltonian considering zero $J^z$ matrix elements to calculate the scattering function of $Tb_2Ti_2O_7$ within the single tetrahedron approximation. In Section 5.2 we calculated the eigenvalues, the eigenstates, and the phase diagram of this problem. We use these eigenvalues and eigenstates to calculate the scattering function in Eq. (6.9). In contrast to the classical approximation above, we incorporate the $J^x$ and $J^y$ matrix elements between the crystal field ground state and first excited state. These matrix elements give inelastic scattering among states that fall within the energy window of the experiment (diffuse neutron scattering).

To compare our diffuse neutron scattering results with the experimental diffuse neutron scattering we need to find the energy window of the experiment. In the diffuse neutron scattering results which were obtained by Gardner *et. al.* [43], the energy window of the experiment is about 4.2 K. Hence, all the states of the system with energy lower than 4.2 K contribute to the diffuse neutron scattering intensity pattern. The 16 lowest energy states of the system satisfy this condition and their effects have to be included in the calculation. Using Eq. (6.9) and the 16 lowest eigenvalues and eigenstates obtained in the last section, we calculate the scattering function in the single tetrahedron approximation at $T$=9 K. The result of this calculation is shown in Fig. 6.3. The calculated scattering pattern is dramatically different from the classical limit pattern (Fig. 6.2). The highest region of intensity moves from (000) to a region around (002) with the highest intensity splitted into two symmetric peaks at ($\bar{\text{h}}\bar{\text{h}}$2) and (hh2). This pattern has some similarities with the diffuse neutron scattering pattern of $Tb_2Ti_2O_7$ (Fig. 6.1), with the difference that the highest intensity in the experimental results is at (002). The observed diffuse scattering in this pattern is related to the non-zero $J^x$ and $J^y$ matrix elements between the crystal field ground state and first excited state. These matrix elements give transitions between the 16 lowest states of the single tetrahedron. However, because of the zero $J^z$ matrix elements between the crystal field ground state and first excited state, these 16 states are divided into two sets each with 8 states and no matrix elements between these two sets of states. From this result we conclude that although the produced neutron scattering pattern with four lowest

crystal field states has some similarities with the experimental pattern, it does not capture all the features like highest intensity at (002). Hence, it seems that considering the non-zero matrix elements is indeed necessary in understanding the diffuse neutron scattering of $Tb_2Ti_2O_7$. A similar conclusion was previously reached on the basis of mean-field treatment of an anisotropic spin model for $Tb_2Ti_2O_7$ [54] as well as a random phase approximation (RPA) calculation [55].

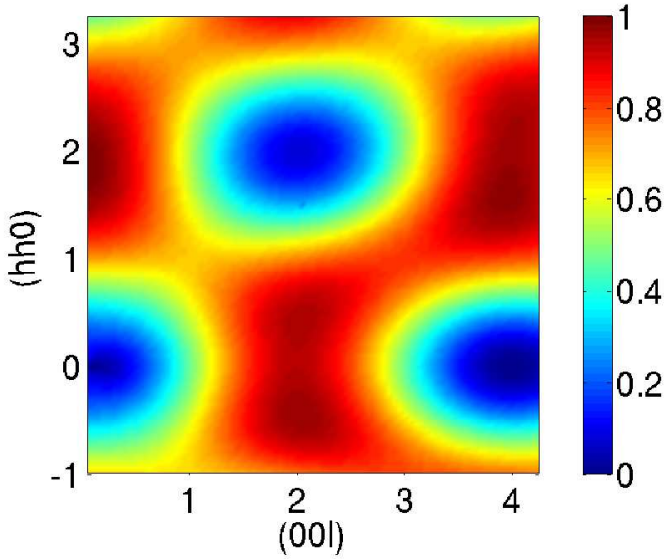


Figure 6.3: Calculated diffuse neutron scattering with four lowest states of the crystal field states of $Tb_2Ti_2O_7$ and zero off-diagonal $J^z$ matrix elements in the single tetrahedron approximation ($\mathcal{D}$=0.0315 K and $\mathcal{J}$=0.167 K). This neutron scattering pattern is similar to the experimental neutron scattering with the difference that the highest intensity is at (hh2) and ($\bar{\text{h}}\bar{\text{h}}$2) instead of (002).

Following the discussion in previous paragraph, we now consider the four lowest crystal field states of $Tb^{3+}$ and calculate the scattering function of $Tb_2Ti_2O_7$ in the single tetrahedron approximation, but now considering all the $J^x$, $J^y$ and $J^z$ matrix elements between the states. We use the eigenvalues and the eigenfunctions of the single tetrahedron with four states per ion to calculate the scattering function. It was discussed in Section 5.1 that the 16 lowest states of the system make a narrow band (0.5 K), which is in the energy window of the experiment, and the

rest of the states are separated by a 16 K gap. Substituting these eigenstates and eigenvalues into Eq. (6.9) we calculate the diffuse neutron scattering and the result of this calculation is shown in Fig. 6.4. This scattering function captures all of the features of the experimental results including highest intensity at (002) and lowest intensity at (000). Comparing this figure with Fig. 6.3 one sees that the effect

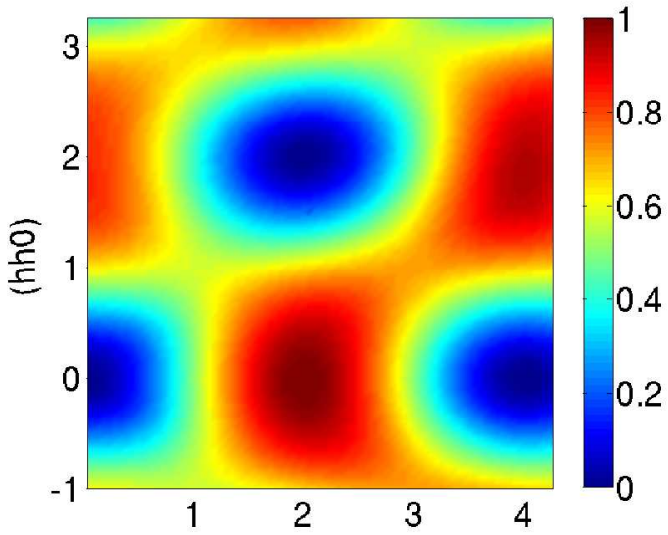


Figure 6.4: Calculated diffuse neutron scattering with four lowest states of the crystal field states of $Tb_2Ti_2O_7$ and non-zero $J^z$ matrix elements between the ground state doublet and first excited state doublet in the single tetrahedron approximation ($\mathcal{D}$=0.0315 K and $\mathcal{J}$=0.167 K).

of non-zero $J^z$ matrix elements is to make the scattering pattern more symmetric. This can be seen most clearly by the two highest intensity peaks in Fig. 6.3 at (hh2) and ($\bar{\text{h}}\bar{\text{h}}$2) combined into a single maximum at (002) in Fig 6.4. The calculated line scans of the scattering function in (00h), (hh0) and (hhh) directions are plotted in Fig. 6.5 and, for comparison, the experimental line scans of $Tb_2Ti_2O_7$ have been included. The theoretical line scans are scaled by the ratio between the highest experimental to the highest (global maximum) theoretical intensity peaks at (002). These results are in semi-quantitative agreement with experimental results of Fig. 6.1. If we remove the elastic part of the scattering function, namely consider Eq.

(6.9) and apply the condition $E_\gamma \neq E'_\gamma$, and only plot the line scan of the diffuse scattering we get the more quantitative agreement between the theoretical and the experimental results. The result of these calculations is plotted in Fig. 6.6. Notice that in this calculation one scaling parameter has been used while, in the single tetrahedron model of Reference [43], three scaling factors were used for each direction. From this discussion we conclude that there may be a mechanism that makes the elastic scattering of $Tb_2Ti_2O_7$ weak. The source of this mechanism can be small terms in the Hamiltonian that lift the degeneracy and make the elastic response zero. In the next section we use the diffuse neutron scattering result in the (002) direction to propose an experiment to verify the quantum spin ice phase in $Tb_2Ti_2O_7$.

We should mention that by adding anisotropic exchange and Dzyaloshinskii-Moriya (DM) interactions with $\frac{1}{10}$ of the strength of the isotropic exchange we obtained a neutron scattering pattern which has much less symmetry than what is obtained using an isotropic exchange interaction. This symmetry cannot be recovered by considering the long-range dipole-dipole interactions and magnetic correlations beyond the first nearest neighbors. Hence, we tentatively conclude that the effects of other interactions on the magnetic properties of $Tb_2Ti_2O_7$ are small. However, this is a question that requires further investigation.

## 6.3 Possible Experimental Realization of Quantum Spin Ice

In this Section we propose an experiment based on the scattering of neutrons along the (hh2) direction that can be used to verify the proposed quantum spin ice ground state in $Tb_2Ti_2O_7$. In this calculation we use the four lowest crystal field states and calculate the diffuse neutron scattering as was explained in Section 6.1. In Fig. 6.7(a) we plot the scattering function as a function of exchange coupling and for the given dipole-dipole coupling for $Tb_2Ti_2O_7$ in the single tetrahedron approximation at 40 mK. Comparing this result with the phase diagram of Fig. 5.4 we see that at the transition point ($\mathcal{J}= 0.187$ K) from the singlet state (quantum

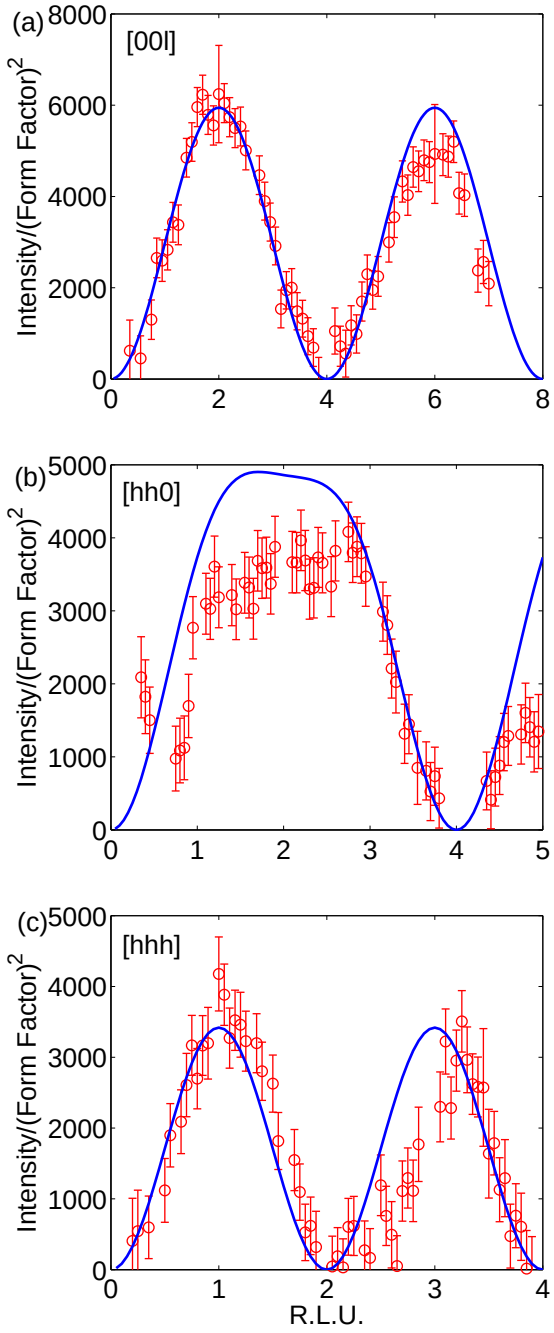


Figure 6.5: Calculated line scan of diffuse scattering function in the symmetric directions [00l], [hh0] and [hhh] (blue lines) at T=4 K. The experimental data of Intensity/(Form factor)$^2$ with their error bars are added to the plot for comparison (red data) [43].

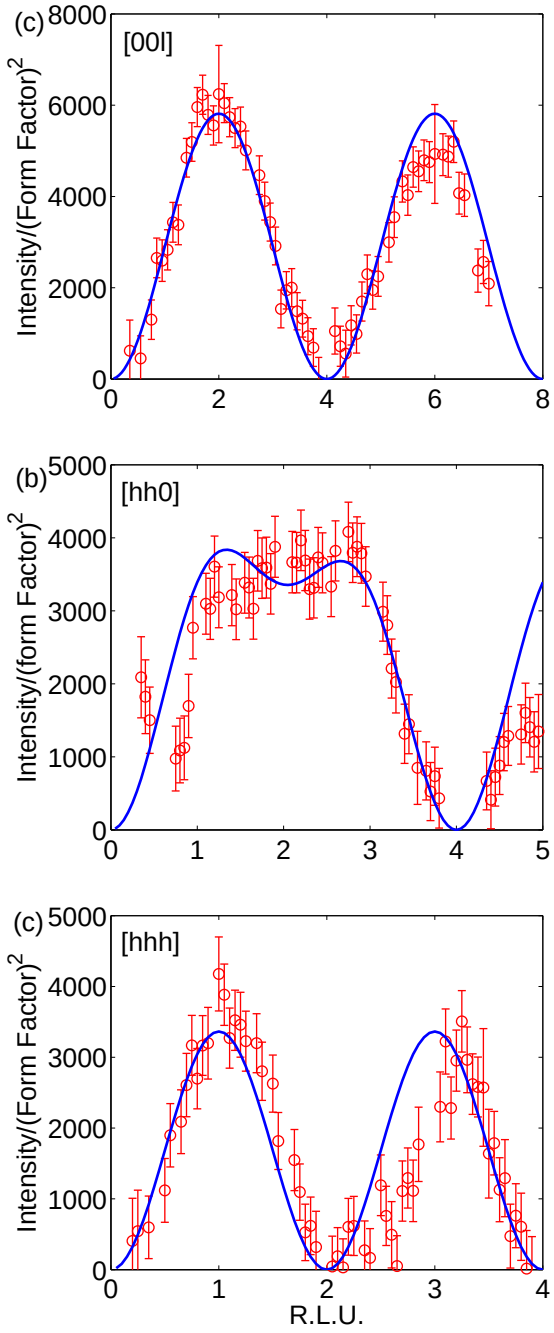


Figure 6.6: Calculated line scan of the diffuse scattering function without elastic term in the symmetric directions [00l], [hh0] and [hhh] (blue lines) at T=4 K. The experimental data of Intensity/(Form factor)$^2$ with their error bars are added to the plot for comparison (red data) [43].

spin ice phase) to the doublet state (all-in/all-out phase) the highest intensity at (002) splits into two highest intensity branches at ($\delta\delta 2$) and ($\bar{\delta}\bar{\delta}2$). This suggests a verifiable experimental probe for investigating the quantum spin ice phase in $Tb_2Ti_2O_7$. In Fig. 6.7(b) we plot the same graph but at the higher temperature, $T$=400 mK. Again, we observe a bifurcation of highest intensity at (002), but this time because of the thermal effects, the splitting is not sharp at the phase boundary. In other words, close to the phase boundary, the doublet and the singlet states are very close and the thermal population of both states are the same at 400 mK. Hence, we do not have a sharp splitting of the intensity at (002), at the phase boundary. Hence, a line scan of the neutron scattering intensity at the lowest possible temperature along [hh2] direction could be used to ascertain whether the low-temperature state of $Tb_2Ti_2O_7$ is a quantum spin ice. The presence of local intensity maxima away from (002) would tend to rule out, at least within the discussion presented in Chapter 5, the existence of a spin-ice like state at low temperature in this material.

## 6.4 Summary

In this Chapter we used the experimental fact that the magnetic correlations in $Tb_2Ti_2O_7$ are to the order of nearest neighbor distance and introduced the single independent tetrahedron approximation with four $Tb^{3+}$ ions per tetrahedron as a good approximation for $Tb_2Ti_2O_7$. Using the eigenstates and eigenvalues of the single tetrahedron with two and four states per ion, we calculated the diffuse neutron scattering of $Tb_2Ti_2O_7$. In the limit of two states per ion we showed that the scattering function is identical to that of $\langle 111 \rangle$ Ising spins on the pyrochlore lattice at high temperatures. In the limit of four states per ion and with zero $J^z$ matrix elements between the crystal field ground state and first excited state, the scattering function is similar to the experimental results with exception that the highest intensity appears at the (hh2) and ($\bar{\text{h}}\bar{\text{h}}2$) and not at (002). Using the four states per ion we derived a scattering pattern which captures all the features of the experimental results. We also proposed an experiment based on the scattering function at (hh2) direction that can be used to verify the spin ice state in $Tb_2Ti_2O_7$.

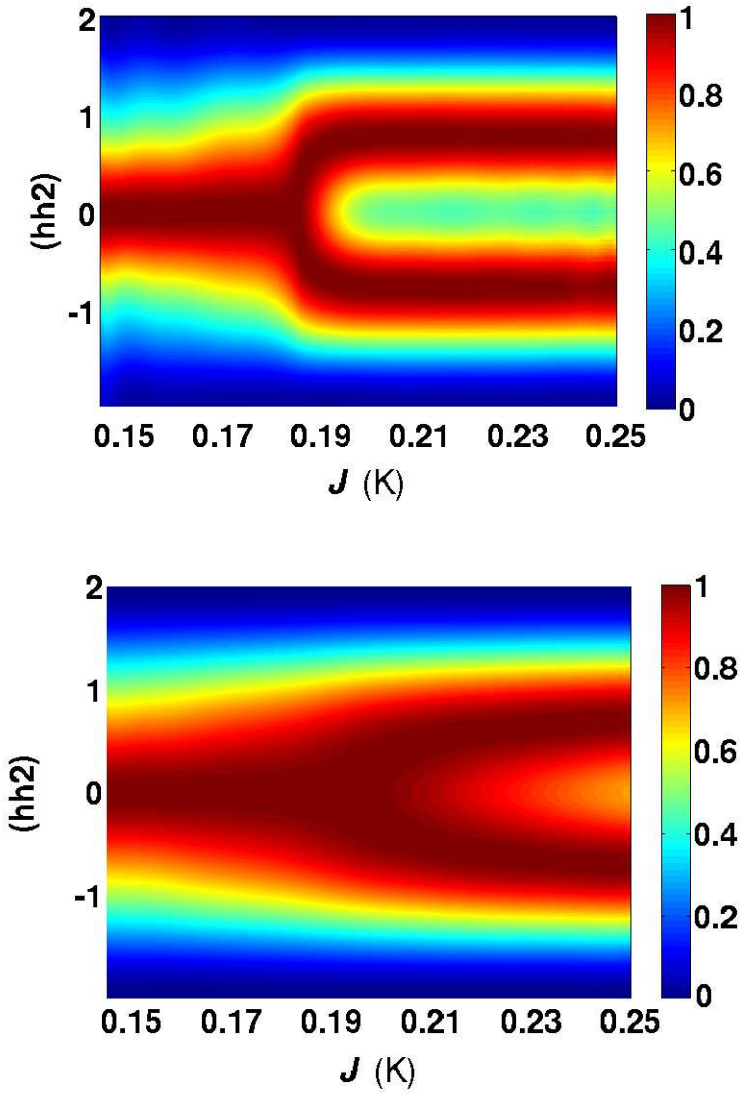


Figure 6.7: Calculated line scan of scattering function along the (hh2) direction at 40 mK (top figure) and 400 mK (down figure). The splitting of the (hh2) line scan arises at the phase boundary between the singlet and doublet states.

# Chapter 7

# The Ground State of $Tb_2Ti_2O_7$ in the Classical Limit

In Chapter 4 we derived an effective spin Hamiltonian for $Tb_2Ti_2O_7$ and found the quantum ground state and related phases of $Tb_2Ti_2O_7$ within a single tetrahedron approximation (Chapter 5). However, in this approximation, the effects of long-range interactions such as dipole-dipole, E-D and D-D (Section 4.3) interactions and also the generated second and third nearest neighbors effective exchange interactions were not taken into account. Hence, the next question that arises is" what is the ground state of $Tb_2Ti_2O_7$ in the presence of these interactions in the thermodynamic limit?". In this chapter we explore these questions in the classical limit in which, we treat the effective spin 1/2 operators as classical rotors. This ground state could then be used in a subsequent $1/S$ calculation to test its stability and also to find the quantum fluctuations around this ground state. This could be done, for example, by following the approach used in Ref. [65]. In the first section of this chapter we apply the Ewald method to the E-D interaction to derive the proper interaction in a simulation box with periodic boundary conditions. In the second section we show that the D-D part of the interaction is at least three times smaller than the E-D part at long distances and hence, we neglect the D-D interaction in comparison to the E-D interaction for long distances. More work would be needed to investigate the consequences of this work. In the third section we calculate the

classical ground state of $Tb_2Ti_2O_7$ within a single cubic unit cell with 16 spins.

## 7.1 Ewald Method for E-D Interaction

In this section we apply periodic boundary condition to the long-range E-D interaction for spins inside a simulation box. However, because of, firstly, the slow convergence nature of the E-D interaction $\frac{1}{r_{ij}{}^3}$ (Section 4.3.1.), and secondly, the sum over the mirror images of any spin inside the box, applying the periodic boundary condition is not trivial.

We use the well-known Ewald method to implement the periodic boundary for the dipole-dipole interaction. This method has been extensively used to calculate the dipole-dipole interaction for the pyrochlore lattice [32,54]. We use the numerical data of spin ice systems for dipole-dipole interaction provided by Taras Yavors'kii to derive the E-D interaction in a simulation box with periodic boundary condition. However, the E-D interaction is not exactly dipolar like. The reason for this is the sum over the third $Tb^{3+}$ ions in the system. Hence we apply a trick to sum over the E-D part of the effective Hamiltonian using the Ewald data of the classical dipole-dipole interaction.

The E-D part of the effective Hamiltonian for a pair of spins 1 and 2 inside the simulation box reads,

$$\begin{aligned} H_{\text{eff}}^{\text{E-D}} &= \sum_{\langle k,c\rangle}\sum_{n} \mathcal{J}\, u_a^{\alpha_1 z} u_c^{\alpha_2\gamma_1} u_b^{\beta_1 z} u_c^{\beta_1\gamma_2} \mathcal{D}_{ik;ac}^{\alpha_1\alpha_2} \\ &\quad \langle\phi_{k,0}^{(l_k)}|J_k^{\gamma_1}|\frac{|\phi_{k,n}^{(p_k)}\rangle\langle\phi_{k,n}^{(p_k)}|}{(E_k^0 - E_k^n)}|\tilde{J}_k^{\gamma_2}|\phi_{k,0}^{(l_k)}\rangle \sigma_{i,a}^z \otimes \sigma_{j,b}^z + Per(i \leftrightarrow j)\ , \end{aligned} \quad (7.1)$$

where $\mathcal{J}$ is the exchange coupling, $\mathcal{D}$ is the dipole-dipole coupling, $\tilde{J}_k^{\alpha}$ is the $\alpha$ component of the angular momentum, $\phi_{k,n}^{p_k}$ is the $p_k$ state of the $n^{th}$ crystal field state, $u_a^{\alpha\beta}$ is the $\alpha\beta$ component of the transformation matrix for sublattice $a$ and the lattice sum is over the six nearest neighbors of spins 1 and 2. To apply the periodic boundary condition we sum over all images of both spins 1 and 2, and the

effective Hamiltonian in the simulation box can be written down as,

$$H_{\text{eff}}^{\text{E-D}} = \sum_{i1,i2}{}' \sum_{\langle k,c\rangle} \sum_{n} \mathcal{J} u_a^{\alpha_1 z} u_c^{\alpha_2 \gamma_1} u_b^{\beta_1 z} u_c^{\beta_1 \gamma_2} \mathcal{D}_{1ik;ac}^{\alpha_{i1}\alpha_{i2}} \langle \phi_{k,0}^{(l_k)} | \tilde{J}_k^{\gamma_1} | \frac{|\phi_{k,n}^{(p_k)}\rangle\langle\phi_{k,n}^{(p_k)}|}{(E_k^0 - E_k^n)} | J_k^{\gamma_2} | \phi_{k,0}^{(l_k)} \rangle \sigma_{i,a}^z \otimes \sigma_{j,b}^z + Per(i \leftrightarrow j) \ , \quad (7.2)$$

where the sum over $i1$ and $i2$ is a sum over spins 1, 2 and all the images of spins 1 and 2 and prime shows the exclusion of self energy term from this summation. Sum over $i2$ is a finite sum and it is limited to the first nearest neighbor, hence it is easy to calculate. However, because of the long-range nature of the dipole-dipole interaction the sum over $i1$ is an infinite sum and we calculate this sum using Ewald method. In another word, Eq. 7.2 is linear in terms of the dipole-dipole interaction and hence, we can change the order of sums and use the Ewald method. After doing these sums, the E-D part of the interaction for spins 1 and 2 in the simulation box reads,

$$H_{\text{eff}}^{\text{E-D}} = \sum_{\langle k,c\rangle} \sum_{n} \mathcal{J} u_a^{\alpha_1 z} u_c^{\alpha_2 \gamma_1} u_b^{\beta_1 z} u_c^{\beta_1 \gamma_2} \mathcal{D}_{1k;ac}^{\text{Ewald};\alpha_1\alpha_k} \langle \phi_{k,0}^{(l_k)} | \tilde{J}_k^{\gamma_1} | \frac{|\phi_{k,n}^{(p_k)}\rangle\langle\phi_{k,n}^{(p_k)}|}{(E_k^0 - E_k^n)} | \tilde{J}_k^{\gamma_2} | \phi_{k,0}^{(l_k)} \rangle \sigma_{i,a}^z \otimes \sigma_{j,b}^z + Per(i \leftrightarrow j) \ , \quad (7.3)$$

where $\mathcal{D}_{1k;ac}^{\text{Ewald};\alpha_1\alpha_k}$ is the Ewald coupling between spin $1, a$ and $k, c$ . From this expression we can easily calculate the E-D part of the effective Hamiltonian using the known results of Ewald sum for the classical dipole-dipole interaction.

In this section we calculated the E-D interaction in a simulation box with the periodic boundary condition. In the next section we calculate the D-D part of the effective Hamiltonian in a simulation box with periodic boundary condition.

## 7.2 D-D Interaction in a Simulation Box

To complete our discussion about applying the periodic boundary condition on the long-range interactions, in this section we calculate the D-D part of the

interaction in a simulation box. The D-D part of the interaction reads,

$$H_{\text{eff}}^{\text{D-D}} = |\langle J^z\rangle|^2 \sum_k \sum_n u_i^{\alpha_1 z} u_k^{\alpha_2 \gamma_1} u_j^{\beta_1 z} u_k^{\beta_2 \gamma_2} \mathcal{D}_{ik}^{\alpha_1 \alpha_2} \mathcal{D}_{jk}^{\beta_1 \beta_2} \langle \phi_{k,0}^{(l_k)} | \tilde{J}_k^{\gamma_1} | \frac{|\phi_{k,n}^{(p_k)}\rangle\langle\phi_{k,n}^{(p_k)}|}{(E_k^0 - E_k^n)} | \tilde{J}_k^{\gamma_2} | \phi_{k,0}^{(l_k)} \rangle \sigma_i^z \otimes \sigma_j^z \quad (7.4)$$

Because of the infinite sum over all the spins in the system and the slow convergence of this interaction, $\frac{1}{r^3}$, an exact calculation of this interaction is unfeasible. We should mention that we can not substitute the dipole-dipole couplings in Eq. (7.4) with the Ewald sum, because the reason for this is that this expression is not linear in terms of the dipole-dipole interaction. However, comparing the E-D and the D-D interactions gives a clue for solving this problem.

In Fig. 7.1 we plot the E-D and the D-D couplings as a function of distance between them for the [100], [110] and [111] directions in the range of 1 to 10 unit cells. In Fig. 7.2 we plot the same graph but this time in the range of 10 to 50 unit cells. In these figures the D-D interaction is at least three times smaller than the E-D interaction for large distances. To make sure that the D-D interaction is always smaller than the E-D interaction, we choose some random pairs and calculate the D-D and the E-D interactions for them. This calculation shows that the D-D interaction is always more than three times smaller than the E-D interaction. Hence, in this work we tentatively use the cut off method to apply the periodic boundary condition to the D-D interaction. The approximation we make in this calculation is to drop the long-range part of the D-D interaction compared to the E-D interaction which is justifiable based on the argument we had about the numerical results for E-D and D-D interactions.

By showing how to apply periodic boundary conditions to the long-range D-D and E-D interactions, our discussion about handling the two most difficult terms in the effective Hamiltonian is dealt with. However, there are other terms in the effective Hamiltonian such as bi-particle transverse terms, second and third nearest neighbor terms for which we need to implement periodic boundary conditions to them. We use the Ewald method to apply the periodic boundary condition for the dipole-dipole Ising interaction. For the second and the third nearest neighbors, the number of neighbors for both interactions are 12. However, we showed in

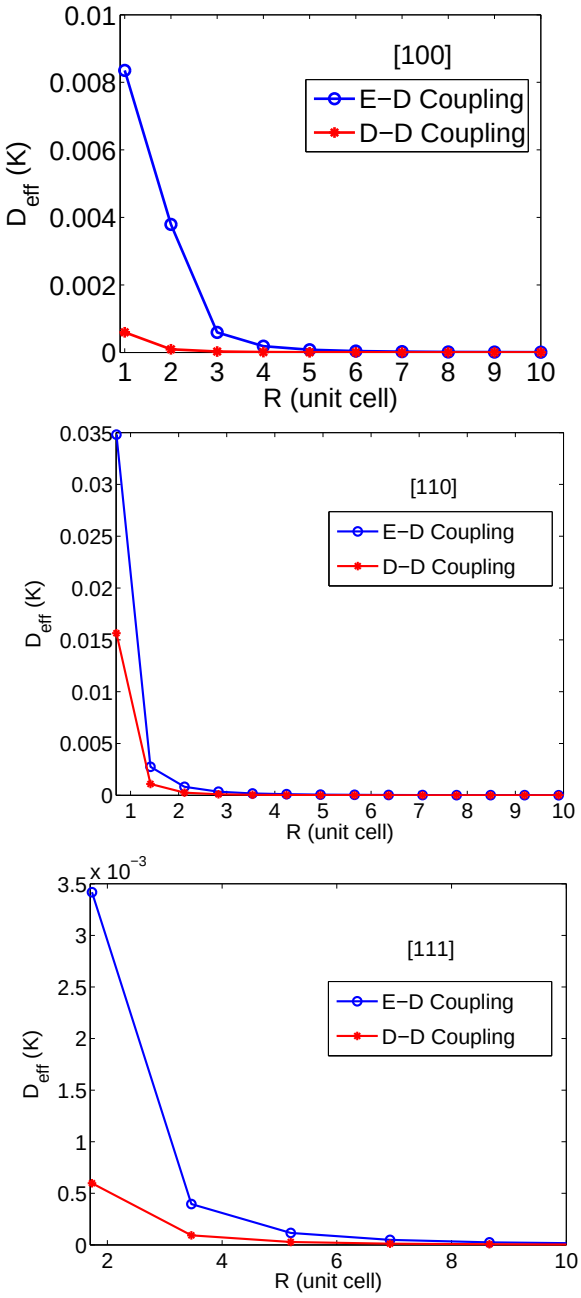


Figure 7.1: E-D and D-D couplings (here we show it by $D_{eff}$) as a function of distance between two spins for the symmetric directions [100], [110] and [111] and in the range of 1 to 10 unit cell.

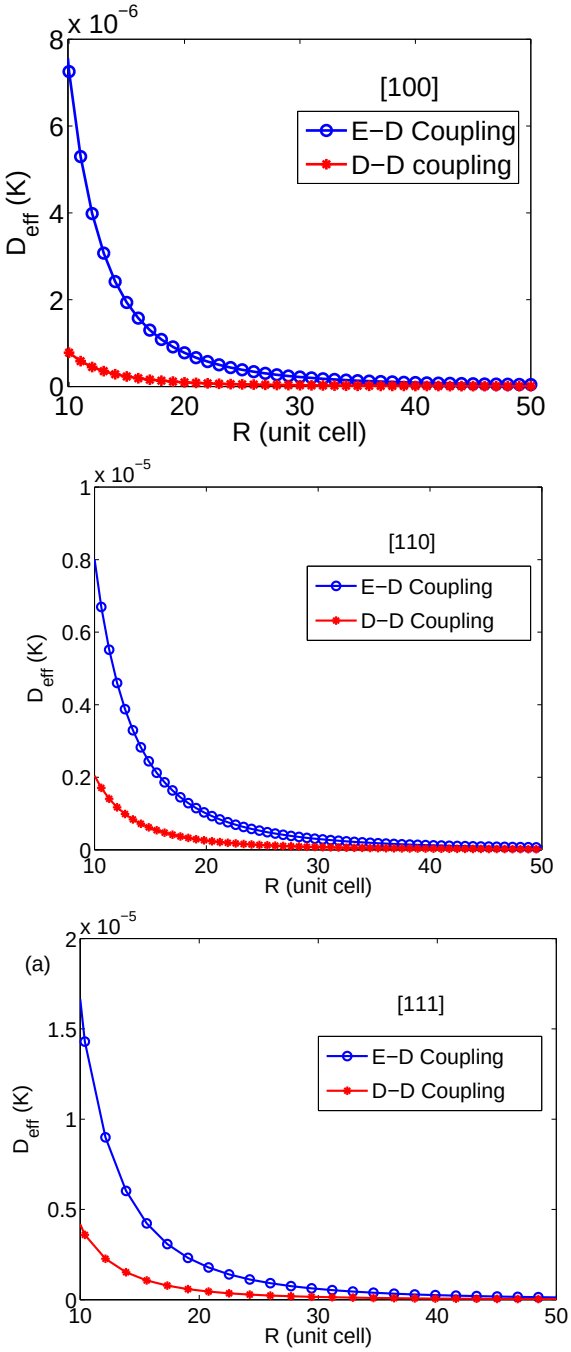


Figure 7.2: E-D and D-D couplings (here we show it by $D_{eff}$) as a function of distance between two spins separated along the [100], [110] and [111] directions and in the range of 10 to 50 unit cell.

the effective Hamiltonian chapter that the quantum Ising term generates the third nearest neighbors interaction for only six of the twelve third nearest neighbors. Hence, we apply the periodic boundary condition to the 12 second nearest neighbors and also to six of third nearest neighbors that are connected by one $Tb^{3+}$ ion (Section 4.3.1). The bi-particle transverse terms are the last terms for which we need to apply boundary conditions. It was mentioned in Section 4.4 that the long-range part of the bi-particle transverse terms drop off as $\frac{1}{r^6}$, where $r$ is the distance between two spins. Therefore, we use the cut off method to apply the periodic boundary condition to this part of the interaction.

## 7.3 Classical Ground State of $Tb_2Ti_2O_7$

After applying the periodic boundary condition on the E-D and the D-D interactions, we calculate in this section the classical ground state of $Tb_2Ti_2O_7$ by minimizing the classical energy of the system. Before embarking into the calculation it is interesting to ask what is the stable classical ground state of $Tb_2Ti_2O_7$ in a single tetrahedron approximation.

To find the classical ground state we assume that each spin is a classical rotor with SO(3) symmetry with fixed length of 1 in real space and we choose an initial random configuration of these spins. We find the new configuration of spins by moving each spin towards the local magnetic field caused by the interactions between this spin and other spins. We repeat this until we find that the difference between the direction of local field and the direction of spin at each site is less than a given threshold (in this simulation we use the threshold $10^{-8}$). This process can give a local minimum, thus we use a random generator which creates another initial configuration and repeat the procedure. We then compare the energy with the previous energy. If the energy is equal or larger than the previous one, the new state is declined and if it is smaller this state is chosen as the new ground state. We wrote a computer code to accomplish this simulation for thousands of attempted times to find the global classical ground state. We fix the value of the dipole-dipole coupling to the value known for $Tb_2Ti_2O_7$, $\mathcal{D}_{\rm nn}$=0.0315 K and find the classical ground state as a function of exchange coupling. In the single tetra-

hedron approximation we determine three stable phases for $Tb_2Ti_2O_7$. For $\mathcal{J} <$ 0.16K the classical ground state is two-in/two-out state which we naively expect. For 0.16 K $< \mathcal{J} <$ 0.22 K all spins move to the local xy plane such that the vector sum of the four spins becomes zero. We call this phase an XY phase. For $\mathcal{J} >$ 0.22 K the ground state of the system is all-in/all-out state. In Fig. 7.3 we plot the energy of these competing phases as a function of exchange interaction. In this phase diagram, $Tb_2Ti_2O_7$ is in the XY phase.

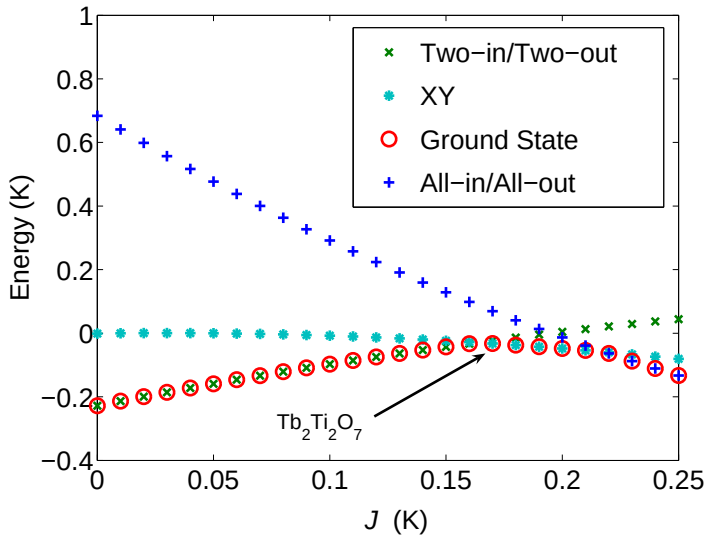


Figure 7.3: Competing classical phases of $Tb_2Ti_2O_7$ as a function of exchange coupling and in the single tetrahedron approximation. For $\mathcal{J} <$ 0.16 K the two-in/two-out state is the ground state and for 0.16 K $< \mathcal{J} <$ 0.22 K, the XY state (all spins are in the xy plane such that the vector sum of the four spins is zero) is the ground state. For $\mathcal{J} >$ 0.22 K the ground state of the system is the all-in/all-out state.

Having found the classical ground state of $Tb_2Ti_2O_7$ in the single tetrahedron approximation, we now proceed to calculate the classical ground state of $Tb_2Ti_2O_7$ in a larger unit cell. We consider a single cubic unit cell with 16 spins and we use the results of the E-D and the D-D interactions within a simulation box to calculate the classical ground state. We truncate the D-D and bi-particle transverse interactions at the third unit cells. We calculate the stable classical ground state with the

method explained in the previous paragraph. For the given dipole coupling of $Tb_2Ti_2O_7$and varying the exchange interaction, we find two candidate ground state for $Tb_2Ti_2O_7$: the Melko phase which is a Q=001 ordered spin ice phase (Section 1.2) and the Q=0 spin ice phase which is made of repeating a single tetrahedron with a two-in/two-out state through the FCC lattice. In this phase diagram $Tb_2Ti_2O_7$ is in the Q=0 spin ice state. In Fig. 7.4 we plot the energy of different well known competing phases as a function of exchange interaction and for the given dipole-dipole interaction of $Tb_2Ti_2O_7$. Naively, one would expect that for large exchange coupling the classical term of the effective Hamiltonian becomes larger than the quantum part, and we get the all-in/all-out phase. However, interestingly, for the whole range of exchange interactions, the ground state is not the all-in/all-out state and the Q=0 spin ice phase remains the ground state for large exchange interaction. This is because for large exchange coupling $\mathcal{J}$ the generated second and third nearest neighbors and also the E-D interaction become large and the ground state is determined not only by the classical exchange but also by the other interactions.

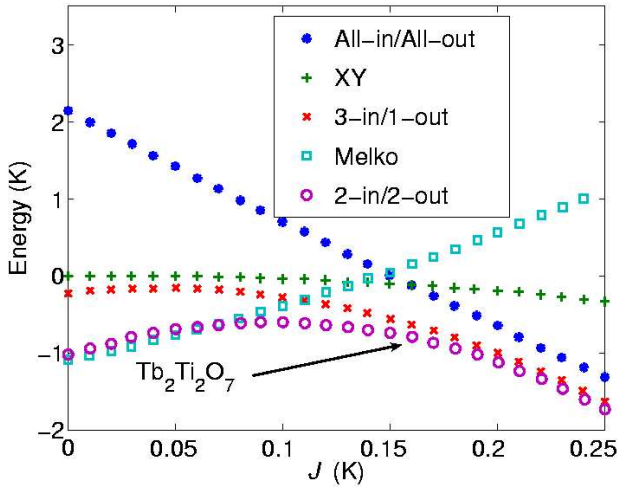


Figure 7.4: Competing classical phases of $Tb_2Ti_2O_7$ as a function of exchange coupling for a single unit cell with 16 spins. For $\mathcal{J} < 0.6$ K the Melko phase is the ground state and for 0.6 K $> \mathcal{J}$ the two-in/two-out $Q = 0$ state is the ground state.

## 7.4 Summary

In this chapter we applied periodic boundary conditions to all the interactions of the effective Hamiltonian of $Tb_2Ti_2O_7$ to study the classical ground state of $Tb_2Ti_2O_7$ in the single tetrahedron approximation and also for a single unit cell which contains 16 spins. For the single tetrahedron approximation we found that $Tb_2Ti_2O_7$ is in the XY phase. To apply the periodic boundary condition for the classical dipole-dipole interactions we used the Ewald result for the spin ice systems. We also showed that we can use the Ewald method of the spin ice systems to apply the periodic boundary condition to the E-D interaction. We showed that the D-D interaction is more than three times smaller than the E-D interaction and therefore we neglect the D-D interaction for long distances. For the bi-particle transverse terms of the effective Hamiltonian, we applied the cut-off method because these interactions drop off as $\frac{1}{r^6}$ ($r$ is the distance between two spins). Using these results we calculated the stable classical ground state of $Tb_2Ti_2O_7$ for a single unit cell and showed that it is $Q$=0 spin ice state. Moreover, we calculated the phase diagram of $Tb_2Ti_2O_7$ in terms of exchange interaction at zero temperature, and we showed that for $\mathcal{J} < 0.6$ K the ground state is the Melko phase and for $\mathcal{J} > 0.6$ K the ground state is the $Q$=0 spin ice phase. Having said this, one must conclude that these results are at this time tentative and further investigation of this challenging question would be both requested and interesting.

# Chapter 8

# $Tb_2Ti_2O_7$ in a Magnetic Field

In the previous chapters we studied the ground state and some of the physical properties of $Tb_2Ti_2O_7$ without any external perturbation. In this chapter we study the effect of an external magnetic field on $Tb_2Ti_2O_7$. Magnetization experiments on $Tb_2Ti_2O_7$ for different symmetry directions show a rather isotropic behaviour [37] in spite of the fact that the single ion crystal field ground state doublet is Ising-like. In this chapter we try to address this question in the context that the crystal field excited states change the low-energy Hamiltonian (Chapter 4) of $Tb_2Ti_2O_7$ from Ising-like to an anisotropic Heisenberg. We also propose an experiment based on magnetization measurement for different symmetry directions to ascertain whether $Tb_2Ti_2O_7$ has a quantum spin ice state. We organize this chapter as follows: in the first section, we study the eigenstates and eigenvalues of a single $Tb^{3+}$ ion in $Tb_2Ti_2O_7$ in a magnetic field. In the second section, we investigate the magnetization of $Tb_2Ti_2O_7$ in the non-interacting $Tb^{3+}$ ions approximation and show that the excited crystal field states do make the magnetic moments more isotropic. In Section 4, we compare the magnetization results of interacting $Tb^{3+}$ ions with the non-interacting system and we conclude that the observed isotropic behaviour of $Tb^{3+}$ ions is partly related to admixing of the excited crystal field states induced by the spin interactions. In Section 5, we propose an experiment based on the magnetization results to investigate whether $Tb_2Ti_2O_7$ possesses a quantum spin ice state. Because the single ion eigenenergies and eigenstates change with a magnetic

field, and to avoid any misunderstanding, from now on we refer to 'crystal field states' as the eigenstates of the crystal field Hamiltonian at zero magnetic field.

## 8.1 Crystal Field Levels of $Tb_2Ti_2O_7$ in a Magnetic Field

In this section we study the effect of a magnetic field on the energy levels of a non-interacting single ion of $Tb^{3+}$ in $Tb_2Ti_2O_7$. The Hamiltonian of this single ion is the sum of the crystal field and the Zeeman Hamiltonians which reads,

$$H = H_{\rm cf} + g\mu_{\rm B}\mathbf{B}\cdot\mathbf{J}, \tag{8.1}$$

where $H_{\rm cf}$ is the crystal field Hamiltonian given in Eq. (2.13), $g = \frac{3}{2}$ is the Landé factor for $Tb^{3+}$ ion, $\mu_{\rm B}$ is the Bohr magneton, $\mathbf{B}$ is the applied magnetic field and $\mathbf{J}$ is the total angular momentum of the $Tb^{3+}$ ion equal to 6. Because the Zeeman Hamiltonian does not commute with the crystal field Hamiltonian all the degeneracies of the crystal field states are lifted.

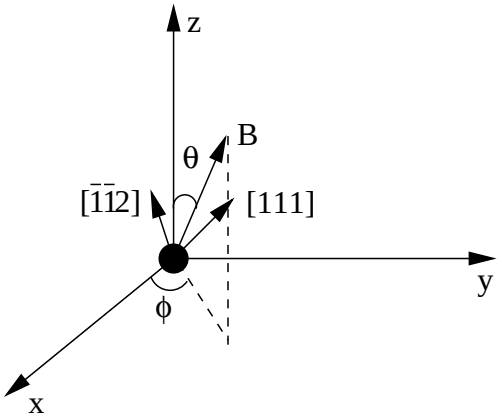


Figure 8.1: The applied magnetic field in the global coordinate frame with $\theta$ and $\phi$ as polar and azimuthal of the magnetic field. The $Tb^{3+}$ ion sits at the origin of coordinates and the $[11\bar{2}]$ and [111] local axis are specified.

Hence, the two states of the crystal field ground state and first excited state doublets, which govern the low-energy physics, are split into four singlets. In Fig.

8.2 we plot these four lowest energy states as a function of azimuthal angle and for $B$=0.01 T, 0.5 T and 5 T and $\theta$=90°, where the polar and azimuthal angles are measured from the global axis (Fig. 8.1). The special feature of these plots is a minimum gap between the ground state and first excited state, which are the splitted states of the crystal field ground state doublet, at $\phi$=135° where the magnetic field is perpendicular to the [111] axis. For this minimum angle the matrix elements of the Zeeman Hamiltonian projected within the crystal field ground state doublet are zero. As a result, the energy gap between two lowest energy states originates from the crystal field excited states and, based on second order perturbation theory, the gap changes as $B^2$ at low magnetic fields (Fig. 8.3).

After studying the energy levels of a $Tb^{3+}$ ion as a function of azimuthal angle it is interesting to study their behaviour as a function of polar angle ($\theta$) as well. From the results of this calculation we propose an experiment in Section 8.4 to test for the quantum spin ice ground state in $Tb_2Ti_2O_7$. In Fig. 8.4 we plot the lowest energy levels of Hamiltonian (8.1) as a function of polar angle for $B$=0.01 T, 0.5 T and 5 T and $\phi$=225° (we choose this value of $\phi$ because we use it for our future study). The same behaviour as the previous graphs is observed with the minimum gap occurring at $\theta$=35.2° where the magnetic field is perpendicular to the [111] easy axis. This magnetic field is parallel to the $[\bar{1}\bar{1}2]$ axis which has been used to verify the spin ice ground state in the $Dy_2Ti_2O_7$ spin ice material [66]. In Fig. 8.5, we plot this minimum energy gap as a function of applied magnetic field and this graph again reveals a $B^2$ behaviour at the minimum gap at low magnetic fields.

To investigate the behaviour of these energy levels for different symmetry directions we plot them (Fig. 8.6) as a function of the magnetic field strength for the [100], [110] and [111] directions. The observed feature at $B$=2 T is related to the level crossing of the second and the third lowest crystal field states. This level crossing is smooth because of the following reason: the second and the third lowest crystal field states in terms of eigenstates of $J^z$ are, respectively, $\alpha_1|+4\rangle+\beta_1|-5\rangle+...$ and $\alpha_2|-5\rangle+\beta_2|+4\rangle+...$, where $\alpha_1$ and $\alpha_2$ are much larger than $\beta_1$ and $\beta_2$. Increasing the magnetic field, the energy of the third state, which has its predominant part at $|-5\rangle$, starts decreasing while on the other hand the energy of the second state starts increasing until $B$=1.5 T. From this point an increase in the magnetic

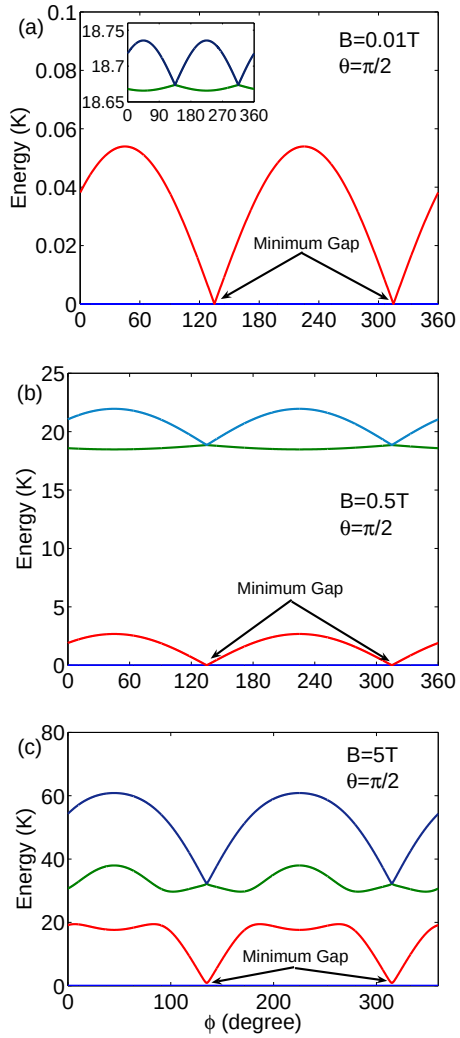


Figure 8.2: Four lowest levels of Hamiltonian (8.1) as a function of azimuthal angle $\phi$ with $\theta$=$\frac{\pi}{2}$ and with a field $B$=0.01 T(a), $B$=0.5 T(b) and $B$=5 T(c) magnetic fields (Because the splitting of the states at $B$=0.01 T is very small, the two states of the excited states are shown in the inset). The correspondent eigenstates of these energy levels at zero magnetic field, are the crystal field ground state and first excited state doublets. These doublets are splitted and their splitted states evolve under an applied magnetic field.

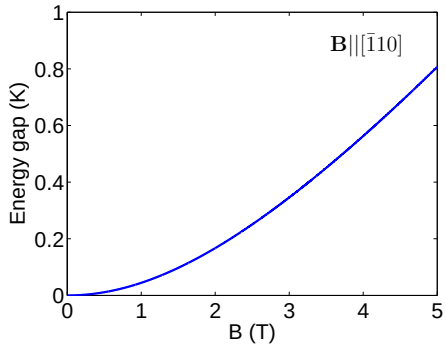


Figure 8.3: Energy gap between ground state and first excited state (the splitted states of the crystal field ground state doublet) as a function of a magnetic field applied along the [$\bar{1}$10] direction.

field decreases the coefficients $\alpha_1$ and $\alpha_2$ and increases the coefficients $\beta_1$ and $\beta_2$ are increasing. This process can be interpreted as the transfer of angular momentum from one state to another as a result of the magnetic field. This transfer of angular momentum continues until $B$=5 T where this smooth level crossing between the second and the third states becomes complete. In the [111] direction the reduction in the third energy level continues until it crosses the ground state at 16.3 T and becomes the ground state of the system. This level crossing, especially in the ground state, can be observed experimentally as a signature in some physical phenomena such as the field dependent magnetization.

## 8.2 Non-Interacting $Tb^{3+}$ Ions in a Magnetic field

In this section we study the magnetization of non-interacting $Tb^{3+}$ ions in $Tb_2Ti_2O_7$. This compound has four magnetic sublattices with different easy axes and therefore the total magnetization per ion reads,

$$\mathbf{M} = \frac{1}{4}\sum_{a}^{4} \mathbf{M}_a \tag{8.2}$$

where $\mathbf{M}$ is the total magnetization per ion and $\mathbf{M}_a$ is the magnetization of sublattice $a$ and the sum is over the four sublattices. The magnetization for each

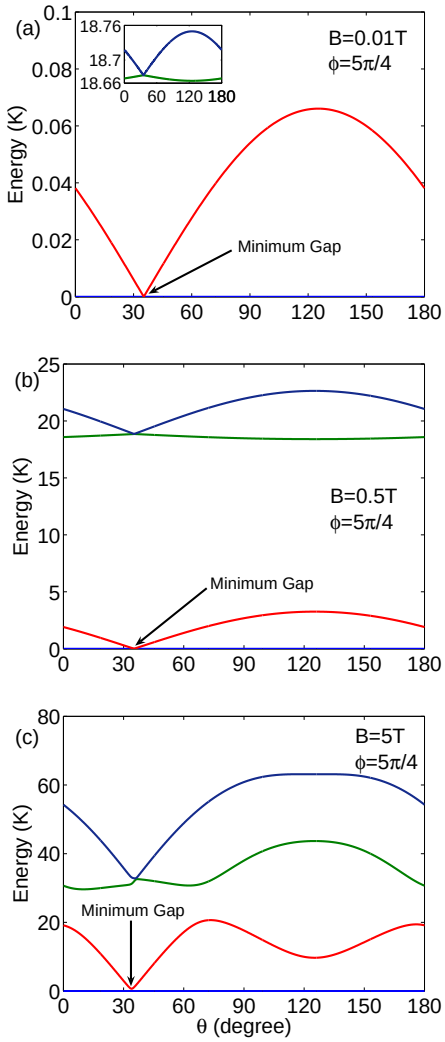


Figure 8.4: Four lowest energy levels of single $Tb^{3+}$ ion as a function of polar angle $\theta$ and with a field of $B$=0.01 T (a), $B$=0.5 T (b) and $B$=5 T (c) magnetic fields (Because the splitting of the states at $B$=0.01 T is very small, the two states of the excited states are shown in the inset). The correspondent eigenstates of these energy levels at zero magnetic field, are the crystal field ground state and first excited state doublets. These doublets are splitted and their splitted states change under an magnetic field.

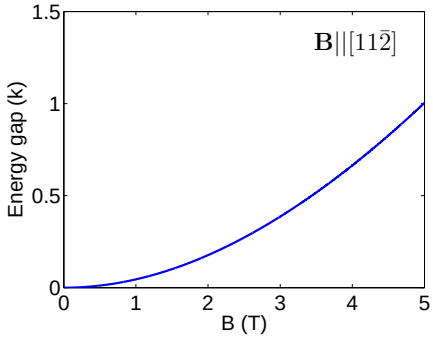


Figure 8.5: Energy gap between the ground state and first excited state as a function of magnetic field along [11$\bar{2}$] direction.

sublattice is given by,

$$M_a^\alpha = g\mu_B \sum_{\nu=1}^{13} u_a^{\alpha\beta} \langle\psi_\nu|J^\beta|\psi_\nu\rangle n_B(E_\nu) \tag{8.3}$$

where $M_a^\alpha$ is the $\alpha$ component of the magnetization of sublattice $a$, $g = \frac{3}{2}$ is the Landé factor for $Tb^{3+}$, $\mu_B$ is the Bohr magneton, $u_a^{\alpha\beta}$ is the rotation matrix from the local to the global axis for sublattice $a$ (Appendix C), $J^\alpha$ is the $\alpha$ component of the total angular momentum of $Tb^{3+}$ with J=6, $|\psi_\nu\rangle$ is the $\nu^{\text{th}}$ eigenstate of Hamiltonian (8.1), $n_B(E_\nu)$=exp$(-\frac{E_\nu}{k_B T})$ is the Boltzmann population of state $\nu$ with energy $E_\nu$ at temperature $T$, and the sum is carried out over all 13 eigenstates of Hamiltonian (8.1). We calculated the magnetization for **B** along the [100], [110] and [111] directions at different temperatures. The results of these calculations are shown in Fig. 8.7.

The magnetization in [100], [110] and [111] directions saturates respectively at 6.8 $\mu_B/Tb^{3+}$, 6.6 $\mu_B/Tb^{3+}$ and 7.2 $\mu_B/Tb^{3+}$ for $B < 30$ T and no feature is observed for the magnetization data in the [100], [110] directions. However, a plateau is observed at B=16.2 T and $T$=1 K in the [111] magnetization data which is related to the level crossing that we discussed in the previous section. The saturation values for different directions is consistent with isotropic moments with the $< J^z >$=5 and $< J^z >$=4 as the major contributors to the ground state. This can be naively seen if we use the $M = g\mu_B\langle\psi_\nu|J^z|\psi_\nu\rangle$ expression with $\psi_\nu$ as the crystal field ground

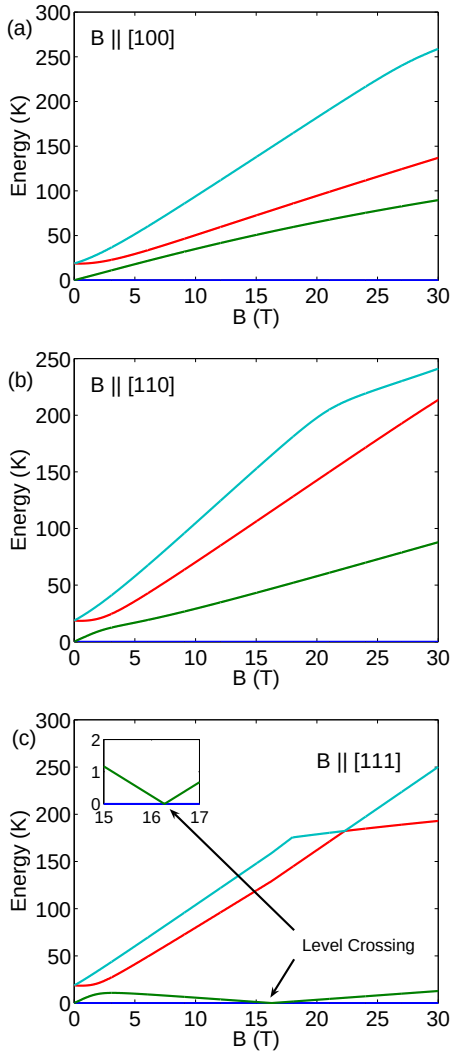


Figure 8.6: Four lowest levels of Hamiltonian (8.1) as a function of magnetic field along [100], [110] and [111] directions. The observed feature between 1.5 T to 5 T is related to the angular momentum transfer from the first excited state to the second excited state. In the [111] magnetization a level crossing between the ground state and first excited state happens at $B$=16.2 T.

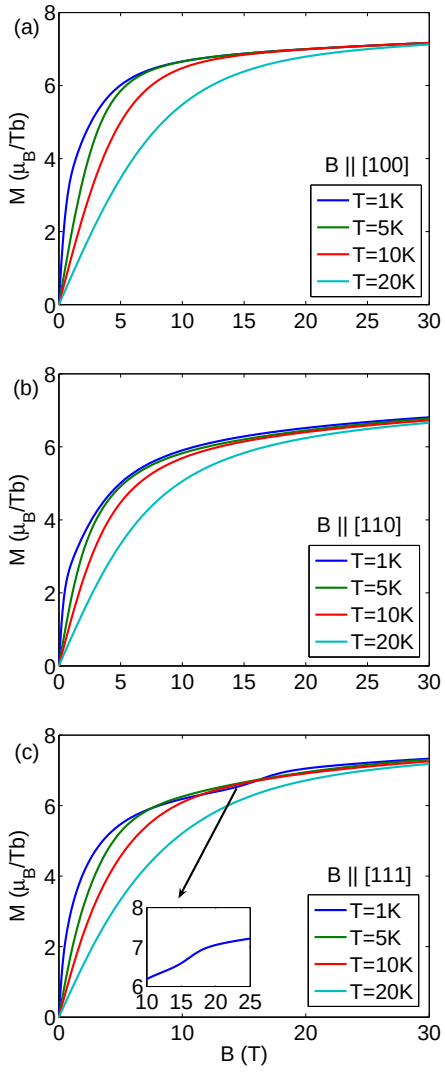


Figure 8.7: Magnetization of four non-interacting $Tb^{3+}$ ions on a single tetrahedron for a magnetic field $B$ along the [100], [110] and [111] directions. The observed plateau at $B$=16.2 T is related to the level crossing between the ground state and first excited state.

state doublet. This value is still far from the 9.72 $\mu_B/Tb^{3+}$ for the free $Tb^{3+}$ ion. To further compare the behaviour of the magnetic moments in different directions, we plot in Fig. 8.8 the [100], [110] and [111] magnetization data as a function of magnetic field and for $T$=1 K and 5 K and 20 K.

At $T$=1 K the behaviour of the magnetization is qualitatively similar to the spin ice systems with the highest magnetization at [100] direction and the lowest magnetization at [110] direction [36]. Increasing the temperature, the magnetization along different directions develops a more isotropic behaviour and at $T$=20K the magnetization along the three directions are very much converged together. In Fig. 8.9 we plot the ratio of the magnetization in the [100] direction to the magnetization in the [110] direction, as a function of magnetic field. For $T$=1 K this ratio reaches a maximum $\frac{M^{[100]}}{M^{[110]}}$=1.279 at $B$=1.4 T which is smaller than the spin ice limit 1.414. Increasing the temperature this ratio converges to 1 since the excited states become more populated (by the thermal excitations) and, as a result, the magnetic moments behave effectively isotropically. Experimental results of magnetization (Fig 1.16) show that the effective magnetic moments in $Tb_2Ti_2O_7$ are more isotropic than what we found in this section. Hence, there should be another mechanisms such as higher order Zeeman terms in the Hamiltonian which give rise to the observed isotropy in the experimental results.

## 8.3 Interacting $Tb^{3+}$ Ions in a Magnetic Field

In this section we calculate the magnetization of interacting $Tb^{3+}$ ions in $Tb_2Ti_2O_7$ within the single tetrahedron approximation and under an applied magnetic field. We showed in Chapter 2 that the excited crystal field states above the first excited state doublet are separated by a gap which is more than 100 K. Hence, quantitatively, these states are irrelevant in describing the low energy physics of $Tb_2Ti_2O_7$. In Chapter 5 we showed that the four crystal field lowest states give results that are in semi-quantitative agreement with the exact results. Hence, choosing any subset of the crystal field states containing the four lowest states or more is enough to describe the interacting part of the Hamiltonian at low temperatures. To find a sufficient subset of crystal field states that quantitatively describe the Zeeman term

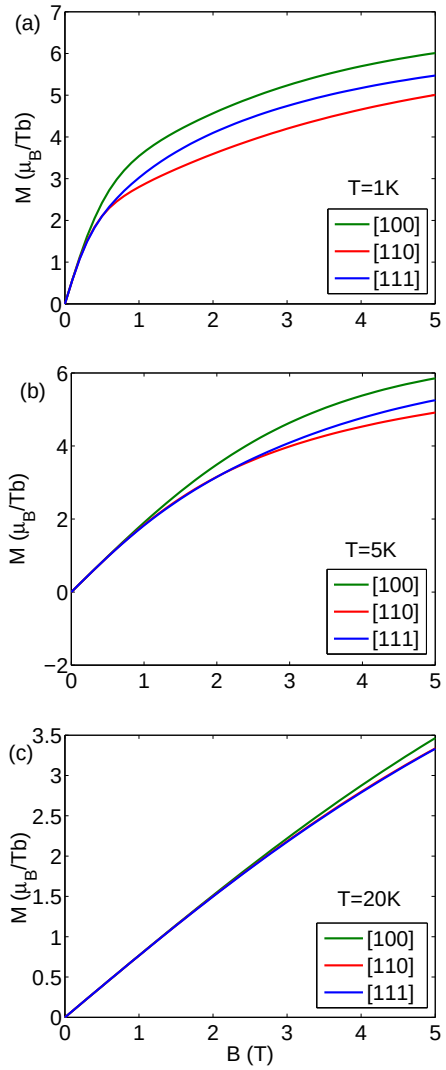


Figure 8.8: Magnetization of non-interacting $Tb^{3+}$ ions on a single tetrahedron for a magnetic field along [100], [110] and [111] directions and at $T$=1 K (a), 5 K (b) and 20 K (c).

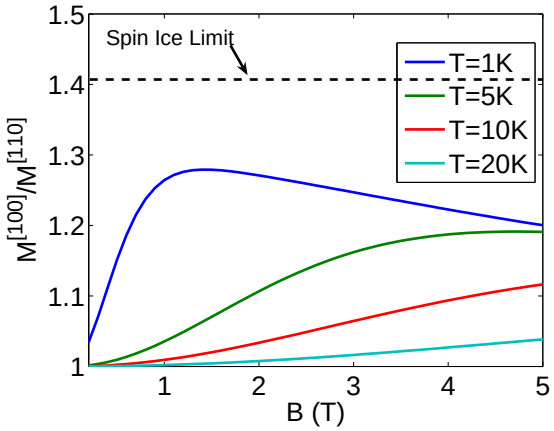


Figure 8.9: The ratio between the magnetization of non-interacting $Tb^{3+}$ ions at [100] direction to [110] direction $M^{[100]}/M^{[110]}$, as a function of magnetic field and for $T$= 1, 5, 10 and 20 K.

of the Hamiltonian we compare the exact magnetization of non-interacting $Tb^{3+}$ ions (with thirteen states) with the magnetization derived from various subsets of the crystal field states.

In Fig. 8.10 the magnetization of non-interacting $Tb^{3+}$ ions as a function of magnetic field with four states, six states and thirteen states per ion is depicted. From these results we conclude that choosing the four lowest crystal field states per ion is not enough to adequately describe the exact results. However, choosing the six lowest crystal field states gives a result that is quantitatively consistent with the exact results. Therefore, in the rest of this chapter we use the six lowest crystal field states to calculate the physical properties of $Tb_2Ti_2O_7$ in the single tetrahedron approximation.

The total Hamiltonian of the system in this approximation is,

$$H = \sum_{a>b}(H_{ab}^{\rm ex} + H_{ab}^{\rm dip}) + \sum_{a=1}^{4} H_a^{\rm Zeeman}, \tag{8.4}$$

where $H_{ab}^{\rm ex}$ and $H_{ab}^{\rm dip}$ are respectively the exchange and the dipole-dipole Hamiltonians for pair $ab$ and $H_a^{\rm Zeeman}$ is the Zeeman Hamiltonian for ion $a$. We calculate the matrix elements of this Hamiltonian in the six lowest crystal field basis states and,

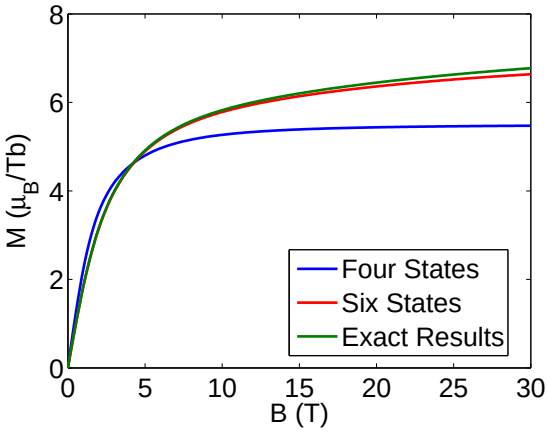


Figure 8.10: Magnetization of a non-interacting single $Tb^{3+}$ ion in $Tb_2Ti_2O_7$ derived from the four, six and thirteen lowest crystal field states. The set of six lowest crystal field states is a minimum set of crystal field states that quantitatively described the exact result (thirteen states).

using the exact diagonalization method, we find its eigenvalues and eigenstates. We use these eigenstates and eigenvalues to calculate the magnetization of $Tb_2Ti_2O_7$ in the single tetrahedron approximation. The magnetization per ion for this magnetic system reads,

$$M^{\alpha} = \frac{g\mu_{\mathrm{B}}}{4} \sum_{\nu} \sum_{a=1}^{4} u_a^{\alpha\beta} \langle \phi_\nu | J^{\beta} | \phi_\nu \rangle n_{\mathrm{B}}(E_\nu), \tag{8.5}$$

where $M^{\alpha}$ is the $\alpha$ component of the total magnetization per ion, $|\phi_\nu\rangle$s are the eigenstates of the Hamiltonian, $u_a^{\alpha\beta}$ is the $\alpha\beta$ component of the rotation matrix from the local to the global axis of sublattice $a$, $J^{\alpha}$ is the $\alpha$ component of the total angular momentum of $Tb^{3+}$ ion with J=6, $n_{\mathrm{B}}(E_i)$=exp($\frac{E_\nu}{k_{\mathrm{B}}T}$) is the Boltzmann population of state $\nu$ with energy $E_\nu$ and temperature $T$, the sum on $\nu$ is over all $6^4$=1296 eigenstates of the Hamiltonian and the sum on $a$ is over the four sublattices. We calculate the magnetization of this system for the [100], [110] and [111] directions and at $T$=1, 5, 10 and 20 K. The results of these calculations are shown in Fig. 8.11. The magnetization data for the [111] direction shows a plateau at $B$=16.2 T and this plateau is less steep compared to the non-interacting case (Fig. 8.7). The magnetization in different directions also saturates to values which

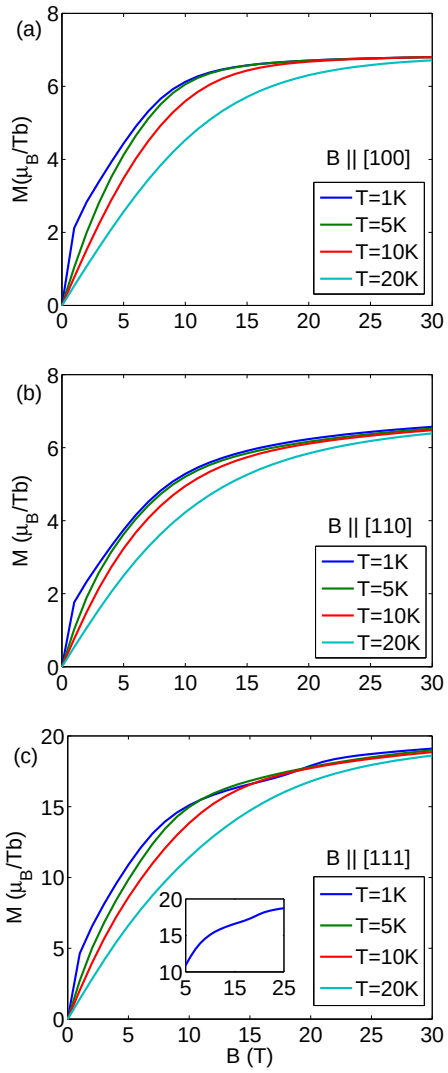


Figure 8.11: Magnetization of four interacting $Tb^{3+}$ ions on a single tetrahedron with six states per each ion along the [100], [110] and [111] directions. The plateau observed in the [111] direction and at $B$=16.2 is less steep compare to the non-interacting result.

are lower than the saturation values for the non-interacting $Tb^{3+}$ ions (Fig. 8.7). This can be explained in the sense that the ground state of the system without magnetic field is a quantum spin ice state and, as a result, a fraction of applied magnetic field works to cancel out the internal field and breaks the quantum spin ice state and aligns all the magnetic moments towards the magnetic field. In Fig. 8.12 we plot the [100], [110] and [111] magnetization data at $T$=1 K and 5 K , 10 K as a function of magnetic field. At $T$=1 K the magnetization shows a qualitative spin ice behaviour meaning that the highest and lowest magnetizations are respectively in the [100] and [110] directions. At $T$=5 K the magnetization in the [110] and [111] directions become closer which is a sign of more isotropic magnetic moments at this temperature rather than Ising-like magnetic moments. At this temperature the magnetization along the [100] direction still shows Ising-like behavior. In Fig. 8.13 we plot the ratio of magnetization in the [100] direction to the magnetization in the [110] direction. Comparing these results with the non-interacting results (Fig. 8.8) shows a decrease in this ratio. This indicates that the interactions render the magnetic moments behave more isotropically and this can be physically understood if we recall that the interactions create transverse terms operating within the manifold of the ground state.

## 8.4 Probing the Ground State of $Tb_2Ti_2O_7$

In this section we propose an experiment to investigate the ground state of $Tb_2Ti_2O_7$ using magnetization measurements for fields along different directions. To start, we label the four sublattices and their correspondent $Tb^{3+}$ ions from 1 to 4 (Fig. 8.14) with their easy axis being respectively, [111], $[\bar{1}\bar{1}1]$, $[1\bar{1}\bar{1}]$ and $[\bar{1}1\bar{1}]$. We explained in Section 8.1 that for a $Tb^{3+}$ ion sitting on sublattice 1 and for some specific magnetic field direction, the gap between the ground state and the first excited state reaches a minimum (Figs. 8.2 and 8.4). One of these directions is the $[11\bar{2}]$ direction. For this direction of magnetic field ($[11\bar{2}]$), ions on sublattices 2, 3 and 4 experience a magnetic field with strength $\frac{2\sqrt{2}}{3}B$ for ion 2 and $\frac{\sqrt{2}}{3}B$ for ions 3 and 4 towards their easy axes. Therefore, for a magnetic field along the $[11\bar{2}]$ direction and of strength larger than the effective internal interactions only

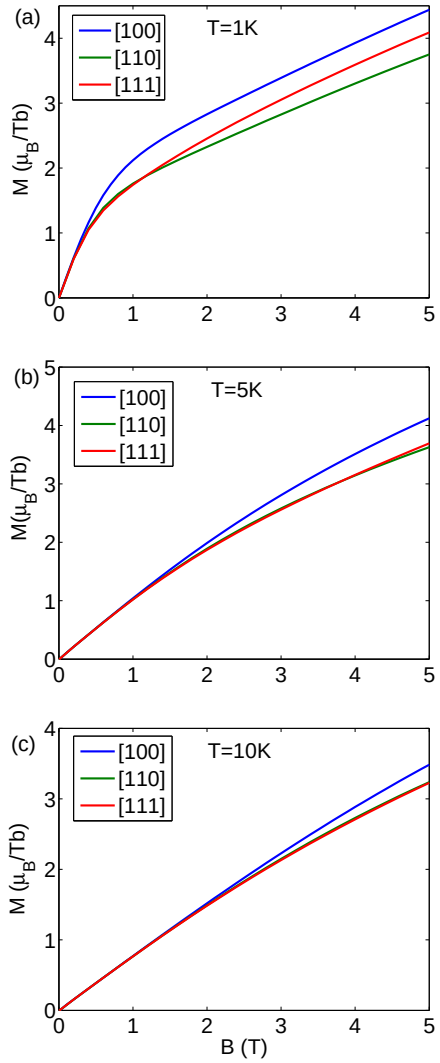


Figure 8.12: Magnetization of an interacting single tetrahedron with four $Tb^{3+}$ ions along the [100], [110] and [111] directions at $T$=1 K (a), 5 K (b) and 10 K (c).

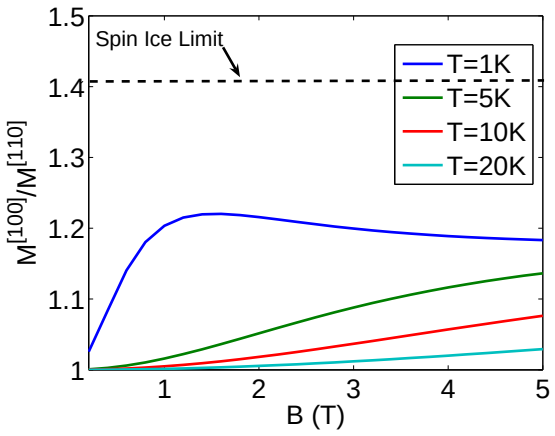


Figure 8.13: The ratio between the magnetization of non-interacting $Tb^{3+}$ ions at [100] direction to [110] direction $M^{[100]}/M^{[110]}$, as a function of magnetic field and for $T=$ 1, 5, 10 and 20 K. For a given magnetic field this ratio is smaller than the non-interacting approximation (Fig. 8.9).

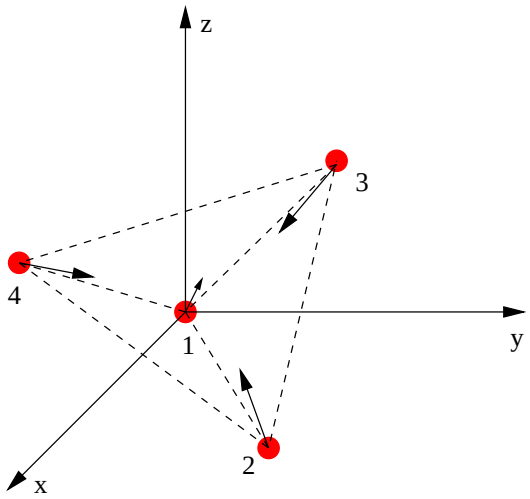


Figure 8.14: Nomenclature of four sublattices from 1 to 4 in a single tetrahedron. The easy axis for ions 1 to 4 are, respectively [111], $[\bar{1}\bar{1}1]$, $[1\bar{1}\bar{1}]$ and $[\bar{1}1\bar{1}]$.

sublattice 1 possesses a minimum gap while the three other sublattices possess a singlet ground state enforced by the magnetic field (Fig. 8.15).

We now use this observation to propose an experiment to characterize the ground state of $Tb_2Ti_2O_7$. Since the magnetic fields in the present calculations are small, the crystal field states do not change much and, to simplify our discussion, we denote the two states of the crystal field ground state with spin up, $|\uparrow\rangle$ and spin down, $|\downarrow\rangle$. We begin the calculation by considering the single tetrahedron approximation with four ions and six states per ion and apply a magnetic field towards the $[11\bar{2}]$ direction. The Hamiltonian of the system can be written down as,

$$H = \sum_{a>b}(H_{ab}^{\text{ex}} + H_{ab}^{\text{dip}}) + g\mu_B \sum_{a}^{4} \mathbf{J}_a \cdot \mathbf{B}^{[11\bar{2}]}, \tag{8.6}$$

where $\mathbf{B}^{[11\bar{2}]}$ is the applied magnetic field towards the global $[11\bar{2}]$ direction. We choose the strength of the magnetic field such that first it forces the magnetic ions 2, 3 and 4 to possess a unique state and second it does not affect the low energy spectrum dramatically. By the first condition the gap between the ground state and first excited state for ions 2, 3 and 4 is more than the effective interaction between them and as a result they are forced to stay in one state. By the second condition the initial eigenstates (eigenstates with $\mathbf{B} = 0$) remain a good quantum states. Applying a magnetic field with a strength of 0.1 T fulfills these criteria. With this specific magnetic field, ions on sublattices 2, 3 and 4 respectively possess $|\downarrow\rangle$, $|\uparrow\rangle$ and $|\uparrow\rangle$ states. For ion 1 we see from Fig. 8.5 that the gap between the ground state and the first excited state is very small and they can be considered to be a doublet. As a result, ion 1 possesses a ground state largely enforced by the internal field from other ions.

Now, we consider the two phases of quantum spin ice discussed in Chapter 5, the doublet and the singlet phases. In the singlet phase, application of the $[11\bar{2}]$ field puts the system in the $\beta_s|\downarrow\downarrow\uparrow\uparrow\rangle + \gamma_s|\phi\rangle$ state where $\beta_s \gg \gamma_s$ and $|\phi\rangle$ shows the contribution form other states. Here ion 1 possesses the $|\downarrow\rangle$ state in order to obey the two-in/two-out state. By applying a further magnetic field to this system along the [111] direction and measuring the magnetization in this direction, we see a continual increase in the magnetization (Fig. 8.16(a)). However, if we reverse the

direction of the [111] magnetic field and increase the strength of the field, the $Tb^{3+}$ ion 1 flips from state $|\downarrow\rangle$ to state $|\uparrow\rangle$ and as a result the magnetization changes sign for a sufficiently large field (Fig. 8.16(a)).

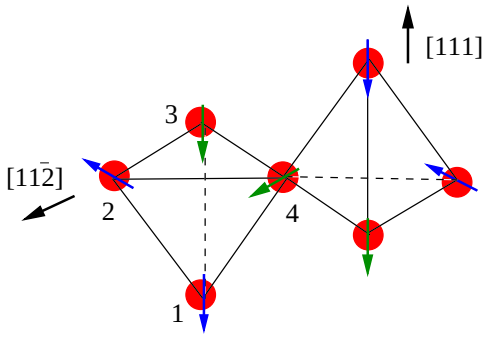


Figure 8.15: The configuration of magnetic moments in the spin ice phase and under a magnetic field in the [11$\bar{2}$] direction. Applying a magnetic field in the [111] direction with strength more than the effective internal interaction reverse the magnetic moment in site 1.

In the doublet phase we apply exactly the same procedure with the only difference in the initial state of the system being $\beta_d|\uparrow\downarrow\uparrow\uparrow\rangle + \gamma_d|\phi\rangle$ ($\beta_d \gg \gamma_d$). In this case ion 1 takes on the $|\uparrow\rangle$ state to minimize its energy by being parallel to two ions 3 and 4. Hence, in contrast to the singlet phase, here applying a magnetic field in the [111] direction flips spin 1 from state $|\uparrow\rangle$ to state $|\downarrow\rangle$ and the magnetization changes sign (Fig. 8.16(b)). On the other hand applying a magnetic field in the [$\bar{1}\bar{1}\bar{1}$] direction increases the magnetization without any change in the sign of magnetization (Fig. 8.16(b)).

From the above discussion we conclude that by applying a magnetic field with strength 0.1 T in the [11$\bar{2}$] direction and another magnetic field in the [111] direction we can find a direct evidence to test the quantum spin ice state in $Tb_2Ti_2O_7$.

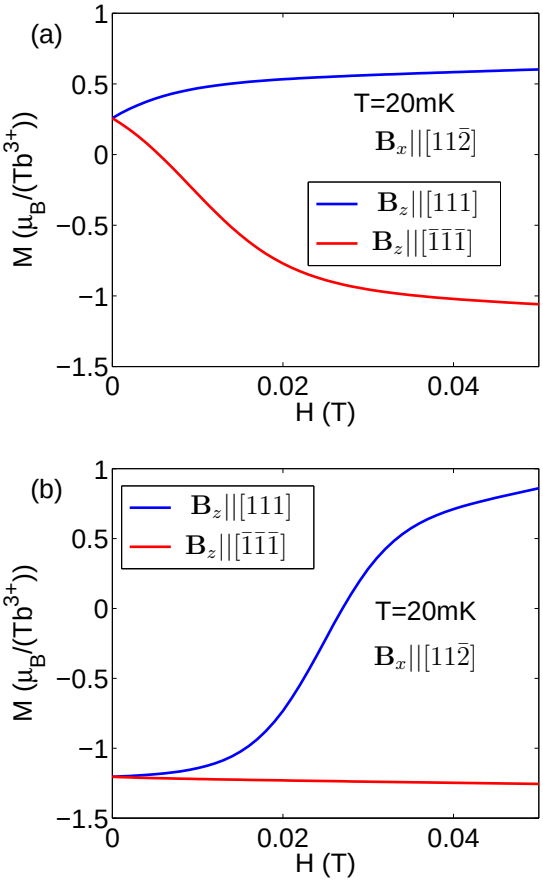


Figure 8.16: Magnetization in the [111] direction as a function of applied magnetic field along the [111] direction at 20 mK in the doublet (top figure) and the singlet (down figure) states under a constant magnetic field 0.1 T along the $[11\bar{2}]$ direction.

## 8.5 Summary

In this chapter, we studied the behaviour of $Tb_2Ti_2O_7$ in a magnetic field. We started by calculating the single ion crystal field levels of non-interacting $Tb^{3+}$ ions in a magnetic field. We showed that the gap between the ground state and the first excited state has a minimum for directions that are perpendicular to the local easy axis. For small magnetic fields this gap changes as $B^2$. For a range of magnetic fields between 1.5 T to 5 T, we observed a transfer of angular momentum from the second excited state to the third excited state. We also showed that a level crossing between the ground state and first excited state happens at $B$=16.2 T. We calculated the magnetization of $Tb_2Ti_2O_7$ in the non-interacting $Tb^{3+}$ approximation and observed a plateau in the magnetization data for $\mathbf{B}$ along [111] direction and at $B$=16.3 T, which is related to the level crossing. By comparing the magnetization for different directions, we also found that at low temperatures the system behaves qualitatively like spin ice systems. At high temperatures, when the first excited crystal field states becomes populated, the magnetization results show a rather isotropic behaviour. We also calculated the magnetization of $Tb_2Ti_2O_7$ in the presence of the spin interactions and within the single tetrahedron approximation, using six states per ion. The magnetization data show an even more isotropic behaviour compared to the non-interacting case which can be interpreted via the presence of transverse terms in the effective Hamiltonian discussed in Chapter 4. In the last section, we proposed a magnetization experiment to ascertain whether $Tb_2Ti_2O_7$ is in the quantum spin ice phase.

# Chapter 9

# Summary and Future Work

## 9.1 Effective Hamiltonian of $Tb_2Ti_2O_7$

The single ion crystal field Hamiltonian of $Tb^{3+}$ in $Tb_2Ti_2O_7$ and its eigenvalues and eigenstates have been calculated. It was shown that the crystal field gap between the ground state and first excited state is quite a bit larger than the interaction Hamiltonian. Using this fact, and by applying the Rayleigh-Schrödinger perturbation theory, an effective Hamiltonian in terms of spin 1/2 operators has been derived. It was shown that, to first order in perturbation theory, the effective Hamiltonian is built of interacting $\langle 111 \rangle$ Ising spins on the pyrochlore lattice, i.e. a classical $\langle 111 \rangle$ Ising Hamiltonian as previously studied in the context of spin ices [32] .

To investigate the effects of excited crystal field states, the effective Hamiltonian was calculated up to second order in perturbation theory. Two processes (fluctuation channels) have been identified at that order: the single ion and the double ion excitations. We showed that the single ion excitations of $Tb^{3+}$ ions generate terms with $\langle 111 \rangle$ Ising symmetry between a pair of Ising spins in the effective Hamiltonian (quantum Ising term). These terms not only renormalize the classical Ising interaction, but also generate new terms such as second and third nearest neighbor interactions between Ising spins. At the first nearest neighbor, the quantum Ising terms change the classical antiferromagnetic interaction to ferromagnetic. It

was shown that the double ion excitations create transverse terms in the effective Hamiltonian and change the effective Hamiltonian from $\langle 111 \rangle$ Ising-like system to that of an effective anisotropic $S = 1/2$ model.

## 9.2 $Tb_2Ti_2O_7$ in the Single Tetrahedron Approximation

The phase diagram of $Tb_2Ti_2O_7$ with the single ion crystal field ground state doublet and first excited state crystal field doublet, has been calculated within the single tetrahedron approximation. Two states have been found as the ground state: a doublet which is predominantly made of the classical all-in/all-out state and a singlet which is predominantly built of a linear combination of all frustrated two-in/two-out states. In this phase diagram, $Tb_2Ti_2O_7$ is in the singlet state which we named *quantum spin ice*. It was shown that the quantum Ising term changes the classical antiferromagnetic interaction to ferromagnetic and makes the Ising spins on the tetrahedron frustrated. The transverse terms, originated from the virtual double ion excitation, lift the degeneracy of these frustrated states and are responsible for the quantum (singlet) nature of the ground state.

Motivated by the fact that the experimental correlations in $Tb_2Ti_2O_7$ are of the order of an atomic distance, the diffuse neutron scattering of $Tb_2Ti_2O_7$ has been calculated in the single tetrahedron approximation with four lowest crystal field states. The obtained diffuse neutron scattering pattern captures all the features of the experimental neutron scattering. We showed that inelastic neutron scattering originates from fluctuations among the lowest states and is responsible for the intensity pattern of the experimental diffuse neutron scattering. An experiment based on the diffuse neutron scattering was proposed to confirm the spin ice like ground state in $Tb_2Ti_2O_7$.

The magnetization of non-interacting and interacting $Tb^{3+}$ ions has been calculated within the single tetrahedron approximation. We showed that the excited crystal field states subject to the interaction between $Tb^{3+}$ ions, change the symmetry of magnetic moments from $\langle 111 \rangle$ Ising like to more Heisenberg-like. An

experiment based on the magnetization for fields applied along different directions was proposed to verify the spin ice like ground state in $Tb_2Ti_2O_7$.

## 9.3 Beyond the Single Tetrahedron Approximation

The effective Hamiltonian of $Tb_2Ti_2O_7$ was calculated using periodic boundary condition, with Ewald method applied to calculate the long-range part of the effective Hamiltonian. By considering the spin 1/2 operators as classical rotors, the classical ground state of the effective Hamiltonian was determined for a single cubic unit cell. It was found that the classical ground state of $Tb_2Ti_2O_7$ is a two-in/two-out $Q$=0, which differs from the previously identified strictly classical $\langle 111 \rangle$ Ising spins.

In conclusion we found that the quantum fluctuations via the excited crystal field states renormalize the low energy Hamiltonian of $Tb_2Ti_2O_7$ and change the coupling between Ising $\langle 111 \rangle$ spins from antiferromagnetic to ferromagnetic. These quantum fluctuations, also change the symmetry of the degrees of freedom of the low energy Hamiltonian from Ising-like to a more isotropic system, namely pseudo-spin 1/2 system. We also show that these quantum fluctuations are responsible for the diffuse neutron scattering of $Tb_2Ti_2O_2$. These results show the importance of the quantum fluctuations in systems with large angular momentum which are usually considered as classical spins.

## 9.4 Future Work

We showed in Chapter 6 that the classical ground state of $Tb_2Ti_2O_7$ is a $Q$=0 two-in/two-out state. This ground state was obtained by assuming that spins are classical rotors and the quantum effects were not considered. To verify the stability of this ground state under the presence of quantum fluctuations, a $1/S$ expansion could be employed. This method was used to find the stability of the classical

ground state in $Gd_2Ti_2O_7$ [65] and a similar $1/S$ calculation could be used to find the stability of the classical ground state in $Tb_2Ti_2O_7$.

In Chapter 3 the effective Hamiltonian of $Tb_2Ti_2O_7$ was obtained. For a single cubic unit cell with 16 spins this effective Hamiltonian can be diagonalized. Using the eigenvalues and eigenstates of this effective Hamiltonian, some of the physical properties of $Tb_2Ti_2O_7$ such as specific heat could be calculated and compared with experiment.

If the proposed quantum spin ice state for $Tb_2Ti_2O_7$ was to be demonstrated, one could consider investigating $(Tb_{1-x}Dy_x)_2Ti_2O_7$ which may exhibit a quantum phase transition between a spin-ice and a spin liquid state as the concentration of $Dy^{3+}$ is decreased.

Applying a magnetic field along the [111] direction creates a kagomé in the classical spin ice system $Dy_2Ti_2O_7$ [69, 70]. Based on our calculations which show that $Tb_2Ti_2O_7$ is in the spin ice state, we propose that applying a magnetic field along [111] direction could create a quantum kagomé spin ice in $Tb_2Ti_2O_7$.

The experimental magnetization results along the [100], [110] and [111] show a strong isotropic behaviour. However, our results only capture parts of this isotropy. This suggests that other mechanisms are at play to recover such high level of isotropy in modrate applied magnetic field. Identifying these symmetry-restoration mechanism would be helpful in ultimately understanding the physics of $Tb_2Ti_2O_7$.

Finally, we close with a general comment. The key contribution of this thesis has been the identification of a "dynamically-induced" emergence of frustration in an effective quantum theory. It would be interesting to investigate the possible manifestation of this phenomena in other strongly correlated electron or quantum spin systems.

# Appendix A

# Exchange Couplings of $Ho_2Ti_2O_7$ and $Dy_2Ti_2O_7$

It was briefly mentioned in the introduction that while $Ho_2Ti_2O_7$ was the first proposed spin ice system, it has also been the most controversial [26, 40, 67]. On one hand, $\mu$SR, elastic and inelastic neutron scattering experiments [25] suggest a spin ice ground state for $Ho_2Ti_2O_7$ while on the other hand the observed sharp peak in specific heat experiment [41] and the derived exchange interaction from the DC susceptibility experiment would seem to suggest that $Ho_2Ti_2O_7$ is not a spin ice system [41]. It was shown that the observed Schottky anomaly in the specific heat data is related to the nuclear Schottky contribution. Subtracting off the contribution from the specific heat results, the derived magnetic specific heat result confirmed the spin ice state for $Ho_2Ti_2O_7$ [38].

However, the large antiferromagnetic exchange coupling derived from the high temperature DC susceptibility that predicted a non-spin-ice state has so far remained a puzzle. Specifically, fitting the Monte Carlo results for the specific heat to the experimental data [32] predicted a value for the exchange coupling three times less than that obtained via DC susceptibility measurements [41]. In this chapter we address this question and identify the source of this discrepancy between the exchange interaction derived from specific heat [38] and DC susceptibility measurements [41]. To proceed, we must discuss the high temperature behaviour of the DC

susceptibility. In the first section we formally derive the effective Hamiltonian for $Ho_2Ti_2O_7$ and $Dy_2Ti_2O_7$. In the second section we derive the DC susceptibility of a single crystal of $Ho_2Ti_2O_7$ and $Dy_2Ti_2O_7$ at high temperatures. We also calculate the Curie and Van Vleck terms of the DC susceptibility to assess their respective contribution to the high temperature part of the DC susceptibility. In the third section we present the experimental DC susceptibility results and give a comment on the importance of the demagnetization effect in these compounds. Using these experimental data, we calculate the exchange couplings of $Ho_2Ti_2O_7$ and $Dy_2Ti_2O_7$ and show that the derived exchange couplings are consistent with those previously obtained via analysis of specific heat data [38]. We conclude that using the wrong regime for high temperatures and the raw DC susceptibility data are the source of the large exchange coupling determined for $Ho_2Ti_2O_7$ [41], moreover, our results for exchange coupling of $Ho_2Ti_2O_7$ confirms the spin ice nature of $Ho_2Ti_2O_7$.

## A.1 Effective Hamiltonian of Spin Ice Systems

To determine quantitatively the effects of crystal field excited states on the low energy physics of $Ho_2Ti_2O_7$ and $Dy_2Ti_2O_7$, we calculate the effective Hamiltonian of these systems (Chapter 3). It has been well established that the total Hamiltonian in these compounds is the sum of the crystal field Hamiltonian plus dipole-dipole and exchange Hamiltonians. Hence the total Hamiltonian of these systems reads,

$$\begin{aligned} H &= H_{\rm cf} + \mathcal{J} \sum_{\langle ij \rangle} \mathbf{J}_i \cdot \mathbf{J}_j \\ &+ \mathcal{D} r_{\rm nn}^3 \sum_{i>j} \frac{\mathbf{J}_i \cdot \mathbf{J}_j}{|\mathbf{r}_{ij}|^3} - \frac{3(\mathbf{J}_i \cdot \mathbf{r}_{ij})(\mathbf{J}_j \cdot \mathbf{r}_{ij})}{|\mathbf{r}_{ij}|^5} \,, \end{aligned} \tag{A.1}$$

where $H_{\rm cf}$ is the crystal field Hamiltonian of $Dy_2Ti_2O_7$ and $Ho_2Ti_2O_7$, $\mathcal{J}$ is the exchange coupling, $\mathcal{D}$ is the dipolar coupling at first nearest neighbor, $\mathbf{J}_i$ is the total angular momentum operator equal to 8 and $\frac{15}{2}$ respectively for $Ho_2Ti_2O_7$ and $Dy_2Ti_2O_7$, and $\mathbf{r}_{ij}$ is the position vector between ions $i$ and $j$. We showed in Chapter 2 that the ground state of $Ho_2Ti_2O_7$ is a doublet with zero matrix elements between these two states and the first excited state is separated by a large gap of about 250

K from the ground state. In contrast to $Ho_2Ti_2O_7$, $Dy_2Ti_2O_7$ has a very small $J^z$ matrix elements between the two states that form the ground state doublet and the first excited state is separated by a 380 K gap from the ground state. However, this off-diagonal $J^z$ matrix element is 100 times less than the diagonal $J^z$ matrix elements. Hence, for our purpose, we assume that in both of these compounds the off-diagonal angular momentum matrix elements within the ground state doublet are zero. We consider the two states of the ground state doublet as the model space and we apply the effective Hamiltonian method (Section 3.3) to derive an effective Hamiltonian in this manifold of states. The effective Hamiltonian for a degenerate ground state to second order is,

$$H_{\text{eff}} = PVP + PVRVP \,, \tag{A.2a}$$

$$P = \sum_{\{k\}} |\Phi_{0,\{k\}}\rangle\langle\Phi_{0,\{k\}}| \,, \tag{A.2b}$$

$$R = \sum_{\{n\},\{m\}} \frac{|\Phi_{\{n\},\{m\}}\rangle\langle\Phi_{\{n\},\{m\}}|}{(E^0 - E^n)} \,, \tag{A.2c}$$

where $V$ is the dipole-dipole and exchange interactions, sum on $\{k\}$ is over all the many-body crystal field ground states and sum on $\{n\}$ and $\{m\}$ is over all the many-body crystal field excited states and $|\Phi_{0,\{k\}}\rangle$, $|\Phi_{n,\{m\}}\rangle$, $E^0$ and $E^n$ are defined as follow,

$$|\Phi_{0,\{k\}}\rangle = \prod_{i=1}^{N} |\phi_{i,0}^{(k_i)}\rangle \,, \tag{A.3a}$$

$$|\Phi_{\{n\},\{m\}}\rangle = \prod_{i=1;\sum n_i \neq 0}^{N} |\phi_{i,n_i}^{(m_i)}\rangle \,, \tag{A.3b}$$

$$E^n = \sum_i E_i^{n_i} \tag{A.3c}$$

where $|\phi_{i,0}^{k_i}\rangle$ is the $k_i^{th}$ state of the crystal field ground state for site $i$, $|\phi_{i,n_i}^{(k_i)}\rangle$ is the $k_i^{th}$ state of the $n_i$ level of crystal field state for site $i$, $E_i^{n_i}$ is the energy of the $n_i^{th}$ crystal field excited states. Multiplication is over all magnetic ions in the crystal and $\sum n_i \neq 0$ imposes that at least one of the ions in the system is in the excited crystal field state. Because of the zero matrix elements between two states of the

crystal field ground state doublet, these two states can be mapped out to the two states of an Ising spin with local $\langle 111\rangle$ axis as the Ising axis. Hence, to the first order, the effective Hamiltonian of $Ho_2Ti_2O_7$ and $Dy_2Ti_2O_7$ reads,

$$\begin{aligned} H^{\text{eff}} &= -J\sum_{\langle ij\rangle}\mathbf{S}_i^{z_i}\cdot\mathbf{S}_j^{z_j} \\ &+ Dr_{\text{nn}}^3\sum_{i>j}\frac{\mathbf{S}_i^{z_i}\cdot\mathbf{S}_j^{z_j}}{|\mathbf{r}_{ij}|^3}-\frac{3(\mathbf{S}_i^{z_i}\cdot\mathbf{r}_{ij})(\mathbf{S}_j^{z_j}\cdot\mathbf{r}_{ij})}{|\mathbf{r}_{ij}|^5}\,, \end{aligned} \tag{A.4}$$

where $J=\mathcal{J}|\langle J^z\rangle|^2$ ($\langle J^z\rangle$ is the diagonal $J^z$ matrix element in the ground state doublet) is the effective exchange coupling, $D=\mathcal{D}|\langle J^z\rangle|^2$ is the effective dipole-dipole coupling and $\mathbf{S}_i^{z_i}$ is the Ising spin at site $i$ with $z$ direction towards the local $\langle 111\rangle$ direction. In second order perturbation theory, the change in physical quantities varies as one over the gap between the crystal field ground state and first excited state ($\frac{1}{E^{(0)}-E^{(n)}}$) and because this gap is very large for $Ho_2Ti_2O_7$ and $Dy_2Ti_2O_7$, this term is much smaller than the first order perturbation term. Numerical calculations confirm this prediction and the effective Hamiltonian of $Ho_2Ti_2O_7$ and $Dy_2Ti_2O_7$ is indeed described by Hamiltonian (A.4).

In Hamiltonian (A.4) the exchange $J$ and the dipole-dipole $D$ couplings are yet to be determined. In what follows we express the dipole-dipole coupling in terms of $D_{\text{nn}}=\frac{5D}{3}$ which is the strength of the dipole-dipole interaction between local $\langle 111\rangle$ Ising spin at nearest neighbor (Section 1.2). We start by calculating the dipole-dipole coupling. The dipole-dipole coupling at the first nearest neighbor reads,

$$D_{\text{nn}} = \frac{5}{3}(\frac{\mu_0}{4\pi})\frac{(g\mu_{\text{B}}|\langle J^z\rangle|)^2}{r_{\text{nn}}^3}\,, \tag{A.5}$$

where $\mu_0$ is the vacuum permeability equal to $4\pi\times10^{-7}$ H/m, $g$ is the Landé factor equal to $\frac{5}{4}$ for $Ho_2Ti_2O_7$ and $\frac{4}{3}$ for $Dy_2Ti_2O_7$, $r_{\text{nn}}=\frac{\sqrt{2}a}{4}$ is the nearest-neighbor distance between magnetic ions ($a$ is size of conventional cubic unit cell) respectively equal to 3.579 Å [36] , and 3.573 Å [68], for $Dy_2Ti_2O_7$ and $Ho_2Ti_2O_7$, and $|\langle J^z\rangle|$ is the diagonal matrix element of $J^z$ in the ground state equal to 7.4043 and 7.7604 (these values obtained using the crystal field parameters of $Ho_2Ti_2O_7$ in Ref. [35]) for $Dy_2Ti_2O_7$ and $Ho_2Ti_2O_7$, respectively. By substituting the proper values of each

quantity in Eq. (A.5) we obtain $D_{\rm nn}$=2.142 K and $D_{\rm nn}$= 2.207 K, respectively, for $Ho_2Ti_2O_7$ and $Dy_2Ti_2O_7$. The observed difference between these values of $D_{\rm nn}$ and the reported values in other references [26,32,41] is related to the different values of $r_{\rm nn}$ and $\langle J^z \rangle$ used in this calculation. All other references [26,32,41] used $r_{\rm nn}$=3.54 Å for both $Ho_2Ti_2O_7$ and $Dy_2Ti_2O_7$ and $\langle J^z \rangle$ equal to 8 and $\frac{15}{2}$ respectively for $Ho_2Ti_2O_7$ and $Dy_2Ti_2O_7$, which were the first reported values for these quantities to derive the $D_{\rm nn}$ dipole-dipole couplings. However, in this calculation we used the most accurate and newly reported values of $r_{\rm nn}$ and $\langle J^z \rangle$ and we derived a slightly different, and likely more accurate, value for $D_{\rm nn}$.

While $D_{\rm nn}$ can be determined by the intrinsic properties of a single magnetic ion, $J$ depends on the overlap of $f$ orbitals and other quantum effects and hence is very difficult to calculate it by *ab-initio* methods. Therefore, semi-empirical methods have been developed to derive the exchange interaction from the experimental results. In this work we use the experimental high temperature DC susceptibility results of $Ho_2Ti_2O_7$ and $Dy_2Ti_2O_7$ to determine the exchange couplings for these two compounds.

## A.2 High Temperature Expansion of DC Susceptibility for Spin Ice Systems

In the previous section we derived the effective Hamiltonian of $Ho_2Ti_2O_7$ and $Dy_2Ti_2O_7$ with the unknown dipole-dipole and exchange couplings and we determined the dipole-dipole couplings of these compounds. In this section we calculate the exchange coupling of $Ho_2Ti_2O_7$ and $Dy_2Ti_2O_7$ using the high temperature DC susceptibility.

It was discussed in the previous section that the effective Hamiltonian of spin ice systems $Ho_2Ti_2O_7$ and $Dy_2Ti_2O_7$ at low temperatures is made of local $\langle 111 \rangle$ Ising spins. We use this assumption to calculate the high temperature DC susceptibility of these systems and later, comment on the validity of this effective Hamiltonian

at high temperatures. The DC susceptibility of a spin ice system reads,

$$\chi^{\alpha\gamma}(T) = \frac{{g_s}^2{\mu_{\rm B}}^2\langle J^z\rangle^2}{k_{\rm B}T}\sum_{i>j}\frac{\langle S_i^\alpha S_j^\gamma e^{(-\beta H^{\rm eff})}\rangle}{\langle e^{(-\beta H^{\rm eff})}\rangle}\,, \tag{A.6}$$

where $k_{\rm B}$ is the Boltzmann's constant, $T$ is the temperature, $\beta{=}\frac{1}{k_{\rm B}T}$, $H^{\rm eff}$ is the Hamiltonian of the system given by Eq. (A.4), $S_i^\alpha$ is the $\alpha$ component of Ising spin at site $i$ in the global axis and the sum is over all Ising spins in the system. Because of the cubic symmetry of the pyrochlore lattice, the DC susceptibility is a coefficient of identity matrix. Based on this fact, the DC susceptibility of these compounds in the [100], [110], [111] directions and polycrystalline should be equal to the DC susceptibility in [001] direction. Hence, we calculate the high temperature part of Eq. (A.6) for the [001] direction, and this expansion, to first order reads,

$$\chi(T) = \frac{N_0(g_s\mu_{\rm B})^2(\langle J^z\rangle)^2}{3k_{\rm B}T}[1+\frac{3}{k_{\rm B}T}(0.545D_{\rm nn}+0.67J_{\rm nn})]\,, \tag{A.7}$$

where, $N_0$ is the Avogadro number, $\mu_{\rm B}$ is the Bohr magneton, $D_{\rm nn}$ is the nearest neighbor dipole-dipole coupling defined in Eq. (A.5) and $J_{\rm nn}=\frac{J}{3}$. To derive Eq. (A.7) we chose the direction of four easy axis related to four sublattices in the global frame as $\frac{1}{\sqrt{3}}(1,1,1)$, $\frac{1}{\sqrt{3}}(-1,-1,1)$, $\frac{1}{\sqrt{3}}(1,-1,-1)$ and $\frac{1}{\sqrt{3}}(-1,1,-1)$. The first term in the susceptibility is $\sum_{ij}n_i^zn_j^z$ which is non-zero when $i$ is equal to $j$. Calculating this sum gives $\frac{N}{3}$, where $N$ is the number of magnetic ions in the system. To calculate the next sum we need to calculate $n_i^zn_j^zn_k^\alpha n_l^\alpha$ which is non-zero when $k$ is $i$ and $l$ is $j$ or, $l$ is $i$ and $k$ is $j$ with the condition that $i\neq j$. Using the fact that $n_i^\alpha n_j^\alpha$ is always $\frac{-1}{3}$, independent of the sublattices, this sum reduces to sum over $n_i^zn_j^z$ which is $\frac{-2}{3}$ for a given $i$. Hence, summing over all the particles, the coefficient of exchange interaction is $\frac{2}{9}N$ or in terms of $J_{\rm nn}$, $\frac{2}{3}N$. To accomplish the sum over the dipole-dipole interaction we use the cut off and Ewald methods to calculate the dimensionless coefficient $-\frac{3}{5D}D_{ij}^{\alpha\beta}n_i^\alpha n_j^\beta n_i^zn_j^z$, which is written down in the unit of $D_{\rm nn}=\frac{5D}{3}$. In Fig. A.1 we plot this coefficient as a function of cut-off radius and we observe that this coefficient converges to 0.545. This is consistent with the coefficient obtained by the Ewald method. Eq. (A.7) is only valid for high temperatures where, firstly, all the states of Hamiltonian (A.4) are thermally accessible and $\chi(T)$ is a linear function of $\frac{1}{T}$ while secondly, the

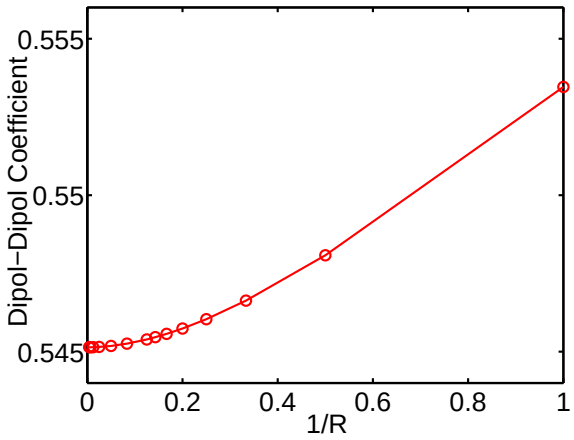


Figure A.1: The coefficient in front of the dipole-dipole coupling in Eq. (A.7) as a function of 1/R, where R is the cut-off distance in the unit of cubic unit cell.

effective Hamiltonian is valid. The validity of the effective Hamiltonian is based on the fact that the thermal populations of the crystal field excited states ought to be negligible and the magnetic moments must behave as Ising spins. Therefore, we need to find a region of temperatures where both these criteria are valid. From an experimental point of view, the linear part of the DC susceptibility can be interpreted as the high temperature regime for the Ising spins. However, we have to verify that in this region of temperature, the effect of the excited crystal field states are small. To accomplish this, we calculate the Curie and Van Vleck terms of the DC susceptibility originating form the excited crystal field states of $Ho_2Ti_2O_7$ and $Dy_2Ti_2O_7$. Notice that from now on we use the wording "Curie term" for the permanent moment contribution from the excited crystal field states. The Curie and Van Vleck terms of the DC susceptibility are given by [61],

$$\chi^{(\text{VanVleck})}_{i\alpha\beta} = \sum_{\mu\nu}^{E_\mu \neq E_\nu} \frac{\langle\nu|J_{i\alpha}|\mu\rangle\langle\mu|J_{i\beta}|\nu\rangle}{E_\mu - E_\nu}(n_\nu - n_\mu)\ , \tag{A.8a}$$

$$\chi^{(\text{Curie})}_{i\alpha\beta} = \frac{1}{k_\text{B}T}\sum_{\mu\nu,\{\mu,\nu\}\neq 0}^{E_\mu = E_\nu} \langle\nu|J_{i\alpha}|\mu\rangle\langle\mu|J_{i\beta}|\nu\rangle n_\nu - \frac{1}{k_\text{B}T}\langle J_{i\alpha}\rangle\langle J_{i\beta}\rangle, \tag{A.8b}$$

where $E_\mu$ is an eigenstate of the crystal field Hamiltonian, $J_{i\alpha}$ is the $\alpha$ component

of the total angular momentum of ion $i$, $n_\mu = \frac{e^{(-\beta E_\mu)}}{Z}$ is the population of the state $\mu$ at temperature $T$, $\beta = \frac{1}{k_B T}$. The condition $\{\mu, \nu\} \neq 0$ in the Curie term confirms that the sum in this term is over the excited states and the sum on $\mu$ and $\nu$ is over all the eigenstates of the crystal field Hamiltonian of the system. In this calculation we used the crystal field parameters of $Ho_2Ti_2O_7$ given in Ref. [35] to calculate crystal field Hamiltonian of $Ho^{3+}$. By rescaling the crystal field parameters [62] of $Ho_2Ti_2O_7$ we obtain the crystal field parameters of $Dy_2Ti_2O_7$. Diagonalizing these crystal field Hamiltonians we calculate their eigenvalues and eigenstates. We used these crystal field states to calculate the Curie and the Van Vleck terms of the DC susceptibility. In Fig. A.2 we show the result of this calculation by plotting $\chi T$ as a function of $\frac{1}{T}$ for Curie and Van Vleck susceptibilities of $Ho_2Ti_2O_7$ and $Dy_2Ti_2O_7$.

The high temperature DC susceptibility in this section can be used to calculate the exchange coupling in the spin ice systems $Ho_2Ti_2O_7$ and $Dy_2Ti_2O_7$. To accomplish this, we determine the slope of the linear part of the experimental DC susceptibility and, by fitting the theoretical slope to this slope we find the exchange coupling. To confirm that the effect of crystal field excited states are indeed negligible, we show that in the linear high temperature regime of the DC susceptibility the Curie and the Van Vleck terms coming from the crystal field excited states make negligible contribution compared to the experimental DC susceptibility data.

## A.3 Exchange Couplings of $Ho_2Ti_2O_7$ and $Dy_2Ti_2O_7$

In this section we present the experimental DC susceptibility results of $Ho_2Ti_2O_7$ and $Dy_2Ti_2O_7$, in order to determine the exchange couplings for both compounds. We accomplish this with specifying the proper high temperature regime of the DC susceptibility, and using the calculated high temperature DC susceptibility results of the previous section, we derive the exchange couplings of these compounds.

The experimental DC susceptibility results were provided to us by Dr. Ryuji Higashinaka and Prof. Yoshi Maeno from Kyoto University. In their measurements, they used two distinct single crystals for each compound and the DC susceptibility were measured along the high symmetry directions [100], [110] and [111] with an

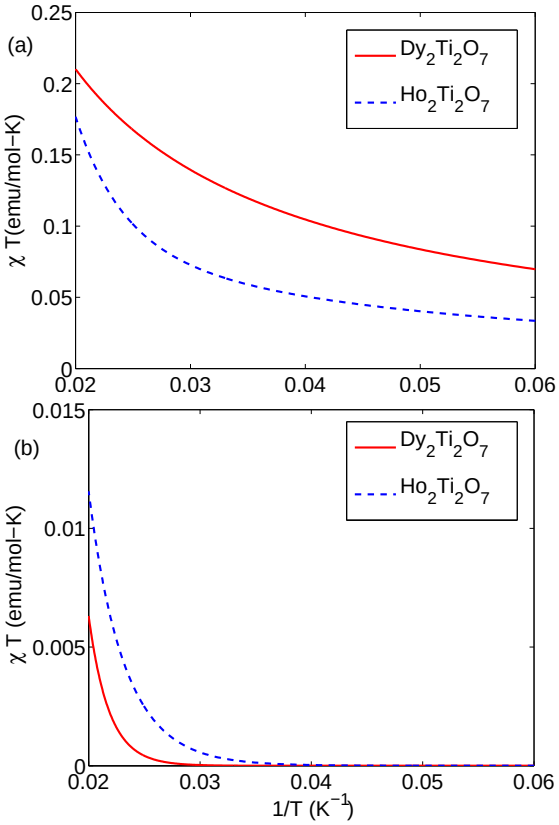


Figure A.2: (a) The Van Vleck term and (b) the Curie term of the DC susceptibility of $Ho_2Ti_2O_7$ and $Dy_2Ti_2O_7$ as a function of $\frac{1}{T}$. The displayed Curie term is from the crystal field excited states (The contribution from the crystal field ground state is not included).

applied magnetic field of $B$=0.01 T. We label the data related to each single crystal of $Ho_2Ti_2O_7$ and $Dy_2Ti_2O_7$ by set 1 and set 2. In Fig. A.3 and Fig A.4 we demonstrate plots of $\chi T$ as a function of $\frac{1}{T}$, where here $\chi$ is the raw DC susceptibility data of $Ho_2Ti_2O_7$ and $Dy_2Ti_2O_7$ for the two sets of data.

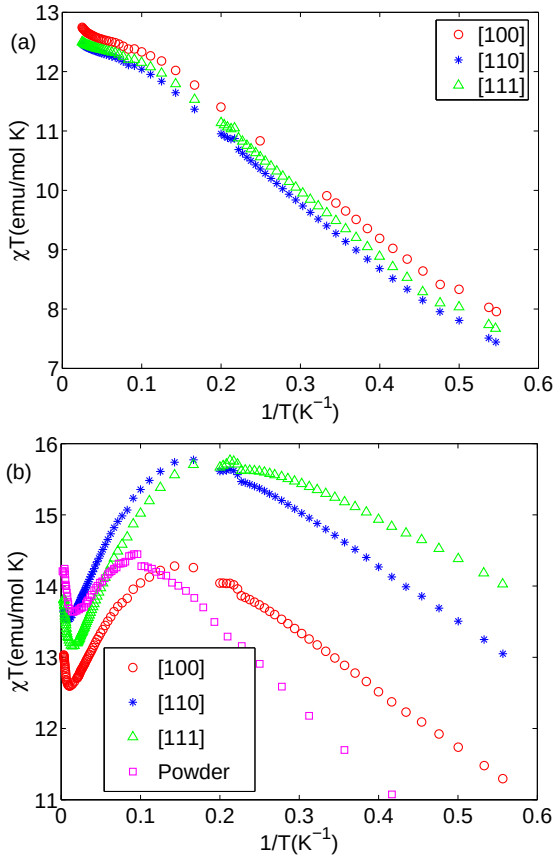


Figure A.3: Raw DC susceptibility data of $Dy_2Ti_2O_7$ (a) and $Ho_2Ti_2O_7$ (b) for a field of $B$=0.01 T along the [100], [110] and [111] directions from data set 1. Powder DC susceptibility data of $Ho_2Ti_2O_7$ is from Ref. [41].

Two linear regimes are observed in these data sets, one between the range of $T$=2 K to $T$=5 K and the other one between $T$=15 K to $T$=35 K. We respectively call these two ranges of temperatures low-temperature linear regime and high-temperature linear regime. However, because of the following reason we can not use these results as the real DC susceptibility of $Ho_2Ti_2O_7$ and $Dy_2Ti_2O_7$ to

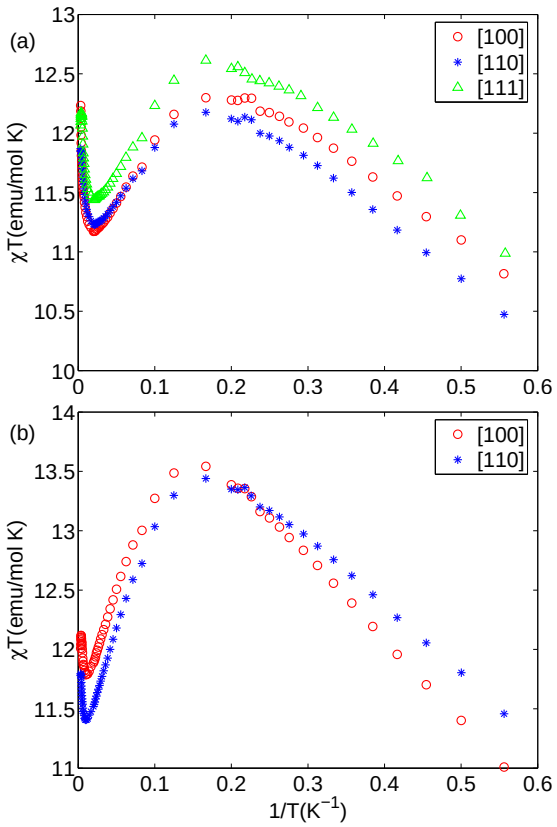


Figure A.4: Raw DC susceptibility data of $Dy_2Ti_2O_7$ (a) and $Ho_2Ti_2O_7$ (b) for a field of $B$=0.01 T along the [100], [110] and [111] directions for $Dy_2Ti_2O_7$ and, [100] and [110] directions for $Ho_2Ti_2O_2$ from data set 2.

calculate the exchange coupling; it turns out that due to the large magnetic moments of $Ho^{3+}$ and $Dy^{3+}$ demagnetization effects in $Ho_2Ti_2O_7$ and $Dy_2Ti_2O_7$ are important [25]. Hence, the experimental DC susceptibility data has to be corrected for demagnetization effects. In Fig. A.5 and Fig. A.6 we use the demagnetization corrected results of the DC susceptibility ($\chi$) to plot $\chi T$ as a function of $\frac{1}{T}$ for $Ho_2Ti_2O_7$ and $Dy_2Ti_2O_7$ for the two data sets.

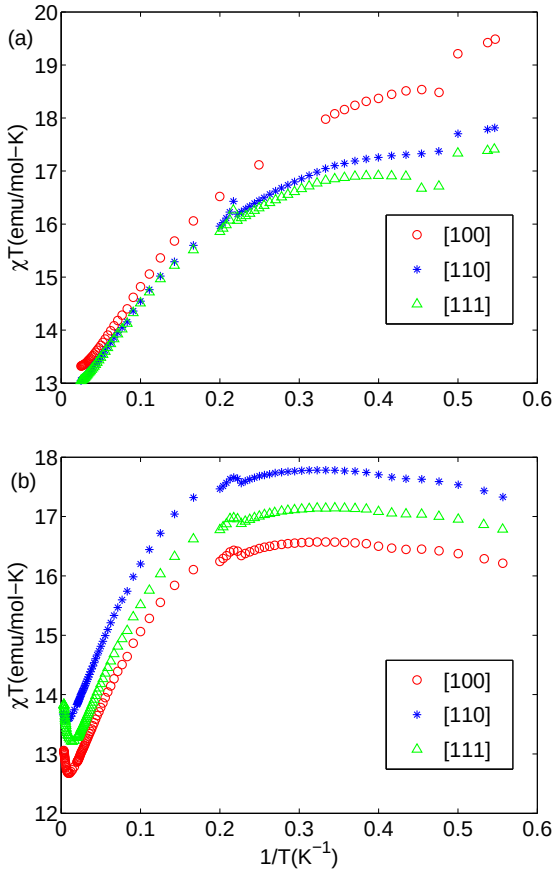


Figure A.5: Demagnetization corrected DC susceptibility data for $Dy_2Ti_2O_7$ (a) and $Ho_2Ti_2O_7$ (b) along the [100], [110] and [111] directions from data Set 1.

These plots show only one linear regime at high temperatures (between 15 K to 35 K) with no other linear regime at low temperatures. Hence, it would appear that the observed linear region at low temperatures in the raw data (Fig. A.3 and Fig. A.4) is an artifact of demagnetization effect. As a result, we conclude

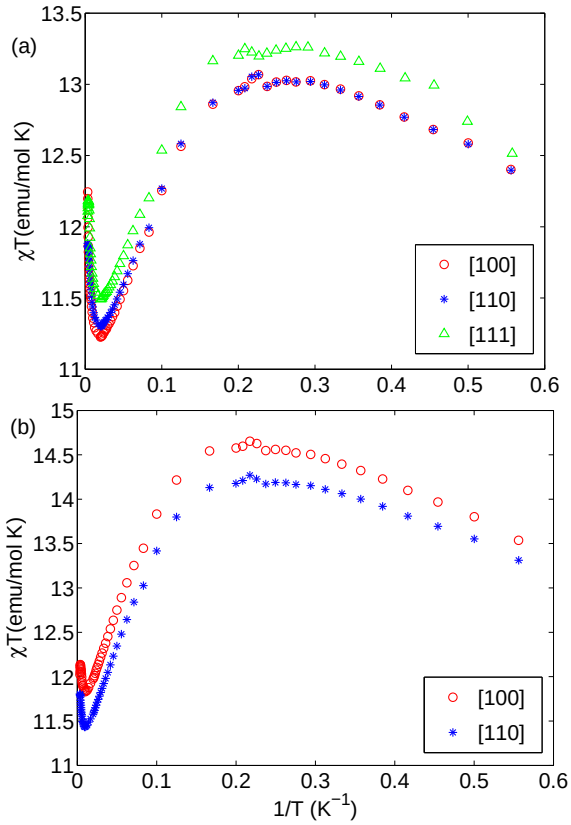


Figure A.6: Demagnetization corrected DC susceptibility data for $Dy_2Ti_2O_7$ (a) and $Ho_2Ti_2O_7$ (b) along the [100], [110] and [111] directions for $Ho_2Ti_2O_7$ and, [100] and [110] directions for $Dy_2Ti_2O_7$ from data Set 2.

that the high-temperature linear regime, is in fact the real linear high temperature regime of spin ice systems $Ho_2Ti_2O_7$ and $Dy_2Ti_2O_7$. We use this linear regime to determine the exchange coupling in $Ho_2Ti_2O_7$ and $Dy_2Ti_2O_7$. Comparing the value of the Curie and Van Vleck terms of the DC susceptibility, arising from the crystal field excited states (Fig. A.2), with the value of the DC susceptibility in the linear regime reveals that Curie and Van Vleck terms are negligible compared to the linear regime of DC susceptibility.

In Fig. A.7 and Fig. A.8, we respectively plot the high-temperature linear part of the demagnetization-corrected DC susceptibility of $Ho_2Ti_2O_7$ and $Dy_2Ti_2O_7$ for set 1 and set 2 of data and high symmetry directions for fields applied along the [100], [110] and [111].

Determining the slope of these lines and fitting them to the theoretical slope $N(g\mu_B)^2\langle J^z\rangle^2$ $(0.54D_{nn} + 0.67J_{nn})$, we derive the exchange couplings of $Ho_2Ti_2O_7$ and $Dy_2Ti_2O_7$. The exchange couplings for different directions are almost the same and we take the average of these couplings as the exchange coupling of $Ho_2Ti_2O_7$ and $Dy_2Ti_2O_7$. In Table 1 we report the average Curie temperature, the dipole-dipole couplings and exchange couplings for $Ho_2Ti_2O_7$ and $Dy_2Ti_2O_7$ for both data set 1 and data set 2. The obtained exchange couplings for $Ho_2Ti_2O_7$ and $Dy_2Ti_2O_7$ are in agreement, within an acceptable error, with the derived exchange couplings obtained from fitting the Monte Carlo results for the specific heat to the experimental data [38]. The previously reported exchange coupling of $Ho_2Ti_2O_7$ in Reference [41], derived from the DC susceptibility results was $J_{nn}$=-1.92 K, which is not consistent with our results. The sources of error in that work are: first, using the raw data of the DC susceptibility as opposed to demagnetization-corrected data; second, choosing the wrong region of high temperature in the experimental data. Using the raw data of set 1 (Figs. A.3) and the same region of high temperature as Reference [41] we obtain $J_{nn} = -2.12$ K for $Ho_2Ti_2O_7$ and $J_{nn} = -2.26$ K for $Dy_2Ti_2O_7$ from data set 1. Using these values of exchange couplings and the phase diagram for $\langle 111\rangle$ Ising spins on the pyrochlore lattice [32], one would have wrongly concluded that both $Ho_2Ti_2O_7$ and $Dy_2Ti_2O_7$ should be in the all-in/all-out ordered phase, which is inconsistent with the experimental results.

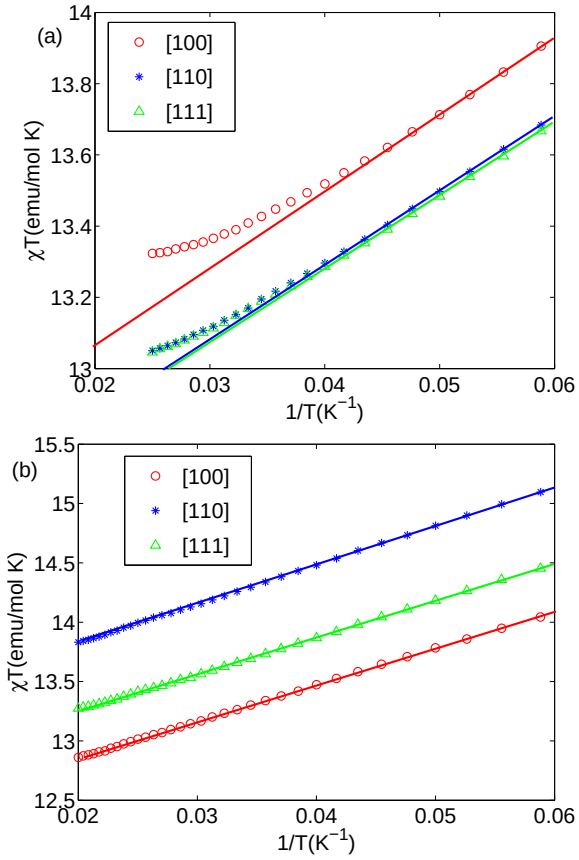


Figure A.7: Linear part of the DC susceptibility (demagnetization corrected) for $Dy_2Ti_2O_7$ (a) and $Ho_2Ti_2O_7$ (b) along the [100], [110] and [111] directions from data Set 1.

| | $Ho_2Ti_2O_7$ | | | $Dy_2Ti_2O_7$ | | |
|---|---|---|---|---|---|---|
| | $\theta_C$ (K) | $D_{\rm nn}$ (K) | $J_{\rm nn}$ (K) | $\theta_C$ (K) | $D_{\rm nn}$ (K) | $J_{\rm nn}$ (K) |
| Set 1 | 2.5 | 2.142 | -0.50 | 1.4 | 2.207 | -1.08 |
| Set 2 | 2.2 | 2.142 | -0.646 | 1.14 | 2.207 | -1.225 |

Table A.1: The derived Curie-Weiss temperature ($\theta_C$) from the experimental results and the calculated dipole-dipole ($D_{\rm nn}$) and exchange ($J_{\rm nn}$) couplings of $Ho_2Ti_2O_7$ and $Dy_2Ti_2O_7$ .

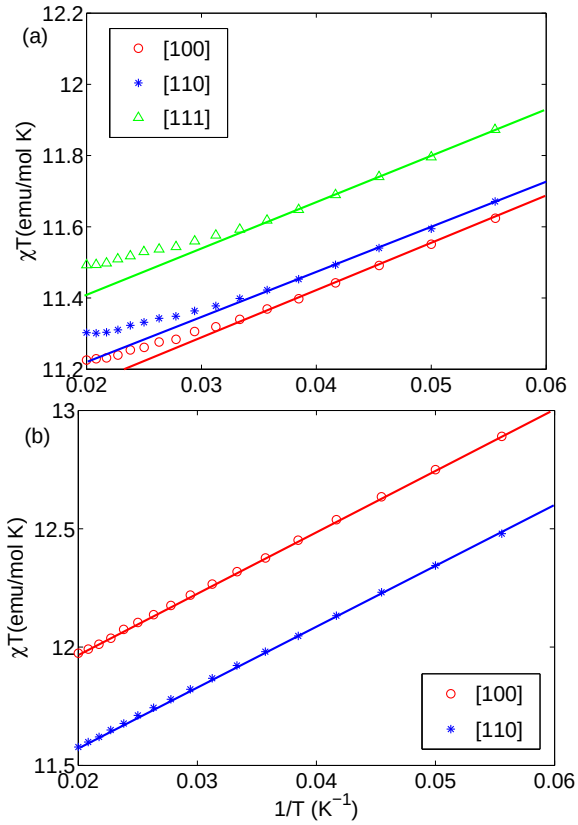


Figure A.8: Linear part of the DC susceptibility (demagnetization corrected) for $Dy_2Ti_2O_7$ (a) and $Ho_2Ti_2O_7$ (b) along the [100], [110] and [111] directions for $Ho_2Ti_2O_7$ and, [100] and [110] directions for $Dy_2Ti_2O_7$ from data set 2.

## A.4 Summary

In conclusion, we presented results aimed at determining the exchange coupling of the spin ice materials $Ho_2Ti_2O_7$ and $Dy_2Ti_2O_7$ using the high temperature expansion of the DC susceptibility to second order in $\frac{1}{T}$. Using the Rayleigh-Schrödinger perturbation theory, we derived an effective Hamiltonian for spin ice systems and showed that this Hamiltonian is indeed that of local $\langle 111 \rangle$ Ising spins.

We calculated the high temperature DC susceptibility of spin ice systems. In order to properly identify the effects and contributions from the excited crystal field states, we derived the Curie and Van Vleck terms of the DC susceptibility arising from those crystal field excited states. We presented raw and demagnetization-corrected experimental DC susceptibility data for $Ho_2Ti_2O_7$ and $Dy_2Ti_2O_7$ with two samples for each compound. We showed that the demagnetization effects in spin ice systems are important and using raw data leads to wrong estimates of $J_{\rm nn}$. By specifying the high temperature regime of the demagnetization corrected DC susceptibility, we determined the exchange couplings of $Ho_2Ti_2O_7$ and $Dy_2Ti_2O_7$. The obtained exchange couplings for $Ho_2Ti_2O_7$ and $Dy_2Ti_2O_7$ are consistent with the estimated exchange couplings based on fitting the Monte Carlo simulations to the experimental specific heat [32, 38]. To determine the incorrectness of the result of Reference [41], we used raw DC susceptibility data (Set 1) and the similar region of temperature used in Reference [41] to derive dramatically wrong exchange couplings for both spin ice systems $Ho_2Ti_2O_7$ and in particular, $Dy_2Ti_2O_7$, which is in dramatic contrast with the value found in Ref. [34].

# Appendix B

# Stevens Operator of $Tb_2Ti_2O_2$

Stevens operators in terms of the total angular momentum **J** operator. $J$ is the magnitude of **J** and $J_+$ and $J_-$ are, respectively, the raising and lowering operators [58, 59].

$$
\begin{aligned}
O_2^0 &= 3J_z^2 - J(J+1) && \text{(B.1a)}\\
O_2^2 &= \frac{1}{2}(J_+^2 + J_-^2) && \text{(B.1b)}\\
O_4^0 &= 35J_z^4 - 30J(J+1)J_z^2 + 25J_z^2 - 6J(J+1) + 3J^2(J+1) && \text{(B.1c)}\\
O_4^3 &= \frac{1}{4}[J_z(J_+^3 + J_-^3) + (J_+^3 + J_-^3)J_z] && \text{(B.1d)}\\
O_6^0 &= 231J_z - 315J(J+1)J_z^4 + 735J_z^4 + 105J^2(J+1)^2J_z \\
&- 525J(J+1)J_z^2 + 294J_z^2 - 5J^3(J+1)^3 + 40J^2(J+1)^2 \\
&- 60J(J+1) && \text{(B.1e)}\\
O_6^3 &= \frac{1}{4}(11J_z^3 - 3J(J+1)J_z - 59J_z)(J_+^3 + J_-^3) \\
&+ (J_+^3 + J_-^3)(11J_z^3 - 3J(J+1)J_z - 59J_z) && \text{(B.1f)}\\
O_6^6 &= \frac{1}{2}(J_+^6 + J_-^6) && \text{(B.1g)}
\end{aligned}
$$

# Appendix C

# Local Basis Vector

In this appendix we introduce the local frame of basis for the four sublattices we use in our calculation in the global axis of frame. The transformation matrix from the global frame to the local frame in terms of vecrors $v$ is: $u = [v'^x v'^y v'^z]$, where $v^z(a)'$ is the transpose of vector $v^z(a)$.

$v^x(1) = \frac{1}{\sqrt{6}}(\bar{1}, \bar{1}, 2)$, $v^y(1) = \frac{1}{\sqrt{2}}(1, \bar{1}, 0)$, $v^z(1) = \frac{1}{\sqrt{3}}(1, 1, 1)$.

$v^x(2) = \frac{1}{\sqrt{6}}(1, 1, 2)$, $v^y(2) = \frac{1}{\sqrt{2}}(\bar{1}, 1, 0)$, $v^z(2) = \frac{1}{\sqrt{3}}(\bar{1}, \bar{1}, 1)$.

$v^x(3) = \frac{1}{\sqrt{6}}(\bar{1}, 1, \bar{2})$, $v^y(3) = \frac{1}{\sqrt{2}}(1, 1, 0)$, $v^z(3) = \frac{1}{\sqrt{3}}(1, \bar{1}, \bar{1})$.

$v^x(4) = \frac{1}{\sqrt{6}}(1, \bar{1}, \bar{2})$, $v^y(4) = \frac{1}{\sqrt{2}}(\bar{1}, \bar{1}, 0)$, $v^z(4) = \frac{1}{\sqrt{3}}(\bar{1}, 1, \bar{1})$.

# Bibliography


[1] A. P. Ramirez, *"Geometric frustration: Magic moments"*, Nature **421**, 483 (2003).

[2] R. Jain, K. Kabir, J. B. Gilroy, K. A. R. Mitchell, K.-C Wong and R. G. Hicks, *"High-temperature metal organic-magnets"*, Nature **445**, 291 (2007).

[3] G. Ernst, C. Broholm, G. R. Kowach and A. P. Ramirez, *"Phonon density of states and negative thermal expansion in $ZrW_2O_8$"*, Nature **396**, 147 (1998).

[4] D. Spergel and, Ue-Li Pen, *"Cosmology in a string-dominated universe"*, *Astrophys. J.* **491** L67-L71, (1997).

[5] D. Bernal and R. H. Fowler, *"A theory of water and ionic solution, with particular reference to hydrogen and hydroxyl ions"*, J. Chem. Phys. **1**, 515 (1933).

[6] W.F. Giauque and M. F. Ashley, *"Molecular rotation in ice at 10* K. *Free energy of formation and entropy of water"*, Phys. Rev. **43**, 81 (1933).

[7] W.F. Giauque and J. W. Stout, *"The entropy of water and the third law of thermodynamics. The heat capacity of ice from 15 to 273* K*"*, J. American Chem. Soc. **58**, 1144 (1936).

[8] L. Pauling, *"The structure and entropy of ice and of other crystals with some randomness of atomic arrangement"*, J. American Chem. Soc. **57**, 2680 (1935).

[9] K.H. Fischer and J.A. Hertz, *"Spin Glasses"*, Cambridge University Press (1991).

[10] M. Mezard, G. Parisi, M. A. Virasoro, *"Spin Glass Theory and Beyond"* , World Scientific (1987).

[11] J. A. Mydosh, *"Spin Glasses"*, Taylor and Francis (1995).

[12] K. Binder and A. P. Young, *"Spin glasses: Experimental facts, theoretical concepts, and open questions"*, Rev. Mod. Phys. **58**, 801(1986).

[13] H. T. Diep, *"Frustrated Spin Systems"*, World Scientific (2004).

[14] G. H. Wannier, *"Antiferromagnetism. The triangular Ising net"*, Phys. Rev. **79**, 357 (1950).

[15] J. N. Reimers, A. J. Berlinsky, and A.-C. Shi, *"Mean-field approach to magnetic ordering in highly frustrated pyrochlores"*, Phys. Rev. B. **43**, 865 (1991).

[16] R. Moessner and J. T. Chalker, *"Properties of a classical spin liquid: The Heisenberg pyrochlore antiferromagnet"*, Phys. Rev. Lett. **80**, 2929 (1998).

[17] B. Canals and, C. Lacroix, *"Pyrochlore antiferromagnet: A three-dimensional quantum spin liquid"*, Phys. Rev. Lett. **80**, 2933 (1998).

[18] R. Moessner and, J. Berlinsky, *"Magnetic susceptibility of diluted pyrochlore and* $SrCr_{9-9x}Ga_{3+9x}O_{19}$ *antiferromagnets"*, Phys. Rev. Lett. **83**, 3293 (1999).

[19] P. Schiffer and A. P. Ramirez, *"Recent experimental progress in the study of geometrical magnetic frustration"*, Comments Condens. Matter Phys. **10**, 21 (1996).

[20] S.-H. Lee, C. Broholm, T. H. Kim, W. Ratcliff, and S-W Cheong, *"Local spin resonance and spin-Peierls-like phase transition in a geometrically frustrated antiferromagnet."*, Phys. Rev. Lett. **84**, 3718 (2000).

[21] O. Tchernyshyov, R. Moessner, and S. L. Sondhi, *"Order by distortion and string modes in pyrochlore antiferromagnets"*, Phys. Rev. Lett. **88**, 067203 (2002).

[22] O. Tchernyshyov, R. Moessner, and S. L. Sondhi, *"Spin-Peierls phases in pyrochlore antiferromagnets"*, Phys. Rev. B **66**, 064403 (2002).

[23] S.-H. Lee, C. Broholm, W. Ratcliff, G. Gasparovic, T. H. Kim, Q. Huang, and S.-W. Cheong, *"Emergent excitations in a geometrically frustrated magnet"*, Nature **418**, 856 (2002).

[24] M. J. P. Gingras, C. V. Stager, N. P. Raju, B. D. Gaulin, and J. E. Greedan, *"Static critical behavior of the spin-freezing transition in the geometrically frustrated pyrochlore antiferromagnet $Y_2Mo_2O_7$"*, Phys. Rev. Lett. **78**, 947 (1997).

[25] M. J. Harris, S. T. Bramwell, D. F. McMorrow, T. Zeiske, and K. W. Godfrey, *"Geometrical frustration in the ferromagnetic pyrochlore $Ho_2Ti_2O_7$"*, Phys. Rev. Lett. **79**, 2554 (1997).

[26] S. T. Bramwell and, M. J. P. Gingras, *"Spin ice state in frustrated magnetic pyrochlore materials"*, Science **294**, 1495 (2001).

[27] J. S. Gardner, S. R. Dunsiger, B. D. Gaulin, M. J. P. Gingras, J. E. Greedan, R. F. Kiefl, M. D. Lumsden, W. A. MacFarlane, N. P. Raju, J. E. Sonier, I. Swainson, and Z. Tun, *"Cooperative paramagnetism in the geometrically frustrated pyrochlore antiferromagnet $Tb_2Ti_2O_7$"*, Phys. Rev. Lett. **82**, 1012 (1999).

[28] J. S. Gardner, A. Keren, G. Ehlers, C. Stock, Eva Segal, J. M. Roper, B. Fak, M. B. Stone, P. R. Hammar, D. H. Reich, and B. D. Gaulin, *"Dynamic frustrated magnetism in $Tb_2Ti_2O_7$ at 50* mK*"* , Phys. Rev. B **68**, 180401 (2003).

[29] N. P. Raju, M. Dion, M. J. P. Gingras, T. E. Mason, and J. E. Greedan, *"Transition to long-range magnetic order in the highly frustrated insulating pyrochlore antiferromagnet $Gd_2Ti_2O_7$"*, Phys. Rev. B **59**, 14489 (1999).

[30] A. P. Ramirez, B. S. Shastry, A. Hayashi, J. J. Krajewski, D. A. Huse, and R. J. Cava, *"Multiple field-induced phase transitions in the geometrically frustrated dipolar magnet: $Gd_2Ti_2O_7$"*, Phys. Rev. Lett. **89**, 067202 (2002).

[31] J. A. Hodges, P. Bonville, A. Forget, A. Yaouanc, P. Dalmas de Réotier, G. Andre, M. Rams, K. Krolas, C. Ritter, P. C. M. Gubbens, C. T. Kaiser, P. J. C. King and C. Baines, *"First-order transition in the spin dynamics of geometrically frustrated $Yb_2Ti_2O_7$"*, Phys. Rev. Lett. **88**, 077204 (2002).

[32] B. C. den Hertog and M. J. P. Gingras, *"Dipolar interactions and origin of spin ice in Ising pyrochlore magnets"* , Phys. Rev. Lett. **84**, 3430 (2000).

[33] M. J. P. Gingras, B. C. den Hertog, M. Faucher, J. S. Gardner, L. J. Chang, B. D. Gaulin, N. P. Raju, and J. E. Greedan, *"Magnetic and thermodynamic properties of the collective paramagnet-spin liquid pyrochlore $Tb_2Ti_2O_7$"*, Phys. Rev. B, **62**, 6496 (2000).

[34] A. P. Ramirez, A. Hayashi, and R. J. Cava, R. Siddharthan and B. S. Shastry, *"Zero-point entropy in spin ice"*, Nature **399**, 333 (1999).

[35] S. Rosenkranz, A.P. Ramirez, A. Hayashi, R.J. Cava, R. Siddharthan, and B.S. Shastry, *"Crystal-field interaction in the pyrochlore magnet $Ho_2Ti_2O_7$"*, J. Appl. Phys. **87**, 5914 (2000).

[36] H. Fukazawa, R. G. Melko, R. Higashinaka, Y. Maeno, and M. J. P. Gingras, *"Magnetic anisotropy of the spin ice compound $Dy_2Ti_2O_7$"*, Phys. Rev. B **65**, 054410 (2002).

[37] Y. Yasui, M. Kanada, M. Ito, H. Harashina, M. Sato, H. Okumura, K. Kakurai, H. Kadowaki, *"Static correlation and dynamical properties of $Tb^{3+}$-moments in $Tb_2Ti_2O_7$ −neutron scattering study"*, J. Phys. Soc. Jpn. **71**, 599 (2002).

[38] S. T. Bramwell, M. J. Harris, B. C. den Hertog, M. J. P. Gingras, J. S. Gardner, D. F. McMorrow, A. R. Wildes, A. L. Cornelius, J. D. M. Champion, R. G. Melko, and T. Fennell, *"Spin correlations in $Ho_2Ti_2O_7$: A dipolar spin ice system"*, Phys. Rev. Lett. **87**, 047205 (2001).

[39] R. G. Melko, B. C. den Hertog, and M. J. P. Gingras, *"Long range order at low temperature in dipolar spin ice"*, Phys. Rev. Lett. **87**, 067203 (2001).

[40] B. S. Shastry, *"Spin ice and other frustrated magnets on the pyrochlore lattice"*, Physica B. **329**, 1024 (2003).

[41] R. R. Siddharthan, B. S. Shastry, A. P. Ramirez, A. Hayashi, R. J. Cava, and S. Rosenkranz, *"Ising pyrochlore magnets: low-temperature properties, ice rules, and beyond"*, Phys. Rev. Lett. **83**, 1854 (1999).

[42] A. Keren, J. S. Gardner, G. Ehlers, A. Fukaya, E. Segal, and Y. J. Uemura, *"Dynamic properties of a diluted pyrochlore cooperative paramagnet $(Tb_pY_{1-p})_2O_2Ti_2O_7$"*, Phys. Rev. Lett. **92**, 107204 (2004).

[43] J. S. Gardner, B. D. Gaulin, A. J. Berlinsky, P. Waldron, S. R. Dunsiger, N. P. Raju, and J. E. Greedan, *"Neutron scattering studies of the cooperative paramagnet pyrochlore $Tb_2Ti_2O_7$"*, Phys. Rev. B **64**, 224416 (2001).

[44] S. R. Dunsiger, R. F. Kiefl, K. H. Chow, B. D. Gaulin, M. J. P. Gingras, J. E. Greedan, A. Keren, K. Kojima, G. M. Luke, W. A. MacFarlane, N. P. Raju, J. E. Sonier, Y. J. Uemura and W. D. Wu, *"Muon spin relaxation investigation of the spin dynamics of geometrically frustrated antiferromagnets $Y_2Mo_2O_7$ and $Tb_2Mo_2O_7$"*, Phys. Rev. B **54**, 9019 (1996).

[45] N. Hamaguchi, T. Matsushita, N. Wada, Y. Yasui, and M. Sato, *"Low-temperature phases of the pyrochlore compound $Tb_2Ti_2O_7$"*, Phys. Rev. B **69**, 132413 (2004).

[46] G. Luo, S. T. Hess, and L. R. Corruccini, *" Low temperature magnetic properties of the geometrically frustrated pyrochlores $Tb_2Ti_2O_7$, $Gd_2Ti_2O_7$, and $Gd_2Sn_2O_7$"* Physics Letters A **291**, 306(2001).

[47] I. Mirebeau, I. N. Goncharenko, P. Cadavez-Peres, S. T. Bramwell, M. J. P. Gingras, and J. S. Gardner, *"Pressure-induced crystallization of a spin liquid"*, Nature **420**, 54 (2002).

[48] I. Mirebeau, I. N. Goncharenko, G. Dhalenne, and A. Revcolevschi, *" Pressure and field induced magnetic order in the spin liquid $Tb_2Ti_2O_7$ as studied by single crystal neutron diffraction"*, Phys. Rev. Lett. **93**, 187204 (2004).

[49] I. Mirebeau, A. Apetrei, J. Rodriuez-Carvajal, P. Bonville, A. Forget, D. Colson, V. Glazkov, J. P. Sanchez, O. Isnard, and E. Suard, *"Ordered spin ice state and magnetic fluctuations in $Tb_2Sn_2O_7$"*, Phys. Rev. Lett. **94**, 246402 (2005).

[50] P. Dalmas de Réotier, A. Yaouanc, L. Keller, A. Cervellino, B. Roessli, C. Baines, A. Forget, C. Vaju, P. C. M. Gubbens, A. Amato, and P. J. C. King,

*"Spin dynamics and magnetic order in magnetically frustrated $Tb_2Sn_2O_7$"*, Phys. Rev. Lett. **96**, 127202 (2006).

[51] K. C. Rule, J. P. C. Ruff, B. D. Gaulin, S. R. Dunsiger, J. S. Gardner, J. P. Clancy, M. J. Lewis, H. A. Dabkowska, I. Mirebeau, P. Manuel, Y. Qiu, and J. R. D. Copley, *"Field-induced order and spin waves in the pyrochlore antiferromagnet $Tb_2Ti_2O_7$"*, Phys. Rev. Lett. **96**, 177201 (2006).

[52] S.-W. Han, J. S. Gardner, and C. H. Booth, *"Structural properties of the geometrically frustrated pyrochlore $Tb_2Ti_2O_7$"*, Phys. Rev. B **69**, 024416 (2004).

[53] O. Ofer, A. Keren, C. Baines, J. S. Gardner, *"Lack of static lattice distortion in $Tb_2Ti_2O_7$"*, Cond-mat/0609125.

[54] M. Enjalran and, M. J. P. Gingras, *"Theory of paramagnetic scattering in highly frustrated magnets with long-range dipole-dipole interactions: The case of the $Tb_2Ti_2O_7$ pyrochlore antiferromagnet"*, Phys. Rev. B 70, 174426 (2004).

[55] Y.-J Kao, M. Enjalran, A. Del Maestro, H. R. Molavian, and M. J. P. Gingras, *"Understanding paramagnetic spin correlations in the spin-liquid pyrochlore $Tb_2Ti_2O_7$"*, Phys. Rev. B **68**, 172407 (2003).

[56] H. R. Molavian, M. J. P. Gingras, and B. Canals, *"Dynamically-induced frustration as a route to a quantum spin ice state in $Tb_2Ti_2O_7$ via virtual crystal field excitations and quantum many-body effects"*, Phys. Rev. Lett. **98**, 157204 (2007).

[57] A. Abragam and B. Bleaney, *" Electron Paramagnetic Resonance of Transition Ions"*, Clarendon Press (1970).

[58] K. W. H. Stevens, *"Matrix elements and operator equivalents connected with the magnetic properties of rare earth ions"*, Proc. Phys. Soc., London, Sect. A **65**, 209 (1952).

[59] M. T. Hutchings, *"Point-charge calculation of energy levels of magnetic ions in crystalline electric fields"*, Solid State Phys **16**, 227 (1964).

[60] K. R. Lea, M. J. M. Leask, and W. P. Wolf, *"The raising of angular momentum degeneracy of f-Electron terms by cubic crystal fields"*, J. Phys. Chem. Solids **23**, 1381 (1962).

[61] J. Jensen and A. Mackintosh, *"Rare Earth Magnetism"*, Clarendon Press (1991).

[62] A. J. Freeman and J. P. Descalaux, *"Dirac-Fock studies of some electronic properties of rare-earth ions"*, J. of Mag. and Mag. Mater. **12**, 11 (1979).

[63] A. J. Kassman, *"Relationship between the coefficients of the tensor operator and operator equivalent methods"*, J. Chem. Phys. **53**, 4118 (1970).

[64] I. Lindgren and J. Morrison, *"Atomic many-body theory"*, Springer-Verlag 2nd Edition (1986).

[65] A. G. Del Maestro and, M. J. P. Gingras, *"Quantum spin fluctuations in the dipolar Heisenberg-like rare earth pyrochlores"*, J. Phys. Condens. Matter **16**, 3339(2004).

[66] J. P. Ruff, R. G. Melko, and M. J. Gingras, *"Finite-temperature transitions in dipolar spin ice in a large magnetic field"*, Phys. Rev. Lett. **95**, 097202 (2005).

[67] R. Siddharthan, B. S. Shastry, and A. P. Ramirez *"Spin ordering and partial ordering in holmium titanate and related systems"*, Phys. Rev. B. **63**, 184412 (2001).

[68] K. Matsuhira, Y. Hinatsu, K. Tenya, and T. Sakakibara, *"Low temperature magnetic properties of frustrated pyrochlore ferromagnets $Ho_2Sn_2O_7$ and $Ho_2Ti_2O_7$"*, J. Phys.: Condens. Matter **12**, L649(2000).

[69] M. J. Harris, S. T. Bramwell, D. F. McMorrow, T. Zeiske, and K. W. Godfrey, *"Liquid-gas critical behavior in a frustrated pyrochlore ferromagnet"*, Phys. Rev. Lett. **81**, 4496 (1998).

[70] T. Sakakibara, T. Tayama, Z. Hiroi, K. Matsuhira, and S. Takagi, *"Observation of a liquid-gas-type transition in the pyrochlore spin ice compound $Dy_2Ti_2O_7$ in a magnetic field"*, Phys. Rev. Lett. **90**, 207205 (2003).